6th BSME International Conference on Thermal Engineering (ICTE 2014)

Effect of Temperature on Biogas Production from Rice Straw and Rice Husk

Mrs. Manjula Das Ghatak[a], Prof. Pinak Mahanta[b]

[a]*Research Scholar Department of Mechanical Engineering, IIT Guwahati, Guwahati, Assam, 781036 India*
[b]*Professor, Department of Mechanical Engineering, IIT Guwahati, Guwahati, Assam, 781036 India*

Abstract

The objective of this paper is to investigate the effect of temperature on anaerobic digestion of two very common lignocellulosic biomasses such as rice husk and rice straw. Rice husk and rice straw are abundant in south East Asia. They are not effectively used for any fruitful purpose rather they are disposed of in the open environment polluting the atmosphere and causing serious health problem. In this paper the rice husk and rice straw were first characterized to see their potentiality for biogas production and then pretreated to make the biogas production achievable. The anaerobic digestion was considered at three different operating temperatures, namely, 45°C, 50°C and 55°C, respectively. Effect of temperature on kinetic rate constant was also studied. It was observed from the investigation that biogas production increases with increase in temperature. The kinetic rate constant plays a significant role to indicate the digestion process.
© 2015 The Authors. Published by Elsevier Ltd.
Peer-review under responsibility of organizing committee of the 6th BSME International Conference on Thermal Engineering (ICTE 2014).

*Keywords:*Lignocellulosic biomasses; anaerobic digestion; kinetic rate constant; biogas production.

1. Introduction

With the depletion of fossil fuels cost of petrol and diesel is increasing day by day because of which development of alternate fuel source is getting emphasized now-a-days. Currently biogas production from cattle dung is getting a very good response due to its economical, eco-friendly usage and readily digestible nature. But cattle dung which is worldwide used for biogas production is not abundant in south Asian countries like India. Whereas various bio-

wastes or agricultural wastes with high cellulose content like rice husk and rice straw are obtainable in plenty in this region. These wastes are either uneconomically used or disposed of as they are, thereby causing serious pollution problems. These bio-wastes also contain lignin rendering its anaerobic digestion slow with conventional digestion methods. As a result these bio-wastes cannot be directly used for biogas production. To break the lignin content pre-treatment were done and were mixed with cattle dung to enhance the biogas production.

One of the major problems in utilizing these materials is their low-digestibility. The lignin to cellulose ratio is normally used to define the degree of digestibility of the biomasses [2]. The digestibility of lignocellulosic biomasses can be improved by pretreatments [3, 1]. Pretreatments involve the alteration of cellulose structure of the biomass rendering fast hydrolysis of both the cellulose and hemicellulose producing biogas in short span of time. Various pretreatments methods that can be applied include mechanical/physical, chemical and biological pretreatments. The most significant physical pretreatment include the particle size reduction [1], which eventually leads to the increase in available surface area and the release of intracellular components [3,4].

The effectiveness of anaerobic digestion naturally depends upon the intensity of bacterial activity which is affected by various factors [5]. Among the many factors, temperature is one important factor which affects the anaerobic digestion. The anaerobic digestion under thermophilic condition provides the various advantages such as high metabolic rates, high specific growth rate of bacteria, at the same time high death rates of bacteria also as compared to mesophilic condition [6]. Mackie and Bryant, 1995 [7] found that thermophilic (60°C) anaerobic digestion of cattle waste is more stable as compared to mesophilic (40°C). Thermophilic digestion is 4 (Four) times more intense and can yield more biogas. Thermophilic stabilization of energy plants at 55°C is truly economical as it produces more biogas [8].

The objective of the present study is to investigate the effect of temperature on biogas production rate of rice husk and rice straw each mixed with cattle dung.

Nomenclature

k	kinetic rate constant
C_B	substrate concentration or concentration of biodegradable volatile solids (VS)
t	time
C_t	substrate concentration at time t
C_0	Initial substrate concentration
y_m	volume of biogas produced per unit mass of volatile solids converted at maximum time (ml/gm)
y_t	volume of biogas produced per unit mass of volatile solids fed at any time, t (ml/gm)

---

2. Materials and methods

The biomasses rice husk and rice straw were collected locally, cleaned and dried under sun. Then they were dried in the hot air oven for 24 hours and separately ball milled to reduce the particle size.

Total solid and volatile matter were determined following standard test methods ASTM E1756-08, and E872-82 (Reapproved 2006) respectively. Carbon and Nitrogen content of the biomasses was determined by using Energy Dispersive X-ray Spectroscopy (EDX) analytical technique.

Table 1. Characterization of Rice Husk and Rice Straw [9]

	Rice Husk	Rice Straw	Cattle Dung
Total Solid (%)	89.41	87.33	19.02
Volatile Solids (%)	74.07	65.15	66.2
Carbon (%)	32.79	32.19	35
Nitrogen (%)	0.40	0.98	1.6
C:N ratio	81.97	32.84	21.8
Hemicellulose (%)	24	35	2.3
Cellulose (%)	28	30.2	4.7

Lignin (%)	25	22	2.7
Lignin/cellulose ratio	0.892	0.728	0.574

Table 1 presents the results of the characterization of rice husk, rice straw and cattle dung on dry weight basis. Total solid (TS) of rice husk and rice straw were 89.41 and 87.33% respectively and that of cattle dung was 19.02%. The C:N ratio of rice husk and rice straw was 81.97 and 32.84 whereas that of cattle dung was 21.8:1. Hills and Roberts, 1981 [10] reported that the performance of digesters containing dairy manure and field crop residues is the maximum when the C:N ratio of the feed mixtures was between 25 to 30:1 and total solid of the slurry was 8%. Budiyono et al., 2010 [11] stated that TSs content of 7.4 and 9.2% in cattle dung exhibit the best performance for digestibility. Mahanta et al., 2004 [12] reported that for cattle dung at 35℃ temperature maximum gas production was obtained with 8% total solid. That is why to get the maximum biogas production from rice husk and rice straw, they were first mixed with fresh cattle dung in 1: 3 ratio, so that their overall C:N ratio comes in between 25 to 30:1. After that water was mixed with the mixtures in 1:3 ratios to bring down the total solid to 9%.

3. Experimental set-up and procedure

The schematic diagram of the experimental set-up is shown in Fig. 2. It consists of a laboratory bio-digester made of borosilicate glass of capacity 1000 ml with air tight rubber cork fitted into its opening. Thermometer and copper tube were fitted through the rubber cork for measuring the slurry temperature and fitting the connecting tube. The other end of the connecting tube was passed through a 500 ml solution bottle containing brine solution. Thus, the biogas produced in the biodigester by the anaerobic digestion process was delivered through the connecting tube to the solution bottle containing brine. The pressure of the biogas produced caused displacement of the brine solution which is then collected in a 200 ml beaker placed on the other side of the solution bottle. The amount of solution collected in the beaker represented the amount of biogas produced in the biodigester. A sampling port was provided through the cork fitted with a valve to take out sample from time to time testing of sample for total solid, volatile solid and pH.

A weighing balance was used to measure the required mass of cattle dung and biomasses. The mercury-in-glass thermometer (range -10℃ to 110℃) fitted to the bio-digester through the cork was used to measure the daily temperature of the slurry and a digital pH meter was used to determine the pH of the fermentation slurry. The constant temperatures of the digesters were maintained by putting the digesters in the water bath at fixed temperature. Two sets of digesters, each having three samples were prepared. In one set substrate was rice straw and cattle dung mixture and in the other set substrate was rice husk and cattle dung mixtures. Both rice straw and rice husk were mixed with fresh cattle dung in 1:3 ratio and water was added to the mixtures in 1:3 ratio. The filled in digesters were kept in water bath at 45℃, 50℃ and 55℃ temperatures respectively to study the effect of temperature on gas production from rice straw and cattle dung mixture and rice husk and cattle dung mixtures for 50 days HRT. The temperature of the feedstock was measured twice a day with the help of the thermometer fitted through the cork and pH was monitored on weekly basis. Gas production was measured by water displacement method.
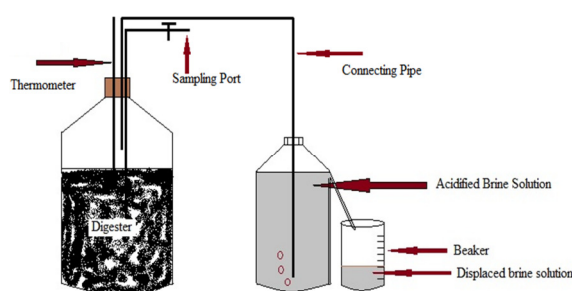

Fig. 1. Schematic diagram of experimental set-up [9]

Table 2. Properties of biomass cattle dung mixtures.

Substrates	Total Solid (%)	C:N ratio
Rice straw and cattle dung mixture	8.9	24.06
Rice husk and cattle dung mixture	9.1	26.49

Table 2 shows the influent TS (%) and C:N ratios of rice straw and cattle dung mixture and rice husk and cattle dung mixture. It is seen that influent total solid and C:N ratio of rice straw and cattle dung mixture were found to be 8.9% and 24.06 respectively; and for rice husk and cattle dung mixture they were 9.1% and 26.49 respectively which is a favourable condition for good biogas production.

The biogas production was monitored daily and measured every five days. The biogas production was observed and recorded for 50 days until biogas production reduced significantly and it was found that the biogas production was very slow at the beginning and at the end of observation. This is because the biogas production in batch condition directly corresponds to specific growth rate of methanogenic bacteria in biodigester [11, 13].

4. Kinetic model

The kinetics of digestion process is crucial in determining the rate of gas production per unit mass of volatile solid. Using chemical engineering theory, a description of batch digestion kinetics is obtained [14, 1]. For first order kinetics, the rate of degradation of the volatile solids is given by-

$$\frac{dC_B}{dt} = -kC_B \tag{1}$$

where, C_B is the substrate concentration or concentration of biodegradable volatile solids (VS), k is the first order kinetic rate constant and t is the time. Rearranging Eq. (1)

$$\frac{dC_B}{C_B} = -kdt \tag{2}$$

Integrating both sides we get,

$$\int_{C_0}^{C_t} \frac{dC_B}{C_B} = -\int_0^t kdt \tag{3}$$

$$or, \ln\left(\frac{C_t}{C_0}\right) = -kt \tag{4}$$

$$or, \frac{C_t}{C_0} = \exp(-kt) \tag{5}$$

According to B. Linke, 2006 [15], the transformation of biodegradable solids (C) into biogas (y) at time t can be correlated as shown in Fig. 2. The biodegradable fraction of the complex organic substrate is converted to biogas according to Eq. (6).
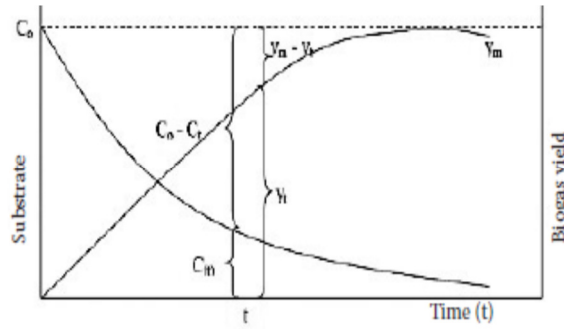
$$\frac{y_m}{y_m - y_t} = \frac{C_0}{C_t} \tag{6}$$

Fig. 2. Correlation between substrate degradation and biogas production in course of time [15]

$$o\,r,\; \frac{y_m - y_t}{y_m} = \frac{C_t}{C_0} \tag{7}$$

Now, replacing $\dfrac{C_t}{C_0}$ in Eq.(5) with $\dfrac{y_m - y_t}{y_m}$, we have

$$\frac{y_m - y_t}{y_m} = \exp(-kt) \tag{8}$$

$$o\,r,\; y_t = y_m\{1 - \exp(-kt)\} \tag{9}$$

where, y_t= volume of biogas produced per unit mass of volatile solids fed at any time, t (ml/gm); y_m=volume of biogas produced per unit mass of volatile solids converted at maximum time (ml/gm); k= kinetic rate constant (day^{-1}) and t= time of digestion (days).

Evaluation of substrate biodegradability and kinetic rate constant was done by applying Eq (12). For that the Eq. (9) was linearized [15].

Differentiating Eq. (9),

$$\frac{dy_t}{dt} = y_m k \exp(-kt) \tag{10}$$

Taking natural logarithm on both sides of the equation,

$$\ln\left(\frac{dy_t}{dt}\right) = (\ln y_m + \ln k) - kt \tag{11}$$

This equation was further reduced to the following form,

$$\frac{1}{t}\ln\left(\frac{dy_t}{dt}\right) = \frac{1}{t}(\ln y_m + \ln k) - k \tag{12}$$

Which is analogous to a straight line equation, $y=mx+c$, where, $(\ln y_m + \ln k)$ represents the slope and $(-k)$ represents the intercept of the graph of $\frac{1}{t}\ln\left(\frac{dy_t}{dt}\right)$ vs inverse of the hydraulic retention time. Thus the first order kinetic rate constant can be easily determined from the plot of $\frac{1}{t}\ln\left(\frac{dy_t}{dt}\right)$ vs inverse of the hydraulic retention time.

The term $(-k)$ is a measure of the rate of removal of the biodegradable fractions as the biogas production increases with time. According to Eastman and Ferguson, 1981 [17], the first order kinetic constant k is a pure

empirical function which represents the cumulative effects of many parameters such as pH, temperature, quantity and quality of substrate, rate of removal of biodegradable fractions, rate of inhibition by other components of the substrate e.g. lignin or by-product of the reaction process such as fatty acids etc. The more negative the value of k, the faster the rates of removal of the biodegradable fractions while more the positive value of k, the slower the rate of removal of the biodegradable fractions [16]. Thus Eq.(12) can be used to detect anaerobic digestion whether it is progressive or regressive.

5. Results and discussions

5.1. Effect of temperature on cumulative biogas production

The gas production rate for the biomass mixtures, rice straw and cattle dung mixture and rice husk and cattle dung mixture at 45°C, 50°C and 55°C temperatures were recorded on daily basis for a period of 50 days. Khandelwal and Mahdi, 1986 [18] have reported that for the northeast India, 55 days retention time is recommended.
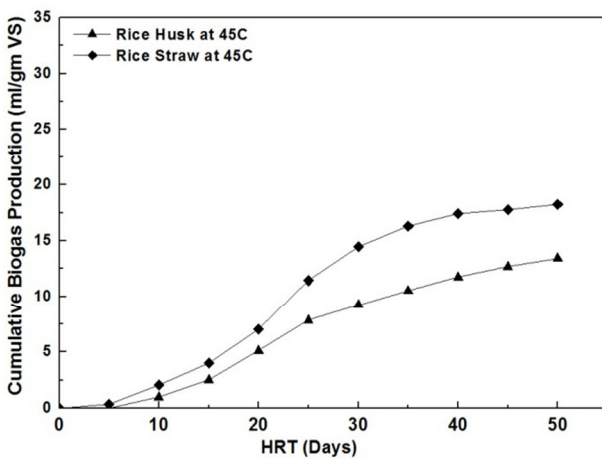

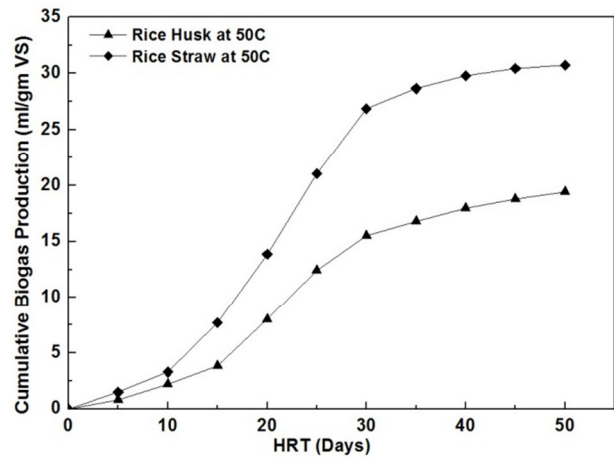Fig. 3. Cumulative biogas production at 45°C

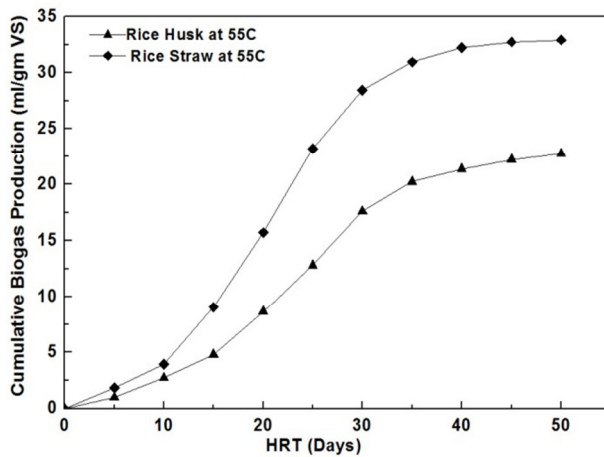Fig. 4. Cumulative biogas production at 50°C

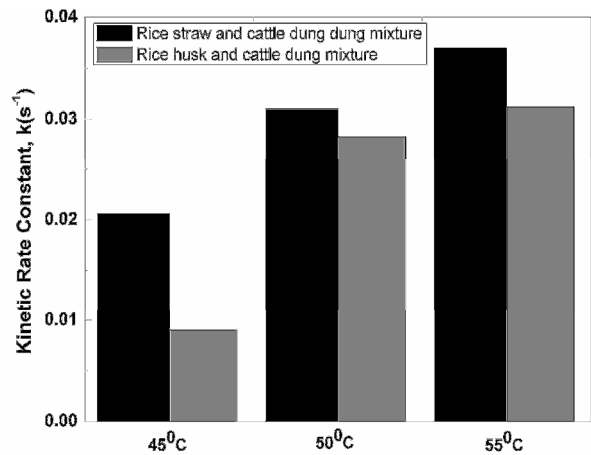Fig. 5. Cumulative biogas production at 55°C

Fig. 6. Kinetic rate constants at different temperatures

Comparison of gas production rate of rice straw and cattle dung mixture and rice husk and cattle dung mixture at three different temperatures is shown in Table 3. It is clear from the table and the graph that although biogas production from both the biomass mixtures were increasing with increase in temperature of the digestate but the biogas production from rice husk and cattle dung mixture was consistently lower than that of the rice straw and cattle dung mixture at all the temperatures.

Table 3. Comparison of cumulative biogas production.

Sample	Gas production in ml/gm VS (50 days)		
	45℃	50℃	55℃
Rice straw and cattle dung mixture	18.24	30.73	32.93
Rice husk and cattle dung mixture	13.41	19.41	22.74

Figure 3-5 show the comparison of cumulative biogas production rate of rice straw and rice husk each mixed with cattle dung at 45℃, 50℃ and 55℃ respectively. It is seen that the biomasses mixed with the cattle dung has the highest biogas production rate at 55℃, followed by 50℃ and 45℃. In case of both the biomasses as temperature increases biogas production rate increases. But biogas production rate from rice husk is quite low as compared to that of rice straw mixed with cattle dung. The reason may be due to the high lignin content (25%) as well as silicon content of rice husk. Lignin content of rice straw (22%) is also high but here as rice straw is mixed with cattle dung; it is getting utilized as support medium for the biogas producing microorganisms. Support media is nothing but a biofilm carrier which provide surface on which microbial biofilms can attach and grow, increasing digester stability, and reducing the amount of microorganisms that are washed out of the digester. Andersson and Björnsson, 2002 [19] studied the behaviour of straw as support media for bacteria and found that it increased methane production more than glass or plastic carriers. On the other hand as temperature increases biogas production rate from both the biomasses increases. Also at thermophilic digestion, biogas production starts earlier as compared to 45°C. So, comparing all the three figures it can be concluded that with increase in temperature biogas production rate can be made faster and better. The large amount of biogas production at 55°C in thermophilic condition is due to the large microbial activity in thermophilic temperature range [20].

5.2. Effect of temperature on kinetic rate constant

Here 56.25 gm of rice straw, 168.75 gm of cattle dung and 675 ml of water were mixed thoroughly and fed to the 1000 ml capacity borosilicate digester. In the same proportion three samples were prepared for three different temperatures. At five day interval, biogas production was measured with the help of water displacement method as discussed in the section 3 (Experiential Set-Up and Procedure). After plotting the data of biogas production rate in the form of $\frac{1}{t}\ln\left(\frac{dy_t}{dt}\right)$ against inverse of the hydraulic retention time and fitting the curve, kinetic rate constant, k at three different temperatures was obtained.

Similarly 56.25 gm of rice husk, 168.75 gm of cattle dung and 675 ml of water were mixed thoroughly and fed to a separate 1000 ml capacity borosilicate digester. In the similar proportion three samples for three different temperatures were prepared and biogas production was measured in the same manner as is done for rice straw mixture. After plotting the data of biogas production rate in the form of $\frac{1}{t}\ln\left(\frac{dy_t}{dt}\right)$ against inverse of the hydraulic retention time and fitting the curve, kinetic rate constant, k for rice husk mixture at three different temperatures was obtained.

Table 4 shows the values of kinetic rate constant, *k* at temperatures 45°C, 50°C and 55°C respectively. Figure 6 shows the graphical representation of the variation of kinetic rate constant, *k* with temperature.

Table 4. Substrate concentration and kinetic rate constants at different temperatures

Substrates	Influent TS, gm	Influent VS, gm	Kinetic rate constant, k		
			45℃	50℃	55℃
Rice straw and cattle dung mixture	84.56	55.46	0.0206	0.031	0.037
Rice husk and cattle dung mixture	84.93	60.71	0.0091	0.0283	0.0312

Comparing different values of *k* at different temperatures for 50 days HRT, it can be concluded that temperature plays a very important role in controlling the kinetic rate constant. For both rice straw and rice husk each mixed with cattle dung value of *k* is the highest at 55℃, followed by 50℃ and 45℃. It is observed that the kinetic rate constant of rice straw is higher than that of the rice husk mixed with cattle dung irrespective of temperature effect. This is due to the presence of lignin as well as silica in rice husk. On the other hand higher kinetic rate constant in case of rice straw is due to its behaviour as support media for microorganisms. So, for the same percentage of total solid and same amount of cattle dung mixed with the biomasses, reaction rate of rice straw and cattle dung mixture is faster which eventually lead to the better biogas production.

6. Conclusions

From the present investigation it is concluded that biogas production rate can be improved by increasing the temperature of the slurry as thermal pre-treatment is one of the important factor to improve the anaerobic digestion of lignocellulosic biomasses [21]. Kinetic rate constant at 55°C is the highest, followed by 35°C and 45°C for both the biomasses. In thermophilic condition biogas yield at 55°C is far better and faster, so if we can provide extra energy for increasing the temperature of feedstock, 55°C temperature is a very good option for best biogas production. Only disadvantage of thermophilic anaerobic digestion is that more energy is needed for heating the digesters.

References

[1] J. Van der Geer, J.A.J. Hanraads, R.A. Lupton, The art of writing a scientific article, J. Sci. Commun. 163 (2000) 51–59.
[2] W. Strunk Jr., E.B. White, The Elements of Style, third ed., Macmillan, New York, 1979.
[3] G.R. Mettam, L.B. Adams, How to prepare an electronic version of your article, in: B.S. Jones, R.Z. Smith (Eds.), Introduction to the Electronic Age, E-Publishing Inc., New York, 1999, pp. 281–304.
[1] L.T. Fan, M.M. Gharpuray, Y.H. Lee, Evaluation of pretreatments for enzymatic conversion of agricultural residues, Biotechnol. Bioeng. Symp. 11, (1988) 29-45.
[2] S.K. Sharma, I.M. Mishra, M.P. Sharma, J.S. Saini, Effect of particle size on biogas generation from biomass residues, Biomass. 17, (1988) 251-263.
[3] L. Palmowski, J.Müller, Influence of the size reduction of organic waste on their anaerobic digestion, Proc. 2nd International Symposium on Anaerobic Digestion of SolidWaste, IWA Publishing, London, 1999, pp.137–144.
[4] A.Lehtomaki, S. Huttunen, J.A. Rintala, Laboratory Investigations on co-digestion of Energy Crops and Crop Residues with Cow manure for Methane Production: Effect of Crop to Manure Ratio, Resources, Conservation and Recycling. 51, (2006) 591-609.
[5] K.M. Mittal, Biogas Systems: principles and applications, New age international (P) limited, New Delhi, India, 1996.
[6] J.B. Van Lier, Thermophilic anaerobic wastewater treatment; Temperature aspects and process stability, Ph.D. Thesis, Wageningen Agricultural University, Wageningen, The Netherlands, 1995.
[7] R.I. Mackie and M.P. Bryant, Anaerobic digestion of cattle waste at mesophilic and thermophilic temperatures, Appl. Microbiol. Biotechnol. 43, (1995) 346–350.
[8] P. Vindis, B. Mursec, M. Janzekovic, F. Cus, The impact of mesophilic and thermophilic anaerobic digestion on biogas production, Journal of Achievements in Materials and Manufacturing Engineering. 36, (2009) 192-198.
[9] M. Das Ghatak and P. Mahanta (2014), "Kinetic assessment of biogas production from lignocellulosic biomasses". International Journal of Engineering and Advanced Technology (IJEAT), vol. 3(5), pp. 244-249.
[10] D.J. Hills, D. W. Roberts, Anaerobic digestion of dairy manure and field crop residues, Agricultural Wastes. 3, (1981) 179-189.
[11] I.N. Budiyono, S. Widiasa, Johari and Sunarso, The kinetic of biogas production rate from cattle manure in batch mode, International Journal of chemical and biological Engineering. 3, (2010) 39-44.

[12] P. Mahanta, U.K.Saha, A. Dewan, P. Kalita, The influence of temperature and total solid concentration on the gas production rate of a biogas digester, Journal of Energy in Southern Africa. 15, (2004) 112-117.

[13] A. Nopharatana, P. C. Pullammanappallil, W. P. Clarke, Kinetics and dynamic modeling of batch anaerobic digestion of municipal solid waste in a stirred reactor, Waste Management. 27, (2007) 595–603.

[14] D.L. Wise, Feasibility of anaerobic digestion of agricultural crop residues for production of methane, Vol.2 Boca Raton, Florida: CRC press; 1981.

[15] B. Linke, Kinetic study of thermophilic anaerobic digestion of solid wastes from potato processing, J. Biomass and Bioenergy. 30 (10), (2006) 892-896.

[16] M.O.L.Yusuf , A. Debora, D.E.Ogheneruona, Ambient temperature kinetic assessment of biogas production from co-digestion of horse and cow-dung, Res. Agr. Eng., 57 (3), (2011) 97-104.

[17] J.A. Eastman, J.F. Ferguson, Solubilization of particulate organics carbon during the acid phase of anaerobic digestion, Journal of Water Pollution Control Federation. 53, (1981) 352.

[18] K.C. Khandelwal, S.S. Mahdi, Biogas Technology, vol.1, Tata Mcgraw-Hill, New Delhi, 1986.

[19] J. Andersson, and L. Björnsson, Evaluation of straw as a biofilm carrier in the methanogenic stage of two-stage anaerobic digestion of crop residues, Bioresource technology. 85(1), (2002) 51-56.

[20] P. Mahanta, A. Dewan, U.K. Saha, P. Kalita, Effect of temperature and agitation on the performance of biogas digester, Proceedings of 2nd BSME-ASME International conference on Thermal Engineering Dhaka, 2, (2004) 873-879.

[21] I. Ferrer, S. Ponsa, F. Vazquez, X. Font, Increasing biogas production by thermal (70°C) sludge pre-treatment prior to thermophilic anaerobic digestion, Biochemical engineering journal. 42, (2008) 186-192.

6th BSME International Conference on Thermal Engineering (ICTE 2014)

Performance of a Diesel Engine run with Mustard-Kerosene blends

S. M. Ameer Uddin[a*], A. K. Azad[b], M. M. Alam[c] and J. U Ahamed[d]

[a,c] *Department of Mechanical Engineering*
Bangladesh University of Engineering & Technology, BUET, Dhaka-1000, Bangladesh
[b]*School of engineering and Technology, Central Queensland University,Rockhampton, QLD-4701, Australia*
[d]*Department of Mechanical Engineering,CUET,Chittagong,Bangladesh*
E-mail: ameer.cuet01@gmail.com[a], sumonbd.ameer@gmail.com[a]*, a.k.azad@cqu.edu.au[b]*

Abstract

Increasing oil prices and global warming activates the research and development of substitute energy resources to maintain economic development. The methyl esters of vegetable oil, known as biodiesel are becoming popular because of their low ecological effect and potential as a green substitute for compression ignition engine. Diesel engines are more efficient and cost-effective than other engines. Vegetable oils can be used in the diesel engine by pure form or by trans-esterified form. In this paper pure mustard oil blending with kerosene at different proportion like m20, m30, m40, m50 and M100 (pure mustard) has been used in different load condition in 4 stroke single cylinder diesel engine mounted on a hydraulic dynamometer bed. Physical properties of different blend like heating value, density, viscosity, flash point and fire point has been determined before engine testing. The engine data was taken applying load from 6 kg to 15 kg at constant rpm 2000.From this study we find that among , the blends m20 and m30 has the minimum bsfc 257.94 gm/kw-hr at 12.5 kg load & 269.67gm/kw-hr at 12.5 kg load condition respectively. Hence m20 can beconsidered as suitable blend for mustard blending with kerosene for diesel engine .

© 2015 The Authors. Published by Elsevier Ltd.
Peer-review under responsibility of organizing committee of the 6th BSME International Conference on Thermal Engineering (ICTE 2014).

Keywords: Bio-diesel, Blend of bio-diesel, Mustard, bsfc, bhp.

1. Introduction

Due to gradual depletion of world petroleum reserves and the impact of environmental pollution there is an urgent need for suitable alternative fuels for use in diesel engines. In view of this, vegetable oil is a promising alternative because it is renewable, environment friendly and produced easily in rural areas, where there is an acute need for modern form of energy [1-2].

In recent year's systematic effort have been made by several research workers to use as fuel engines. It is said that energy consumption pattern is an indicator of the socio-economic development of a country. It is also a measure of the quality of life. Energy consumption is growing day by day along with technological development of a country [3-4]. Although the industrialized and developed world consumes most of the energy resources, the demand of energy in the developing world has also increased in recent decades due to their economic take off and sustainability [5-6]. Internal combustion (IC) engines are widely employed in many development activities using a greater portion worlds energy resources .From the very beginning, the IC engines are being fuelled mostly by petroleum products like petrol and diesel. IC engines use only a small fraction of distillation products of crude oils [7-8]. These crude oils have limited reserves. Any shortfall of petroleum fuels in the world market will therefore have a great impact on the economy of non-oil third world countries. Vegetable oils from crops such as Soyabean, Peanut, Sunflower, Rape, Coconut, Karanja, Neem, Mustard Jatropha, linseed and Coster have been evaluated in many parts of the world in comparison with other non-edible oils [9-10]. Different countries are looking for different vegetable oils depending on their climate and soil condition. As for example Soyabean oil in USA, rapeseed oil and sunflower in Europe, Olive oil in Spain, palm oil in south east Asia, mainly in Malaysia and Indonesia, coconut oil in Philippines are considered to substitute diesel fuel [11]. Different researchers results show that vegetables oils are promising alternative fuels for CI engine. In view of growing energy demand of our country it is thus reasonable to examine the use of Mustard Oil as a substitute fuel for IC engine [12].

2.1. Problems of using straight vegetable oil in diesel engine

Most natural fats contain a complex mixture of individual triglycerides; because of this, they melt over a broad range of temperatures. Most vegetable oils have a range of boiling and melting temperature rather than a specified one. Straight vegetable oil (SVO) has comparatively higher density & viscosity than fossil fuels. Higher viscosity and higher density limit the use of vegetable oils directly into diesel engine cylinder. Problems associated using straight vegetable oil (SVO) in diesel engine can be classified in two groups, namely: operational and durability problems. Operation problems are related to starting ability, ignition, combustion and performance. Durability problems are related to deposit formation, carbonization of injection tip, ring sticking and lubrication oil dilution [13].

2.2. Overcome of the problems

First point blending, cracking/pyrolysis, emulsification or trans-esterification of vegetable oil may overcome these problems. Heating and blending of vegetable oil with fossil diesel also reduces viscosity and improve volatility of vegetable oil but its molecular structure remains unchanged; hence poly-unsaturated character remains. Blending of vegetable oil with diesel at diffrent proportion like 20%, 30% etc. however reduces the viscosity drastically and the fuel handling system of engine can handle the vegetable oil diesel blends without any problems. Preheating is required to such a temperature to attain the viscosity comparable to diesel fuel and then the oil can be introduced into the engine following direct or indirect injection system. It has been experienced that vegetable oil has the advantage of miscibility with diesel or kerosene and the blended fuels do not change the quality of solution for a long time at any mixed ratio. Thus a solution can be prepared by blending vegetables oils with either diesel or kerosene to reduce the viscosity thereby making the oils suitable for engine operation. This blend can be introduced into the engine where a partial substitution is possible. Vegetable oil when mixed with methanol or ethanol in presence of a catalyst (Usually sodium or potassium hydroxide) at about 50^0C, glycerol is replaced and an ester is formed –where fatty acids do not create problems in respect of instauration. This method of fuel modification improves fuel properties to meet the requirement of diesel engine, especially the low viscosity and high cetane number requirements. Another method of using a single vegetable oil is to make emulsion with a certain percentage of water immediately before injection but this technique requires some engine modifications for making emulsions. Using a single vegetable oil in diesel engine a long ignition delay is experienced having its high Self Ignition Temperature (SIT). Addition of enhancer with the oil before introducing into engine reduces the ignition delay and gives better engine performance [14].

3. Physical properties of mustard and its blends

In this experiment pure mustard oil is blended with the kerosene at 20%, 30%, 40% and 50% by volumetrically.These blends are named as m20, m30, m40, m50 and M100 (pure musatrd). The physical properties

of these blends i.e density ,viscosity,heating value,flash point and fire point were determined in the fuel testing laboratory. Density of fuel at different temperatures were measured by a standard 25 ml marked flask. Viscosities of fuels were measured as per ASTM standard D88-56 [15] using saybolt viscometer and accessories. Heating values of fuels used in this research were measured experimentally following ASTM standard D240-87 [16] using an oxygen bomb calorimeter. Flash point and fire point of test fuels were measured as per ASTM standard D93-85 [17] using Pensky-Martens closed tester.

Table 1. Physical properties at room temperature (22 °C)

Blends	Calorofic value (MJ/Kg)	Density (kg/m^3)	Viscosity (mm^2/sec)	Flash point (°C)	Fire Point (°C)
m20	42.8	837.00	2.68	45	55
m30	40.5	855.00	4.45	50	60
m40	38	863.00	6.86	55	70
m50	35.96	871.84	9.16	65	80
M100	32.43	934.00	63.4	310	350
D100	44.80	836.96	3.96	72	90

4. Engine performance study

The blends m20, m30, m40, m50 and M100 are tested in a single Cylinder 4 stroke diesel engine at various load.The loads were applied through a water brake dynamoter from 6 kg to 15 kg. The brake power (BP), brake specefic fuel consumption (BSFC), brake thermal efficiency (BTE) and brake mean effective presure (BMEP) were calculated against the applied loads. All data were derated as per **BS5514** standards. The specification of the engine & dynamometer are given in table 2.

Table 2. Specification of the engine & dynamometer

Engine		Dynamometer	
Model	S 195 G	Model	TFJ-250L
Method of starting	Hand starting	Max. braking horsepower (PS)	250
type	Single Cylinder, Horizontal, Four- stroke,	Revolutions at max. braking horsepower point (rpm)	2500-5500
Cylinder dia	95 mm	Max. braking torque (kg.m)	71.6
Piston stroke	115 mm	Max. revolutions (rpm)	5500
Nominal speed	2000 rpm	Max^m braking water quantity (Lit/min.)	75
Rated power	9.00 KW	GD (Kg. m^2)	0.25
Cooling system	Water Cooling Evaporative	Main bearings	Ball and roller bearings drip-feed lubricated
Fuel Injection Pressure (MPa)	12.75+/-0.5 kgf/cm²	Weight(Kg)	575 kg

5. Engine Performance analysis

Fig: 1 shows the variation of BSFC with   BP for different bio-fuel blends with kerosene. The curve shows that bsfc is higher at low load and decreases with the increase of load upto 12 kg after that bsfc increased again. From graph it is evident that the bsfc of pure mustard M100 is the highest and the minimum bsfc for diesel fuel D100. This is mainly due to the relationship among volumetric fuel injection system, specific gravity, viscosity, and heating value of the fuel. As a result, more biodiesel blend is needed to produce the same amount of energy due to its higher density and lower heating value in comparison to conventional diesel fuel. Again as biodiesel blends have different viscosity, so biodiesel causes poor atomization and mixture formation and thus increases the fuel consumption rate to maintain the power.The curve for pure mustard is always higher than the other blends in all load condition.Besides, The curve for the diesel fuel is lower than all blends.The minimum bsfc is obtained for D100 (232.57 gm/kw-hr) at 12 kg load . The second minimum bsfc obtained for m20 is 257.94 gm/kw-hr at 12.5 kg load. The minimum bsfc obtained for blends m30, m40, m50 and M100 are 269.67gm/kw-hr, 292.49 gm/kw-hr, 370.53 gm/kw-hr, and 525.69 gm/kw-hr respectively. The bsfc is a measure of overall efficiency of the engine. It is also inversely proportional to the thermal efficiency. So the lower value of bsfc indicates the higher of overall efficiency of the engine. The second minimum bsfc obtained for m20 is 257.94 gm/kw-hr at 12.5 kg load. The bsfc is a measure of overall efficiency of the engine. It is also inversely proportional to the thermal efficiency. So the lower value of bsfc indicates the higher of overall efficiency of the engine.
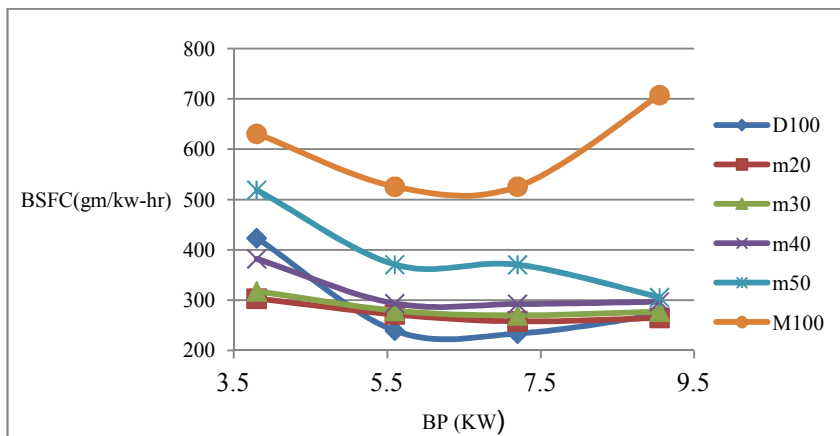

Fig: 1. Variation of BSFC with BP for kerosene blend

Fig:2 shows the relation in between BP and BTE for different blends of mustard with kerosene. The brake thermal efficiency of the pure mustard oil (M100) is lower than all other blends in all load condition. The maximum brake thermal efficiency efficiency found for the blends D100,m20,m30,m40,m50 and M100 are 35.03%, 32.61%, 32.96%, 32.38%, 32.76% and 21.11% respectively.The lowest brake thermal efficiency is 21.11 % at 12 kg load for pure mustard oil and the highest brake thermal efficiency for D100 i.e pure diesel fuel at 35.03% at 12 kg load.
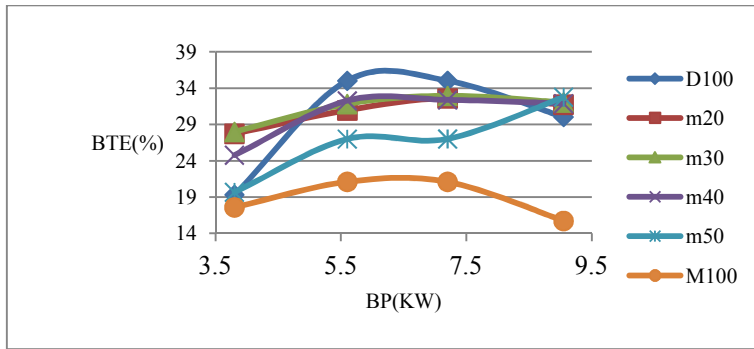
Fig: 2 .Variation of break thermal efficiency with BP

Fig: 3. depicts about variation in exhaust gas temperature with BP for different blends of kerosene. The exhaust gas temperature increases with the increase of load .Pure diesel shows the lowest exhaust gas temperature in lower load condition and shows the highest exhaus gas temperature at the higher load condition. But at middle load condition i.e. 9 to 12 kg M100 shows the highest exhaust gas temperature. Except pure mustard oil all other blends shows the similar characteristics. At starting condition, higher exhaust gas temperature but low power output for biodiesel blends indicate late burning to the high proportion of biodiesel. This would increase the heat loss, making the combustion a less efficient.
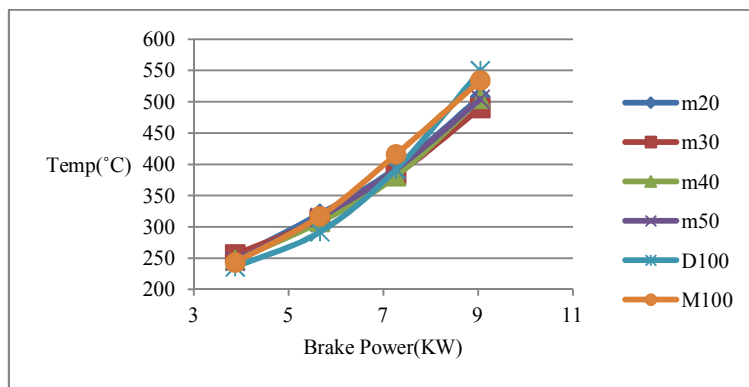

Fig: 3. Variation of exhaust gas temperature with BP

Fig:4 shows the relation in between lube oil temperature and BP for different bio-fuel blends. The lube oil temperature increases with the increase of engine load, and higher lube oil temperature found for pure diesel at all load condition than any other blends. But for pure mustard oil, lube oil temperature becomes the lowest at all load condition because of its more lubricity property.Besides, m50,m40,m30 and m20 shows gradually higher lub oil temperature than M100.

Fig: 5. shows the variation of bmep for different bio-fuel blends with BP.The mean effective pressure is the average pressure developed on the piston head over a cycle in the combustion chamber of the engine which measures the capacity of the engine to do work. A little variation of mean effective pressure has been observed during the experiment for each blend. The bmep gradually increases with the increase of engine load and the highest bmep was obtained at 15 kg load for each blends. The regular shape of the curve indicates that the proper combustion has done in the combustion chamber of the fuel.
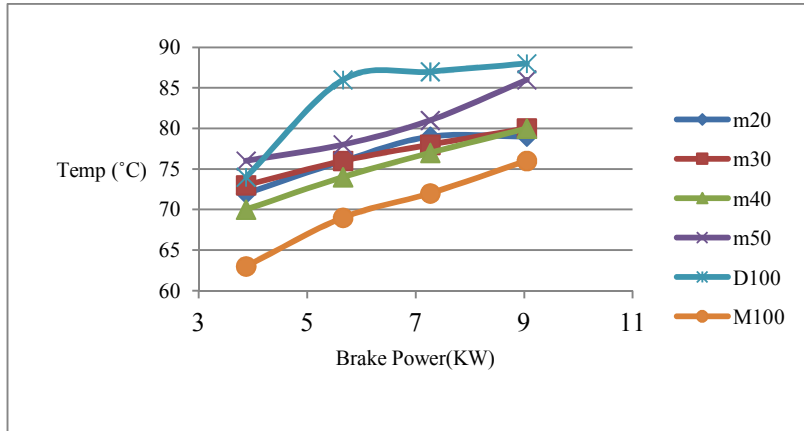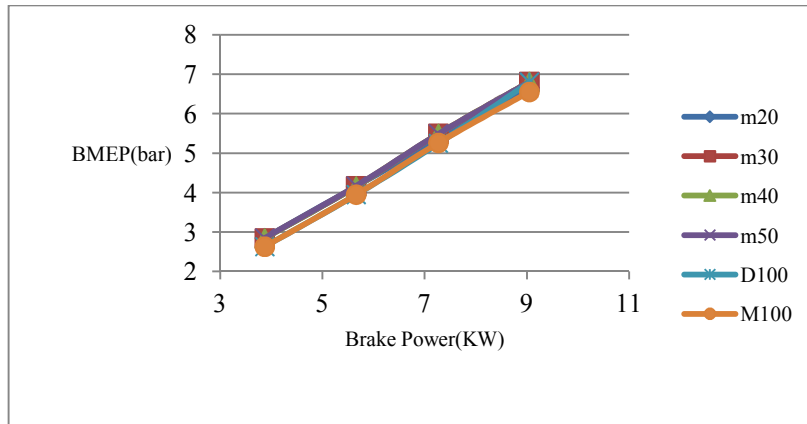
Fig: 4. Variation of lub oil temperature with BP

Fig: 5.Variation of brake mean effective pressure with BP

6. Discussion:

Fuel consumption for pure mustard (M100) is higher and lower the brake thermal efficiency than all other blends in all load condition (bsfc 525.69 gm/kw-hr & bte 21%).This is because lower calorific value of pure musatrd oil than the diesel fuel as needs more fuel to generate same power of diesel. The bsfc increase with the increase of musatard oil percentage with the kerosene.The bsfc also increase with increase of load. For different blends with different heating values, the bsfc values are misleading and hence brake thermal efficiency is employed when the engines are fueled with different types of fuels.The maximum brake thermal efficiency obtained for m30 (32.96%). The bsfc and brake thermal efficiency of blends m20, m40 & m50 (32.61%, 32.38%, 32.76%) are also close to m30 this is because higher calorific value of kerosene.Higher exhaust gas temperature but low power output for pure mustard oil and biofuel blends due to late burning of fuels.Pure mustard oil and biofuel blends shows lower lub-oil temperature due to lubricity property of mustard oil.

7. Conclusion:
- Heating value of the mustard oil (32 MJ/Kg) is much lower than the diesel and kerosene blend (Heating value of diesel and kerosene is 44 MJ/Kg and 46 MJ/Kg). So when mustard oil is used in a diesel engine

reduce the power output of the engine. The calorific value of blend m20 and m30 are very close diesel fuel.

- High viscosity is identified as a main problem of using the considered mustard oil directly in diesel engine. However, when this oil is volumetrically blended with kerosene; gives viscosity values very close to diesel fuel that required by the diesel engine. Therefore, 20% to 30% mustard oil can be blended with kerosene as substitute fuel of diesel.

- While Mustard is blended with kerosene found that the bsfc of m20 and m30 are 257.94 gm/kw-hr at 12.5 kg load & 269.67 gm/kw-hr at the same load condition which are close to standard consumption of diesel fuel (233.51 gm/kw-hr) in this engine. Hence, m20 and m30 can be considered as suitable fuel for the diesel engine.

- The bsfc and brake thermal efficiency of the other blends m40 & m50 are also close to m20 but the viscosity and density are higher which is problem for smooth engine running.

- From the overall observation it can be concluded that mustard oil could be a potential substitute for diesel fuel with a little sacrifice of power and efficiency.

- Since mustard oil has extremely limited use at present, its production for use in diesel engine will not only enable the country to attain self reliance but also help mitigate the conventional fuel crisis.

References

[1] Srivasata, A. and Prasad, R. "Triglyceride based diesel Fuels", *Renewable and sustainable Energy Reviews* 4: 111-11, 2000.
[2] A. Forhad, A.R. Rowshan, M.A. Habib, M.A. Islam, "Production and Performance of Biodiesel as as Alternative to Diesel", *ICME-2009*. TH-30.
[3] Yosimoto, Y. Onodera.M and Tamaki.H (2001), "Performance and Emission Characteristics of Diesel Engine Fuelled by Vegetable Oils", SAE paper no. 2001-01-1807/4227.
[4] Otera J., Transestrification Chem. Rev, 1993; 93 (4) : 1449-70.
[5] Freedom B, Pyre EH, Mounts TL, "Variable affecting the yield of fatty asters from tranesterification vegetable oils", J Am oil Chem soc 1984;61 (10) : 1638 43.
[6] Naik, M., Meher, L.C., Naik, S.N. and Das, L.M., (2008), "Production of biodiesel from high free fatty acid Karanja (Pongamia pinnata) oil", *Biomass and Bio-energy, Vol. 32, pp.354-357.*
[7] Altan, R., Cetinkay, S.,and Yucesu, H. S., (2001), "The potential of using vegetable oil fuels as fuel for diesel engines", *Energy Conversion and Management, Vol.42, Issue.5, pp. 529-538.*
[8] Ghormade, T. K., and Deshpande, N. V., (2002), "Soybean oil as an alternative fuels for I. C. engines", *Proceedings of Recent Trends in Automotive Fuels, Nagpur, India.*
[9] Kumar, and Reddy, V. K., (2000), "Experimental investigations on the use of vegetable oil fuels in a 4-stroke single cylinder diesel engine", *Ph.D Thesis, submitted at JNTU, Anantapur.*
[10] Huzayyin, A. S., Bawady, A. H., Rady, M. A., and Dawood, A., (2004), "Experimental evaluation of Diesel engine performance and emission using blends of jojoba oil and Diesel fuel", *Energy Conversion and Management, Vol.45, pp.2093–2112.*
[11] Narayan, C.M., (2002), "Vegetable oil as engine fuels— prospect and retrospect", *Proceedings on Recent Trends in Automotive Fuels, Nagpur, India.*
[12] Srivasata, A., and Prasad, R., (2000), "Triglyceride based diesel Fuels," *Renewable and sustainable Energy Reviews, vol. 4, No. 2, pp. 111-133.*
[13] Yosimoto, Y., Onodera, A., and Tamaki, H., (2001), "Production and Emission Characteristics of Diesel Engine Fuelled by Vegetable Oils," *The Society of Automotive Engineers,* No. 2001-01-1807.
[14] Ramadhas, A.S., Jayaraj, S. and Lakshmi Narayana Rao, K. 2002. Experimental investigation on non edible vegetable oil operation in diesel engine for improved performance. National Conference on Advances in Mechanical Engineering, J.N.T.U., Anantapur, India.
[15] ASTM Standard D88-56, " Standard Test Method for Saybolt Viscosity".
[16] ASTM Standard D240-87, "Standard Test Method for Heat of combustion of Liquid Hydrocarbon Fuels by Bomb Calorimeter".
[17] ASTM Standard D93-85, " Standard Test Method for Flash Point by Pensky-Martens Closed Tester".

6th BSME International Conference on Thermal Engineering (ICTE 2014)

Solar adsorption cooling and hot water supply for climatic condition of Dhaka

Rifat Ara Rouf[a,*], K. C. Amanul Alam[b], M. A. Hakim Khan[c]

[a]School of Engineering and Computer Science, Independent University, Bangladesh, Plot-16, Block-B, Aftabuddin Ahmed Road, Bashundhara R/A, Dhaka-1229, Bangladesh,
[b]Department of Electronics and Communication Engineering, East-West University, A/2, Jahurul Islam Avenue, Jahurul Islam City, Aftabnagar, Dhaka-1212, Bangladesh,
[c]Department of Mathematics, Bangladesh University of Engineering and Technology, Dhaka-1000, Bangladesh.

Abstract

For the climatic condition of a tropical country like Bangladesh, solar heat driven adsorption cooling seems to have great prospect. Installation cost is one of the foremost drawbacks of such a system. Although, once installed, system maintenance and operation cost is negligible. Besides, the solar unit can not only support as a cooler for adsorption space cooling purpose during summer season but also as a source of hot water supply for domestic use during the winter season. A conventional two bed basic adsorption chiller, driven by solar heat run by silica gel-water pair as adsorbent and adsorbate respectively, has been investigated for the climatic condition of Dhaka $23°46'$ N (latitude), and $90°23'$ E (longitude). 30 enhanced compound parabolic concentrator (CPC) collectors each of area 2.415 m^2 along with a hot water storage tank of volume 2.197 liters is optimum for considered climatic condition. With such a unit 30.27°C continuous water supply during the peak hours can be assured, with the storage of 44.77°C of hot water in the month of January.

Keywords: Solar heat; storage tank; hot water supply.

1. Introduction

Growing population, shortage of primary resources and demand of the modern generation ask for new ideas to search for environment friendly technologies that are easily available and within the reach of mass population. Solar

*Rifat Ara Rouf, Tel:+88-02-8401645-53; fax:+88-02-8401991.
 E-mail address:rifatara@iub.edu.bd

radiation is known to be the largest and the world's most abundant permanent and clean energy source. Compared to the annual global energy use, the amount of solar radiation intercepted by the earth's surface is much higher. In full sun, it can be safely assumed about 100 watts of solar energy per square foot [1]. If 12 hours of sun per day is assumed, this is 438,000 watt-hours per square foot per year [1]. In recent years, many promising technologies have been developed to extract sun's energy. One of these important technologies is the solar refrigeration systems which employ either absorption or adsorption technologies. Solar adsorption refrigeration devices are extremely important for vaccine and food preservations in remote areas. Due to the ability to combat against ozone depletion problem which was caused by the utilization of CFCs and HCFCs in cooling systems, thermally powered adsorption refrigeration system has gained considerable interest in recent years [2].

Absorption, adsorption and desiccant cooling are the most common technologies available in solar refrigeration and air-conditioning applications. Solar powered adsorption cooling systems, in particular, have the advantages of using clean energy and environment friendly refrigerants. Moreover, they can be driven by low temperature heat source, typically below 100° C, which can be reduced to 50° C if multi-stage scheme is performed [3- 5].

Pons and Guilleminot [6] studied solar powered adsorption system employing activated carbon-methanol pair to produce ice. Anyanwu and Ogueke [7] and Anyanwu and Ezekwe [8] studied transient analysis of solid adsorption solar refrigerator applying activated carbon-methanol as adsorbent-refrigerant pair. Sumathy et al. [9] employed activated carbon-methanol pair to study solar driven two bed adsorption air-conditioning system. Boubakri [10,11] reported new conception of adsorptive solar powered icemaker equipped with a single heat exchanger playing alternatively the role of condenser and evaporator. It shows that the daily ice production may exceed 5.2 kg, with a COP of more than 0.14 with a consistent design of the different components of adsorptive solar machine.

In the recent years, a number of researchers have investigated various aspects of solar adsorption cooling and refrigeration system like Clauss et al. [12] and Alam et al. [13]. Also for climatic condition of southern Asia mainly tropical regions [14,15] . Based on the climatic condition of Dhaka, Rouf et al. [16] investigated performance on collector area and cycle time for solar driven adsorption chiller. Later effect of the operating conditions on the performance of the system has been studied for the same conditions [17]. Lately, performance of an adsorption cooling system added with a storage tank has been discussed by Rouf et al. [18] for climatic condition of Dhaka. The present study investigates the prospect of the installation of optimum collector area only for hot summer season but also for cold winter as well as hot water supply for winter.

Nomenclature				Subscript	
A	area	$\dot{m}$	mass flow rate	cp	collector pipe
W	weight	η	collector efficiency	cr	collector
C	specific heat	U	heat transfer coefficient	tm	tank metal
T	temperature	I	solar radiation	wt	tank water

2. System description

For the climatic condition of Dhaka (Latitude $23°46'$ N, Longitude $90°23'$ E) a conventional single stage basic adsorption chiller with two beds coupled with CPC solar collectors has been discussed in Rouf et al. [13]. The working principle of same chiller when added with a storage tank is available in Rouf et al. [18]. For both cases silica gel -water pair has been considered as adsorbent and adsorbate respectively. The basic adsorption cycle consists of two adsorbent beds one condenser and one evaporator. The principle of basic adsorption cycle is available in literature [21]. The solar collector panels are connected to the adsorbent beds alternately. The storage tank is connected with the adsorbent beds and the solar collector panels. Water is heated in the solar collector and transported to the bed. The outflow of this hot water from the bed is then collected in the reserve tank. Reserve tank supplies water in the collector again. Schematic of adsorption solar cooling system with storage tank is given in Fig. 1. The working principle of the chiller with heat storage tank is available in Rouf et al. [18].

In winter, since cooling is not required, the valves between collector and beds, reserve tank and beds are closed. The collector panel is connected with reserve tank directly. Tank supplies hot water for household use and also to the collector. The amount of outflow of tank water for household is filled up with same amount of inflow of water of ambient temperature during day time. Tank size is same as the tank considered in [18]. Weight of water in reserve tank is half of that of the weight considered in [18]. Schematic of the tank and collector water flow chain is presented in Fig. 2 and Fig. 3 of both designs respectively. The operating conditions of the chiller are available in [13] while the supply chain and reserve tank specifications are presented in table 1.

In order to run a continuous supply of hot water for house hold use during the peak hours, 22 collectors are added with one storage tank (with considered specification). While, on the other hand in order to store hot water heated inside the collector and to reserve it in the reserve tank, a closed hot water fill is considered, without any outflow for household during day time, remaining 8 collectors are added with a second tank of same specification. However, in this case, reserved hot water will be stored in intension to be utilized during night time when solar radiation is absent. The schematic of the continuous household water supply and closed hot water fill is given in Fig 2 (a) and (b) respectively.

Table 1. Design of reserve tank

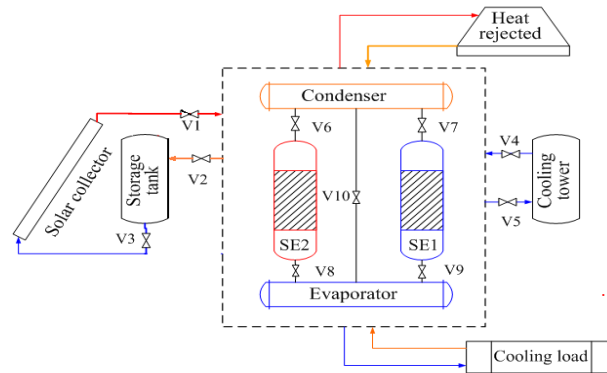| Symbol	Description	Value
LHW	Dimension of the tank	1.3 m
W_{tv}	Volume of the tank	$1.3^3\,m^3$
W_{wt}	Weight of water in reserve tank	W_{tv}x500-10 kg
U_{tloss}	Reserve tank heat transfer loss coefficient	$0.5\ W/m^2K$
AS_{rt}	Reserve tank outer surface area	$6x1.3^2\,m^2$
W_{tm}	Reserve tank metal weight	A_{wt}x0.005x2700kg

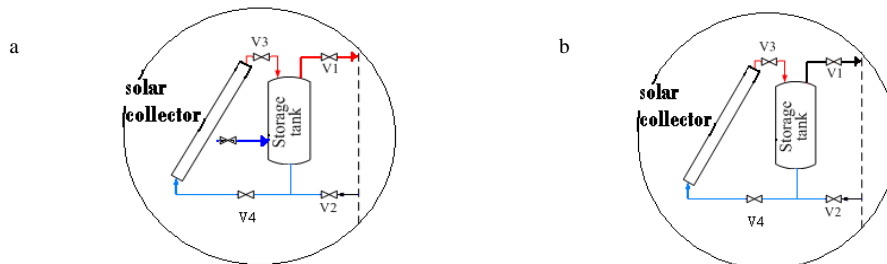Fig.1. Schematic of solar heat driven adsorption cooling system with heat storage

Fig.2. (a) Schematic of hot water chain design 1; (b) Schematic of hot water chain design 2

2.1. Mathematical modeling and simulation procedure

The mathematical model for the solar adsorption chiller with storage tank is available in Rouf et al. [18]. Water supply from the collector to reserve tank and from reserve tank to collector is considered to be 1 kg/s. While the outflow of the reserve tank for household and inflow to reserve tank of water of ambient temperature is equal and it is 0.5 kg/s. Exploiting a lumped parameter model, the energy balance equation for collector are;

$$W_{crM,i} \frac{dT_{cr,i}}{dt} = \eta_i A_{cr,i} I + \dot{m}_{f,cr} C_f \left(T_{\tan k} - T_{cr,i,out}\right) \tag{1}$$

$$T_{cr,i,out} = T_{cr,i} + \left(T_{\tan k} - T_{cr,i}\right) \exp\left(-\frac{U_{cp,i} A_{cp,i}}{\dot{m}_{f,cr} C_f}\right) \tag{2}$$

And energy balance equation of the reserve tank is;

$$\frac{d}{dt}\left\{\left(W_{tm} C_{tm} + W_{wt} C_w\right) T_{wt}\right\} = \dot{m}_w C_w \left(T_{cr,out} - T_{wt}\right) + U_{tloss} AS_{rt} \left(T_{am} - T_{wt}\right) - \dot{m}_w C_w \left(T_{wt} - T_{am}\right) \tag{3}$$

Also, for the second case, there is no drain of water from the reserve tank for household and therefore no fill in the tank, the energy balance equation is;

$$\frac{d}{dt}\left\{\left(W_{tm} C_{tm} + W_{wt} C_w\right) T_{wt}\right\} = \dot{m}_w C_w \left(T_{cr,out} - T_{wt}\right) + U_{tloss} AS_{rt} \left(T_{am} - T_{wt}\right) \tag{4}$$

The differential equations has been dealt with implicit finite element method while logical programming language FORTRAN with Compaq visual Fortran compiler has been exploited to obtain the numerical solution of the proposed model.

3. Result and discussion

The climatic data for Dhaka station has been supported by Bangladesh meteorology department (BMD) while solar radiation data has been supported by Renewable energy research center (RERC), University of Dhaka. During April maximum temperature has been recorded as 34°C while it is 21.8°C in January in the year of 2003. For the climatic condition of Dhaka, during the hot Summer namely in April, 14 collectors are enough to raise adsorption bed temperature to the desired level to run the proposed chiller with direct solar coupling Rouf et al. [16]. While for maximum cooling capacity optimum collector number is 22 in this case. When a storage tank of size 2.197 m^3 is added with the chiller, it need more collectors compared with direct solar coupling to raise adsorption bed temperature in order to run the chiller, Rouf et al. [18]. However, optimum performance is obtained with 30 collectors. Furthermore, addition of the storage tank enhances system activation hour beyond sunset hours. Two different designs have been studied based on the performance [19]. Figure 3 represent comparative cyclic average cooling capacity (CACC) of both system with optimum collector area. Both of these studies have been conducted for the month of April, since it is the first month of Summer season and from the month of May Monsoon will start and it is difficult to get uninterrupted solar radiation. Hence, 30 collectors are considered to be the optimum collector area for the climatic condition of Dhaka to be installed.
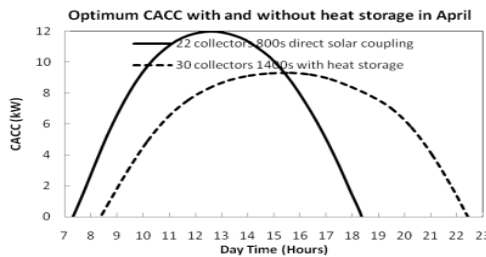

Fig.3. Comparative CACC with direct solar coupling and with storage tank for optimum collector area and cycle time

The cooling capacity using 22 collectors with direct solar coupling for the month of April and January is depicted in Fig. 4. It is seen that maximum 4.5 kW cooling capacity is produced in peak which can be used for air-conditioning purpose if it requires cooling during the period winter session at peak hour. During January minimum temperature is recorded as 11°C while maximum temperature is recorded as 21.8ºC for the climatic condition of Dhaka. The average day time temperature is around 16ºC. Therefore, neither cooling nor room heating is essential for this region during winter. But again, the modern architectural buildings are designed in such a way so that the temperature of the room needs to be controlled. Also there is no ventilation in these types of buildings. Thus, some cooling production is needed for comfortable work environment. Furthermore, beyond room cooling, once installed, the CPC collectors could be utilized for use of household hot water supply to utilize in cooking, bathing and other house hold courses. This will save primary energy used in cooking such as use of natural gas or other primary fuels, electricity driven water heater for faucets and bathing.

Figure 5 illustrates energy distribution when 22 collectors are utilized to produce cooling during the month of January when no storage tank is added with the system. In this month 22 collectors can collect 486.552 MJ heat from solar radiation during the whole day, out of which 217.469 MJ is used for cooling production. That is only 44% of total energy collected can be utilized for cooling purpose. The rest of 269.1 MJ heat remains unused and is lost in the environment. When cooling is not considered necessary, the unit can be utilized as a heat supplier in winter.

According to State of Colorado estimate [20] a minimum well yield of 4 to 10 gallons per minute is recommended for household. That includes shower and bath, faucet, toilet and cloth washing. Hence an average of 8 gallons of water per minute can be considered to be consumed for household in each day during peak demand in Dhaka. Thus, using 22 collectors and considering system design 1, a continuous supply of hot water of temperature 30.27°C can be provided for house hold use at the peak hours (Fig. 6(a)). Whereas, with the rest of 8 collectors another tank of same size (as of system design 2) can store hot water of temperature 44.77°C to be used after sunset for house hold courses (Fig. 6 (b)).

4. Conclusion

Based on the above discussion it can be concluded that for a tropical region like Dhaka, 30 CPC collectors each of area 2.415 m^2 can be installed in intension to run a solar heat driven adsorption cooling system along with a heat storage tank of volume 2.196 liters without any loss of generosity. As once installed, 72.45 m^2 collector area can be utilized not only for cooling purpose during hot summer season but also as a source of supply of hot water during winter to save other primary fuels such as natural gas, coal or electricity.
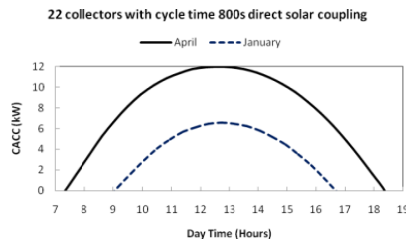

Fig. 4. Comparative CACC with direct solar coupling for January and April with optimum collector area and cycle time
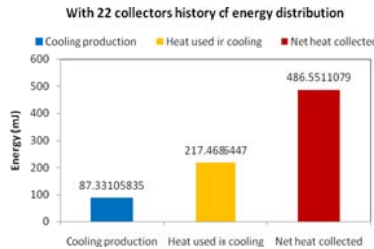

Fig. 5. Energy distribution diagram for January with direct solar coupling
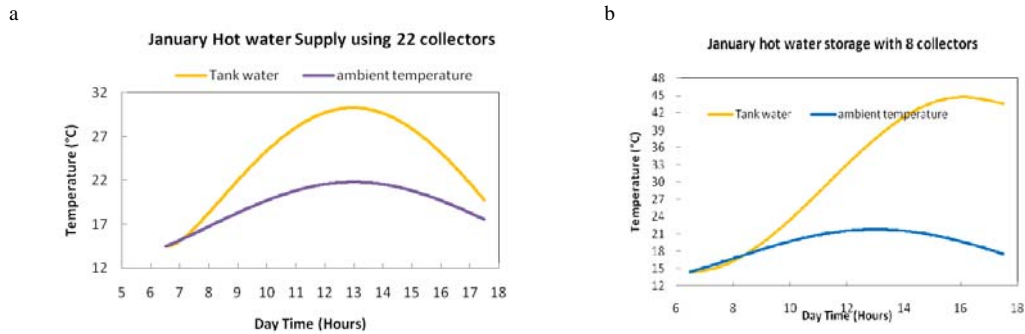
a

b

Fig. 6. (a) Hot water supply chain with continuous household supply; (b) with no household supply

Acknowledgements

References

[1] www.ecoworld.com/energy-fuels/how-much-solar-energy-hits-earth.html (viewed on 28 June 2014).

[2] D.C. Wang, Y.J. Wang, J.P. Zhang, X.L. Tian, J.Y. Wu, Experimental study of adsorption chiller driven by variable heat source, Energy Conversion and Management, 49 (2008) 1063-1073.

[3] B. B. Saha, E. C. Boelman, T. Kashiwagi, Computer simulation of a silica gel–water adsorption refrigeration cycle-the influence of operating conditions on cooling output and COP. ASHRAE TRANS., 101 (1995) 348–57.

[4] B. B. Saha, S. Koyama, T. Kashiwagi, A. Akisawa, K. C. Ng, H. T. Chua, Waste heat driven dual-mode, multi-stage, multi-bed regenerative adsorption system. International Journal of Refrigeration, 26 (2003) 749–57.

[5] K. C. A. Alam, M. Z. I. Khan, A. S. Uyun, Y. Hamamoto, A. Akisawa, T. Kashiwagi, Experimental study of a low temperature heat driven re-heat two-stage adsorption chiller, Applied Thermal Engineering, 27 (10) (2007) 1686-1692.

[6] M. Pons, J.J. Guilleminot, Design of an experimental solar powered, solid adsorption ice maker, Journal of Solar Energy and Engineering, (Trans. ASME), 103 (4) (1986) 332-337.

[7] E.E. Anyanwu, N.V. Ogueke,Transient analysis and performance prediction of a solid adsorption solar refrigerator, Applied Thermal Engineering, 27 (2007) 2514-2523.

[8] E.E. Anyanwu, C.I. Ezekwe, Design, construction and test run of a solid adsorption solar refrigerator using activated carbon/methanol as adsorbent/adsorbate pair, Energy Conversion and Management, 44 (18) (2003) 2879-2892.

[9] K. Sumathy, Li Yong, H. Muller Steinhagen, H. Kerskes, Performance analysis of a modified two-bed solar-adsorption air-conditioning system, Int. J. Energ. Res. 33 (2009) 675-686.

[10] A. Boubakri, A new conception of an adsorptive solar epowered ice maker, Renewable Energy, 28 (2003) 831-842.

[11] A. Boubakri, Performance of an adsorptive solar ice maker operating with a single double function heat exchanger (evaporator/condenser), Renewable Energy, 31 (2006) 1799-1812.

[12] M. Clausse, K. C. A. Alam, F. Meunier, Residential air conditioning and heating by means of enhanced solar collectors coupled to an adsorption system, Solar Energy, 82(10) (2008) 885-892.

[13] K. C. A. Alam, B. B. Saha and A. Akisawa, Adsorption cooling driven by solar collector: a case study for Tokyo solar data, Applied Thermal Engineering, 50 (2) (2013) 1603-1609.

[14] I. I. El-Sharkawy, H. A. Meguid, B. B. Saha, Potential application of solar powered adsorption cooling systems in the Middle East, Applied Energy, 126 (2014) 235-245.

[15] K. Habib, B. B. Saha, A. Chakraborty, S. T. Oh, S. Koyama, Study on solar driven combined adsorption refrigeration cycles in tropical climate, Applied Thermal Engineering, 50 (2013) 1582-1589.

[16] R. A. Rouf, K. C. A. Alam, M. A. H. Khan, T. Ashrafee, M. Anwer., Solar Adsorption cooling: A case study on the climatic condition of Dhaka. Journal of Computers, 8(5) (2013) 1101-1108.

[17] R. A. Rouf, K. C. A. Alam, M. A. H. Khan, Effect of operating conditions on the performance of adsorption solar cooling run by solar

collectors, Procedia Engineering, 56 (2013) 607-612.

[18] R. A. Rouf, K. C. A. Alam, M. A. H. Khan, B. B. Saha, F. Meunier, M. A. Alim, K. M. A. Kabir, Advancement
of solar adsorption cooling by means of heat storage, Proceedings of 10th International Conference on Mechanical Engineering, ICME 2013, 2014.

[19] K. C. A. Alam, R. A. Rouf, M. A. H. Khan, K. M. A. Kabir, Performance Analysis of Solar Adsorption Cooling System – Effect of Position
of Heat Storage Tank, Proceedings of 18th International Mathematics Conference 2013, 2014, pp. 207-209.

[20] leg.mt.gov/conlent/committees/Interim/2007_2008/water_policy/staffmemos/typicalneed.pdf (viewed on 14 May, 2014).

[21] B. B. Saha, E. C. Boelman, T. Kashiwagi, Computer simulation of a silica gel-water adsorption refrigeration cycle- the influence of
operating conditions on cooling output and COP,ASHREA Transactions, 101(2) (1995) 348-357.

6th BSME International Conference on Thermal Engineering (ICTE 2014)

Performance Test of Double-stage Rankine Cycle experimental plant for OTEC

Eisuke Kusuda[a,*], Takafumi Morisaki[b], Yasuyuki Ikegami[b]

[a]Dept.of Mechanical Engineering Saga University, 1, Honjo-machi, Saga-shi, Saga 840-8502, Japan
[b]Institute of Ocean Energy Saga University(IOES), 1-48, Hirao, Yamashiro-cho, Imari-shi, Saga 849-4256, Japan

Abstract

Ocean thermal energy conversion has gained focus generating stable electric power while providing additional benefit. By some research, it is shown that using a double-stage Rankine cycle is theoretically more efficient than a single-stage Rankine cycle. Moreover, several studies have been made on the experimental study of a double-stage Rankine cycle. But the comparison of theoretical result with experimental result has never been studied so far. In this research, it was demonstrated a double-stage Rankine cycle experimental plant, and attempted to compare experimental result with theoretical result.
© 2015 The Authors. Published by Elsevier Ltd.
Peer-review under responsibility of organizing committee of the 6th BSME International Conference on Thermal Engineering (ICTE 2014).

Keywords: Ocean thermal energy conversion, Double-stgae Rankine cycle, *Entropy generation rate*, *Working fluid flow rate distribution ratio* ;

1. Introduction

In recent years, renewable energy is refocused because global warming and energy problems have received more attention. There are various kinds in renewable energy. One of them is Ocean thermal energy conversion called OTEC. OTEC plant is basically a heat engine that utilizes the temperature difference between the warm surface water and deep cold seawater to drive a turbine to produce electricity, using the principles of a Rankine cycle (Figure.1 (a)). OTEC systems could be provided that not only a stable source of electricity, but also produces desalinated fresh water, cooling for aquaculture. Also, an enormous amount of this potential energy is stored in the Earth's oceans. Compared to fossil fuels and nuclear energy generation, OTEC has a low energy density and a low temperature difference. With present designs operating only 3-4% efficiency, OTEC systems must be improved before they can be considered to be a practical form of energy generation.

In order to improve the heat efficiency of OTEC systems, an ammonia/water mixture, as suggested by Kalina, can be used [1]. Using ammonia/water mixture decreases the irreversible losses in the heat exchange process and improves

overall performance. However, Panchal have reported that the mixture lowers the heat transfer coefficient and usable temperature difference due to the change in the concentration boundary layer [2].

Therefore, using a multi-stage Rankine cycle is gathering attention as one of the methods to minimize the irreversible losses in the heat exchange process. Multi-stage Rankine cycle has plural independent Rankine cycles. The heat source passes each heat exchanger sequentially. Multi-stage Rankine cycle is used pure medium as working fluid (Ammonia, Freon).

This research focuses on the results using a double-stage Rankine cycle (D-R). Fig.1 (b) shows the process flow diagram for the double-stage Rankine cycle. It is broken down into two independent Rankine cycles identified as Cycle-Nop.1 (High temperature) and Cycle-No.2 (Low temperature). Warm water is passes evaporator of Cycle-No.1 and is flowed directly to the evaporator of Cycle-No.2. Similarly, cold water is passes through the condenser of Cycle-No.2 and is flowed directly to the condenser of Cycle-No.1.

It is evident from the research of Morisaki and Ikegami [3, 4] that the theoretical efficiency of a multi-stage Rankine cycle improves upon a single-stage Rankine cycle (S-R), and maximum power output of a multi-stage cycle is expected to rise by up to double compared to a single-stage cycle [5]. Moreover, several studies have been made on the theoretical study of a double-stage Rankine cycle. Single-stage OTEC systems and the mixture cycle were already examined theoretically and experimentally before [6-9]. In the case of a double-stage Rankine cycle, it has been reported that the operation conditions affect the system characteristics and performance.

On the other hand, the comparison of theoretical result with experimental result has never been studied so far. In this research, it was demonstrated a double-stage Rankine cycle experimental plant, and attempted to compare the experimental results with the theoretical results.
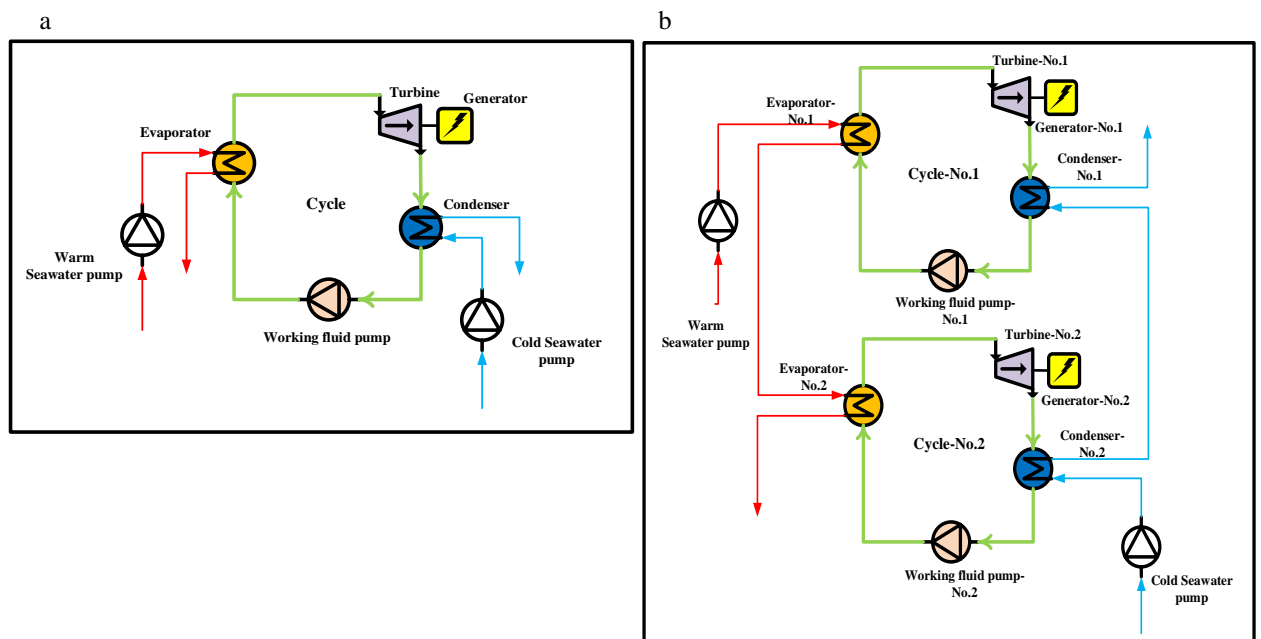

Fig. 1. (a) Single-stage Rankine cycle flow; (b) Double-stage Rankine cycle flow.

2. Experimental equipment

2.1. Heat exchanger

The evaporator and condenser used by two units each because total heat transfer area of a double-stage Rankine cycle and a single-stage Rankine cycle was equal. There are valves in the duct of each heat exchanger. The valve can choose heat exchanger to use. Therefore, it can change the number of stage of Rankine cycle. The form of heat transfer surface in evaporator and condenser is herringbone pattern. High temperature fluid and low temperature fluid were alternately rolled by countercurrent in the duct between each plate, then heat exchanger is performed.

2.2. Heat source pump

Water which heated in boiler or cooled in refrigerator was used as heat source in this experiment. Because the influence of pollution films such as heat exchangers were excluded. The flow rate of heat source was regulated by controlling the warm and cold water pump with inverter each.

2.3. Measuring instrument

The volume flow of heat source was measured by electromagnetic flowmeter, and mass flow rate with the liquid phase of working fluid was measured by Coriolis flowmeter. The experimental data such as temperature, pressure, the flow rate are imported to process computer. At the same time, the measuring date can be displayed to process computer. Displayed all data to screen were updated automatically

3. Experimental methods

Using experimental equipment in this research is shown in Figure.2. Table.1 show experimental conditions in this research. Tetrafluoroethane (HFC-134a) was selected as the working fluid. Water which heated in boiler or cooled in refrigerator was used as heat source. The working fluid flow rate distribution ratio in Cycle-No.1 and Cycle-No.2 was changed 3:7 ~ 7:3. Then the total working fluid flow is constant. Measurements were taken for a 5-min period after the system had stabilized. To simulate a turbine, a pressure-reducing valve was used, meaning the power output and thermal efficiency were not measured. Instead, the temperature of the cold and warm water sources and the working fluid was measured. The irreversible losses in the heat exchange process were assessed by calculating the entropy generation rate of the system. The influence of the irreversible losses in heat exchange process on the working fluid flow rate distribution ratio is examined. The formula for the entropy generation rate [6] is shown below.

$$S_{gen} = m_H \left(S_{in} - S_{out} \right)_H + m_L \left(S_{in} - S_{out} \right)_L \tag{1}$$

The value m_H represents the flow rate of the warm source, also m_L represents the flow rate of the cold source. The values S_{in} and S_{out} represent the specific entropy at the input and output, respectively.

Table 1. Experimental conditions.

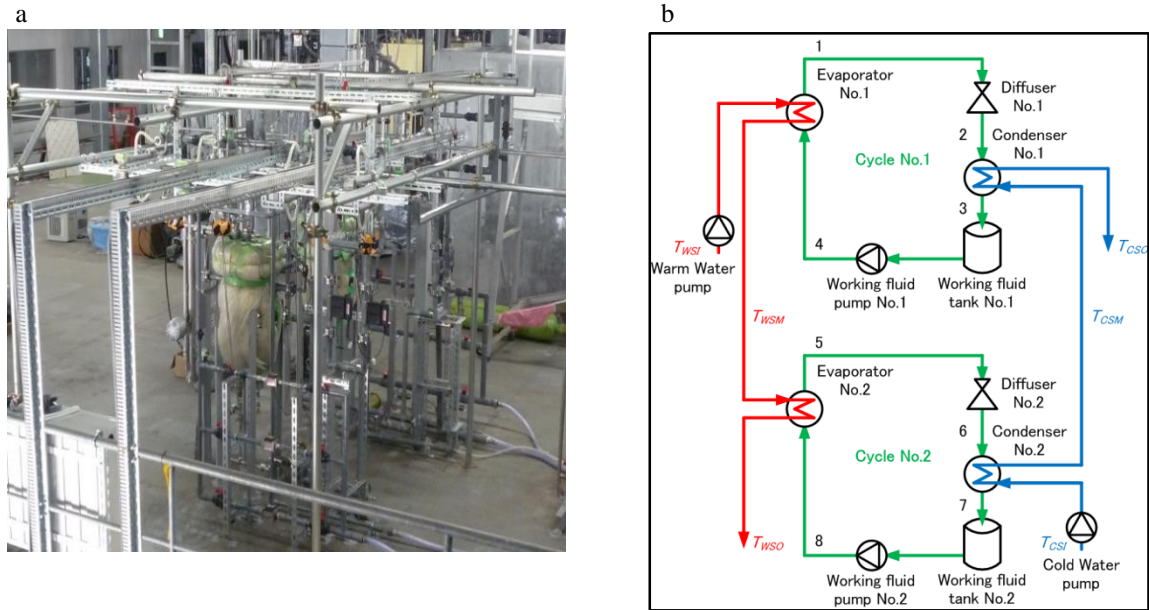| Item	Sign	Unit	Value
Warm water temperature	T_{WSI}	[°C]	28
Cold water temperature	T_{CSI}	[°C]	7
Warm water flow rate	m_{WS}	[kg/h]	500
Cold water flow rate	m_{CS}	[kg/h]	500
Working fluid flow rate	m_{WF}	[kg/h]	100
Heat transfer area	A	[m^2]	0.064

a

b

Fig. 2. (a) Experimental equipment used; (b) Schematic diagram of a double-stage Rankine cycle

4. Results

4.1. Theoretical calculation results

Figures 3 and 4 show theoretical calculation result. Theoretical calculation method is derived by Morisaki and Ikegami [3, 4]. Figure.3 shows the entropy generation rate with the working fluid flow rate distribution ratio in Cycle-No.1 with Cycle-No.2. The dashed line shows the entropy generation rate of the evaporator in Cycle-No.1, $S_{genE,1}$; the two dot chain line shows the entropy generation rate of the evaporator in Cycle-No.2, $S_{genE,2}$; the dotted line shows the sum of the entropy generation rate of evaporator between Cycle-No.1 and Cycle-No.2, S_{genE}; and the solid line shows the sum of the entropy generation rate between the evaporator and the condenser, S_{gen}. The entropy generation rate of the evaporator in Cycle-No.1 increased with an increase the working fluid flow rate distribution ratio and the entropy generation rate of evaporator in Cycle-No.2 decreased. Therefore, the sum of the entropy generation rate in evaporator between Cycle-No.1 and Cycle-No.2 was minimized when working flow rate distribution ratio of Cycle-No.1 with Cycle-No.2 was 1:1. As a result, the sum of the entropy generation rate between the evaporator and the condenser was minimized when working flow rate distribution ratio of Cycle-No.1 with Cycle-No.2 was 1:1.

Figure 4 shows the power output and the thermal efficiency of cycle with the working fluid flow rate distribution ratio in Cycle-No.1 with Cycle-No.2. The solid line shows the power output, W; the dotted line shows the thermal efficiency of cycle, η_{th}. It shows that the power output and the thermal efficiency of cycle were the greatest when working flow rate distribution ratio of Cycle-No.1 with Cycle-No.2 was 1:1. In other words, it indicates that the entropy generation rate is minimized and the power output and the thermal efficiency of cycle is peak when working flow rate distribution ratio of Cycle-No.1 with Cycle-No.2 is 1:1 in theory.

4.2. Experimental results

Figures 5-7 show the experimental results. Figure.5 shows the change in the evaporation and condensation temperatures with the working fluid flow rate distribution ratio in Cycle-No.1 with Cycle-No.2. The solid line shows the evaporation and condensation temperatures of the double-stage Rankine cycle, the two dot chain line shows the evaporation temperature of the single-stage Rankine cycle and the dashed line shows the condensation temperature of the single-stage Rankine cycle. It shows that the evaporation temperature of the double-stage Rankine cycle is larger

than that of the single-stage Rankine cycle. Also, the condensation temperature of the double-stage Rankine cycle is smaller than that of a single-stage Rankine cycle. Therefore, using temperature difference in the working fluid flow of the double-stage Rankine cycle is larger than the single-stage Rankine cycle.

Figure 6 shows the change in temperature with the entropy ratio of Cycle-No.1 and Cycle-No.2 when working fluid flow rate distribution ratio is 1:1. The T-s diagram clearly shows that the evaporation and condensation temperatures in the working fluid of a double-stage Rankine cycle are closer to the heat source temperatures than the single-stage Rankine cycle. Therefore, the irreversible losses in heat exchange process of the double-stage Rankine cycle are less than that of the single-stage Rankine cycle. Also, using temperature difference in the working fluid of the double-stage Rankine cycle is larger than that of the single-stage Rankine cycle. The area of square in working fluid flow means the power output in the T-s diagram. Therefore, it can be expected that the double-stage Rankine cycle generates a greater power output than the single-stage Rankine cycle.

Figure 7 shows the entropy generation rate with the working fluid flow rate distribution ratio in Cycle-No.1 with Cycle-No.2. The entropy generation rate of a double-stage Rankine cycle is minimized when working flow rate distribution ratio of Cycle-No.1 with Cycle-No.2 is 1:1. Also, entropy generation rate of a double-stage Rankine cycle is less than that of a single-stage Rankine cycle. As a result, the optimum operating condition of working fluid flow rate ratio between Cycle-No.1 and Cycle-No.2 is 1:1. On the other hand, the variation of experimental entropy generation rate is small, in comparison with theoretical result. The quality was defined by experimental result, but theoretical result didn't defined it. As a result, it was considered that the experimental vapour flow rate is less than theoretical result.
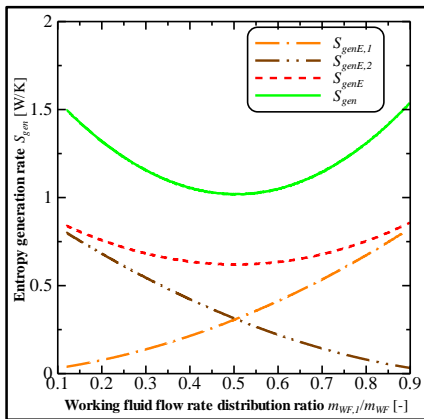

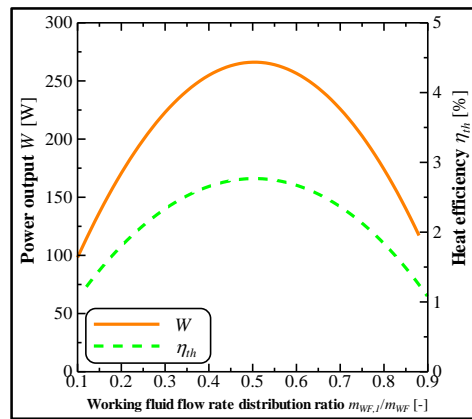Fig. 3. Entropy generation rate in evaporator(CAL).

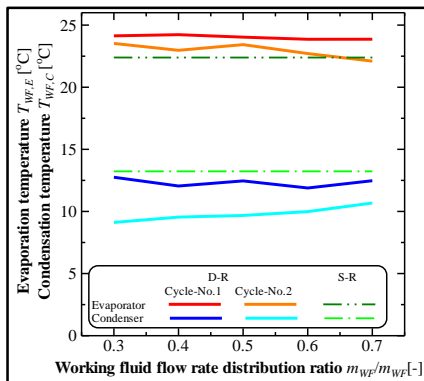Fig. 4. Power output and the thermal efficiency of cycle (CAL)
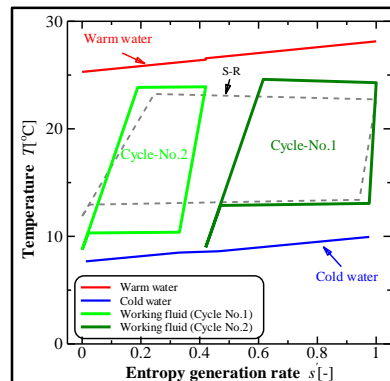

Fig. 5.Evaporation and condensation temperatures.
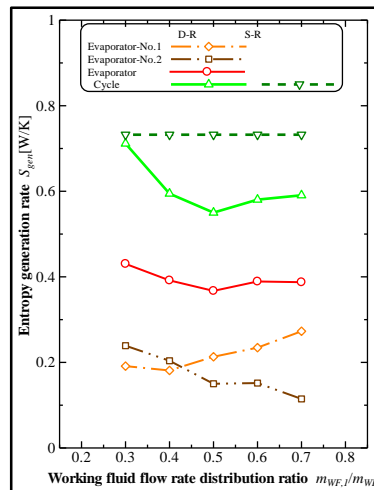

Fig. 6. Conceptual T-s' diagram (1:1).

Fig. 7. Entropy generation rate (EXP).

5. CONCLUSION

In this research, it was demonstrated the experimental plant of double-stage Rankine cycle, and compared experimental result with theoretical result. The variation of experimental entropy generation rate is small, in comparison with theoretical result. The quality was defined by experimental result, but theoretical result wasn't defined it. As a result, it was considered that the experimental vapour flow rate is less than theoretical result.

It was clarified that the entropy generation rate of a double-stage Rankine cycle was minimized when working fluid flow rate distribution ratio of Cycle-No.1 and Cycle-No.2 is 1:1. Then, entropy generation rate of a double-stage Rankine cycle was less than the single-stage Rankine cycle. Also, the using temperature difference in the working fluid of the double-stage Rankine cycle was larger than those of a single-stage Rankine cycle. Therefore, it could be expected that a double-stage Rankine cycle generates a greater output than a single-stage Rankine cycle experimentally.

By this experiment, to simulate a turbine, a pressure-reducing valve was used, meaning the power output and thermal efficiency were not measured. After this, to make an experiment mounting turbine and to consider system characteristic.

References

[1] Kalina A.I. Generation of energy by means of a working fluid, and regeneration of a working fluid. United States Patent 4346561; 1982.
[2] Panchal, CB, et al. OTEC performance tests of the Trane plate-fin heat exchanger. US DOE Report, ANL/OTEC-PS-7; 1981
[3] T. Morisaki, Y.Ikegami. Comparison between the conventional method and a new developed method for calculating a multi-stage Rankine cycle, (in press)
[4] Y. Ikegami, T. Morisaki. OTEC Using Multi-stage Rankine Cycle. Proceedings of 23rd International Offshore and Polar Engineering Conference; 2013, pp. 451–456.
[5] T.Morisaki, Y.Ikegami. Maximum power of a multistage Rankine cycle in low-grade thermal energy conversion. *Applied Thermal Engineering*. 69; 2014, pp.78-85
[6] Bejan. A.The thermodynamic design of heat and mass transfer processes and devices. International Journal of Heat and Fluid Flow; 1987, pp. 258–276.
[7] Y.Ikegami, K.Urata, J.Inadomi, H. Goto, T.Morisaki, K.Inoue, S.Goto. Investigation on the stability of OTEC system using ammonia/water mixture as working fluid by continuous operation for two weeks. Proceedings of 20rd International Society of Offshore and Polar Engineering Conference; 2010
[8] Kalina A.I. Combined Cycle System with Novel Bottoming Cycle. Transactions of the ASME Journal of Gas Turbine. Vol.106. No.4; 1984, pp.737-742.
[9] S.JITSUHARA, Y.Ikegami, H.Uehara. Optimization of Design Conditions for OTEC (In the case of annual Operation Performance). Japan Society of Mechanical Engineers collection of papers. Vol.60. No.570; 1994, pp.291-298.

6th BSME International Conference on Thermal Engineering (ICTE 2014)

An experimental study of a cyclonic vertical axis wind turbine for domestic scale power generation

Bavin Loganathan, Harun Chowdhury*, Israt Mustary and Firoz Alam

School of Aerospace, Mechanical and Manufacturing Engineering, RMIT University, Melbourne, 3083, Australia

Abstract

The primary objective of this paper is to investigate a cyclonic domestic scale vertical axis wind turbine with semicircular shaped blades under a range of wind speeds. A 16-bladed rotor was initially designed and its torques and angular speeds were measured over a range of wind speeds using a wind tunnel. Additionally, a cowling device was developed to enhance the turbine efficiency by directing the air flow from the rear blades into the atmosphere. Another 8-bladed rotor was also manufactured to investigate the effect of blade number on the maximum power generation. The aerodynamic performance of the cowling device was also investigated. Maximum power curves as a function of wind speeds were established for each configuration. The results indicated that the 16-bladed wind turbine can be used for domestic scale wind power generation. The results show that the cowling device has positive effect to increase the rotor speed to a significant amount. With the use of the cowling device, the average rotor speed increased by about 26% for the 16-bladed rotor compared to the baseline configuration. A significant increase (about 40%) of rotor speed was also found for the 8-bladed rotor with the cowling device. The results also indicated that the cowling device can be used to increase the power output of this cyclonic type vertical axis wind turbine especially with a reduce number of blades.

* Corresponding author. Tel.: +61 3 99256103; fax: +61 3 99256108.
  E-mail address: harun.chowdhury@rmit.edu.au

1. Introduction

The increasing awareness of global warming and climate change, diminishing fossil fuel energy sources, and tightening carbon emission target require the development of renewable energy resources to generate power [1-4]. Over decades, many research works have been carried out to investigate and enhance the power generation performance of various wind turbine configurations. Most of these research studies have been focused on large scale horizontal axis wind turbines (HAWTs) and vertical axis wind turbines (VAWTs) installations in open areas or fields with a constant undisturbed wind source. However, limited research has been focusing on wind power generation in built up areas [5-6]. In urban and built-up area, the atmospheric wind becomes highly turbulent and exhibits significant fluctuations of gust speed and high variability of wind direction caused by the urban structures and buildings. Under such conditions, existing HAWTs are not effective power generators. On the other hand, despite having some advantages (fewer moving parts, lower tip speed ratio, quieter, lower cost, & insensitive to wind direction) over HAWT, VAWTs currently used in urban applications do not produce much more appreciable power [7]. One of the major limitations of current VAWTs is the negative torque. This restricts the rotor from accelerating to higher torque producing speeds. There are two ways this negative torque is produced. The first negative torque is produces on the returning blade (convex side). The second negative torque is produced on the rear blades when the swept airflow moves through the rotor and tries to exit at the rear. This exiting airflow impedes the returning blade. In addition, the exiting air stream is directed back into the path of the approaching wind, creating a turbulent zone which not only introduces losses and minimizing efficiency, but also creates pressure fluctuations that cause vibrations in the rotor and the surrounding mountings.

Over the years, researches have tried to improve the performance of VAWT. Ogawa et al. [8] examined the effect of flow deflector plate and found that the rotor power increases nearly 30 percent. Irabu and Roy [9] studied the effect of surrounding the turbine with a guide box and found increases about 1.5 times with three blades and 1.23 times with two blades greater than that without guide-box tunnel, respectively. Altan et al. [10] found that the maximum power coefficient of the Savonius wind rotor is increased to about 38.5% with the optimum curtain arrangement. These studies prove that we can increase the efficiency of a Savonius rotor by using enhancements.

This study builds on top of a previous work carried out by Alam et al. [11] using RMIT Industrial wind tunnel. As an alternative to existing VAWT systems (e.g., Savonius, Nautilus or Darrieus), a novel concept of Cyclonic Vertical Axis Wind Turbine (CVAWT) which diverts the incoming wind upward and makes use of the stack effect to extract more wind power as it exits through a cowling system. Preliminary testing using a card board model of a CVAWT was carried out by Alam et al [11]. The CVAWT was tested with two configurations over a range of wind speeds (5 to 30 km/h). The first configuration was the bare rotor without a cowling and the other configuration was the bare rotor shrouded with a cowling. Only the speeds of the rotor with these two configurations were tested and their study indicated an increase of rotor speed over 130% with the cowling. However, the study neither considered the effect of the number of blades nor measured the rotor torque and angular velocity which is an important parameter to determine the possible power generation by a wind turbine. Therefore, the main purpose of this study is to measure the power output of a model CVAWT for four different configurations using better construction material (e.g., fiber glass) and considering the effect of number of blades.

Nomenclature	
N	rotor speed (rpm)
ω	rotor speed (rad/s)
T	torque (Nm)
P	power (W)

2. Experimental methods

2.1. Wind turbine rotor design

The Savonius blades were modeled on a variation of classic Savonius rotor. The VAWT used for this study is a semicircle shaped blade made from fiber glass material. The rotor radius is 150 mm and the height of each blade is 75 mm. Two rotors: one with 16 blades and another with 8 blades were constructed. The schematic of the rotors are shown in Fig. 1(a) and Fig. 1(b) shows a 3D model of the assembly for 16-bladed turbine rotor.
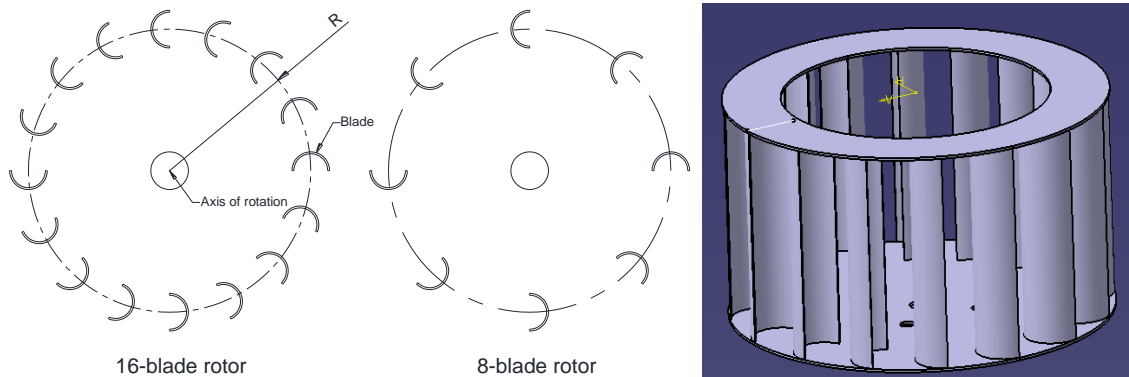

Fig. 1. (a) schematic of wind turbine rotors; (b) 3D model of the 16-blade rotor.

2.2. Cowling design

The main function of the cowling is to eliminate the negative torques which prevents the rotor from accelerating to higher torque producing speeds. Therefore, a cowling was designed in such a way that it can enclose the turbine rotor with a small clearance and can guide the incoming wind through a defined inlet and push the rotor and finally channel out the wind through the confined outlet to the environment. The cowling was constructed with two hollow PVC cylinders. The outer cylindrical shell is 360 mm in diameter and half of its frontal area is kept closed to prevent the incoming wind hitting the convex side of the returning blade. The inner shell with 160 mm diameter has an opening to allow the swept wind to exit the turbine through the top instead of at the rear to eliminate the second negative torque. Fig. 2(a) shows the 3D model of the cowling and Fig. 2(b) represents the rotor fitted with the cowling.
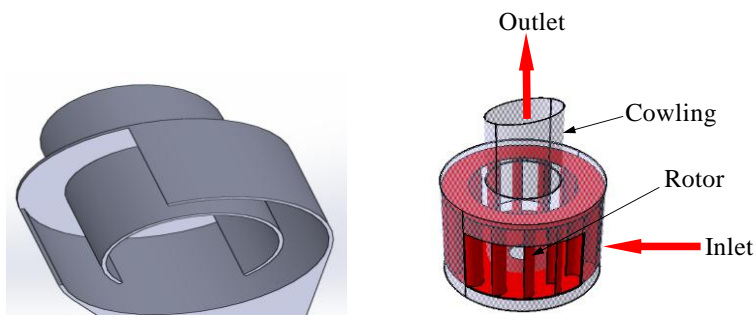

Fig. 2. (a) cowling device; (b) wind turbine rotor including the cowling.

2.3. Wind tunnel testing

Tests were undertaken at RMIT Industrial Wind Tunnel. It is a closed return circuit wind tunnel with a rectangular test section (3 m width, 2 m height and 9 m length). The maximum wind speed of the tunnel is approximately 145 km/h. More details of the wind tunnel can be found in Alam et al. [11]. To measure various parameters (i.e., torque, rotor speed) at different wind speeds, the experimental setup was positioned and fixed at the middle of the wind tunnel test section. Two different rotors with different numbers of blade (i.e., 16 and 8 blades) without any cowling device were measured. Following four wind turbine configurations were investigated:

(a) 16-blade rotor without cowling
(b) 8-blade rotor without cowling
(c) 16-blade rotor with cowling and
(d) 8-blade rotor with cowling

The rotor was connected to a torque transducer (model: T20WN, manufactured by HBM GmbH, Germany) and a mechanical breaking system through a circular rod and bearing supports. The setup was fixed properly to the wind tunnel floor to minimize vibration which may cause measurement errors. The setup was positioned 150 mm above the tunnel floor to minimize boundary layer effect. Fig. 3(a) shows the schematic of the experimental setup and Fig. 3(b) shows the experimental setup inside the RMIT Industrial Wind Tunnel. Opening of the cowling was positioned at 90 degree relative to wind direction for both rotor configurations. The torque transduce has the maximum capacity of 5 kN with 0.01% accuracy. Data logging software supplied by the torque transduce manufacturer was used to log the data (i.e., speed and torque). Each measurement was taken three times for each configuration and wind speed tested and the average values were presented in this study.
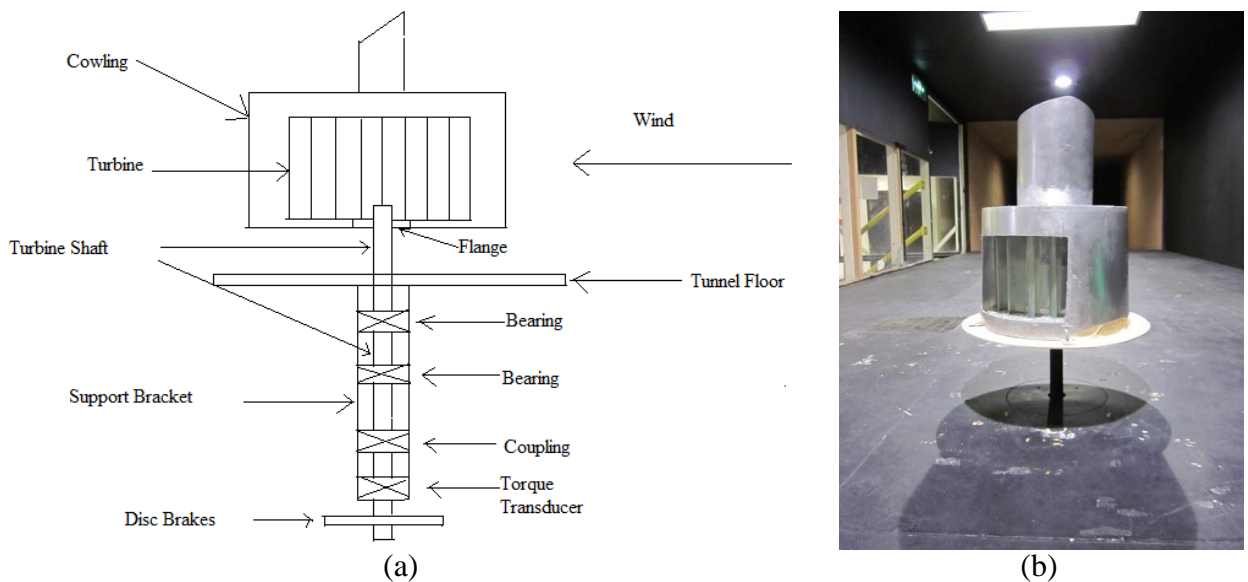

Fig. 3. experimental setup: (a) schematic; (b) inside the wind tunnel (front view).

Torques and rotor speeds for all four configurations were measured over a range of wind speeds from 20 to 45 km/h under wind tunnel environment. The minimum wind speed was constrained by the ability of the turbine to overcome bearing friction and inertia. The upper limit of wind speed was limited by safety consideration due to structural resonant vibrations. Maximum torque at each speed tested was analyzed to calculate the maximum power using the following formula:

$$P = T\omega \tag{1}$$

3. Results

Fig. 4 shows the variation of torque with rotor speeds at 20, 30 and 40 km/h wind speeds for the 16-blade rotor without a cowling. It can be observed that the torque value increases with the increase of wind speed. Fig. 5(a) shows the variation of maximum rotor speeds with wind speeds for each configuration tested. Linear relationships can be found with the rotor speed and the wind speed for all 4 configurations. Fig. 5(b) represents the maximum power curves for 4 configurations of turbine tested. It is found that 16-blade rotor with a cowling is more efficient (generates more power) than the other configurations at wind speeds above 40 km/h.
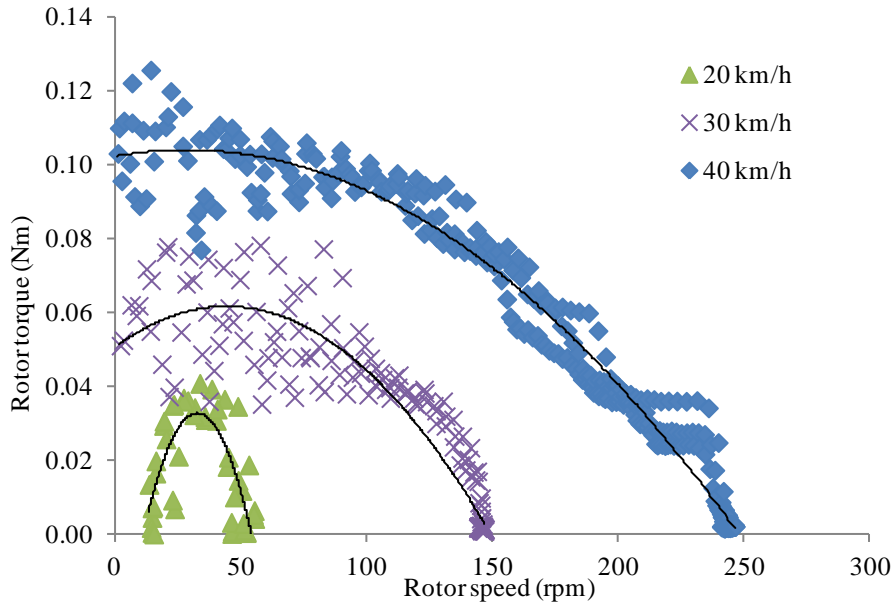

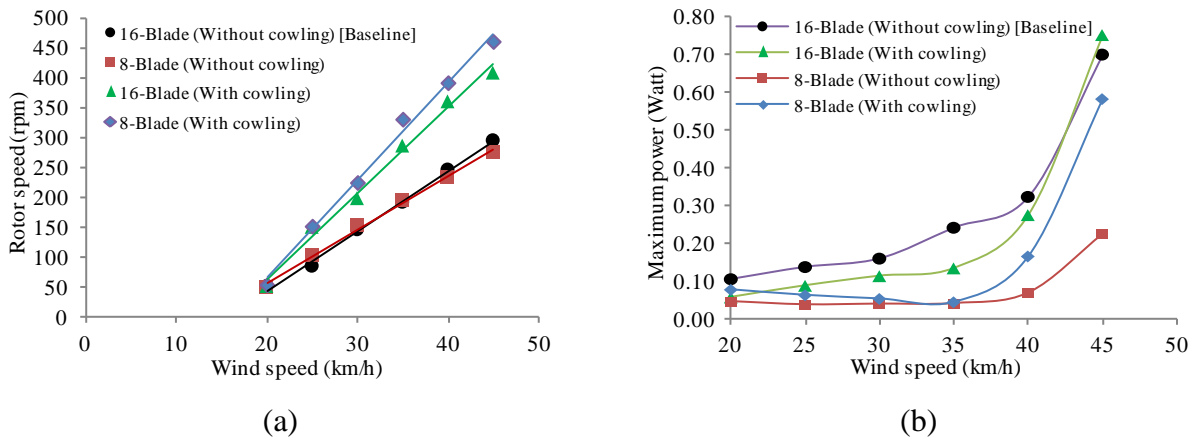Fig. 4. rotor speed as a function of torque for the 16-blade rotor without a cowling.

(a)

(b)

Fig. 5. (a) maximum rotor speed vs. wind speeds; (b) maximum power as a function of wind speeds for 4 configurations.

4. Discussion

Results indicated an increase of rotor speed with the increase wind speed for the baseline configuration: 16-blade rotor without a cowling device. The data from this study for this baseline configuration compares well with the investigation by Alam et al. [11]. The results also show the similar trend for the other three configurations. However, the rate of change of rotor rpm over the wind speeds is different for each configuration. With the use of the cowling device, the average rotor speed increased by about 26% for the 16-bladed rotor compared to the baseline configuration. A significant increase (about 40%) of rotor speed was found for the 8-bladed rotor with the cowling device. However, a 12% decrease in speed was found while the number of blades was reduced to a half without a cowling device. Hence, it is clear from the experimental data that the cowling device has positive effect to increase the rotor speed to a significant amount.

The effectiveness of a domestic scale vertical axis wind turbine mainly depends on its power generation capability. Therefore, it is important to analyze the power output over a range of wind speeds. The result shows that the baseline configuration indicated better power output capability than other three configurations up to 45 km/h wind speed. However, the use of cowling with the 16-blade rotor shows an increase of power output of about 7% at 45 km/h. similarly, the cowling device has increased the maximum power output significantly while used with 8-bladed rotor. The result shows about 159% increase of power with the 8-bladed rotor with the cowling device compared to the 8-bladed rotor with the cowling at 45 km/h. Therefore, it is clear that the cowling device can be used to increase the power out of this domestic scale vertical axis wind turbine especially with a reduce number of blades.

5. Conclusions

The results show that the cowling device has positive effect to increase the rotor speed to a significant amount. With the use of the cowling device, the average rotor speed increased by about 26% for the 16-bladed rotor compared to the baseline configuration. A significant increase (about 40%) of rotor speed was also found for the 8-bladed rotor with the cowling device. The results also indicated that the cowling device can be used to increase the power output of this cyclonic type vertical axis wind turbine especially with a reduce number of blades.

References

[1] A.C. Hansen, C.P. Butterfield, Aerodynamics of Horizontal Axis Wind Turbines, Annual Review of Fluid Mechanics. 25 (1993) 115-149.

[2] H. Hirahara, M. Z. Hossain, M. Kawahashi, Y. Nonomura, Testing basic performance of a very small wind turbine designed for multi-purposes, Renewable Energy. 30 (2005) 1279-1297.

[3] R. Howell, N. Qin, J. Edwards, N. Durrani, Wind tunnel and numerical study of a small vertical axis wind turbine, Renewable Energy. 35 (2010) 412-422.

[4] A. D. Sahin, Progress and recent trends in wind energy, Progress in Energy and Combustion Science. 30 (2004) 501-543.

[5] http://www.climatechange.gov.au/government/initiatives/renewable-target.aspx, accessed on 31 August 2013.

[6] A. Ali, F. Alam, V. Djamovski, S. Watkins, A review of power generation from wind in Australia, In Proceedings of the 9th International Conference of Mechanical Engineering. (ICME2011) (2011, December) (pp. 18-20).

[7] Victoria Consumer Guide to Small Wind Turbine Generation, Sustainable Victoria. July 2010, 1-59.

[8] T. Ogawa, H. Yoshida, Y. Yokota, Development of rotational speed control systems for a Savonius-type wind turbine, Journal of fluids engineering. 111(1) (1989) 53-58.

[8] K. Pope, I. Dincer, G. F. Naterer, Energy and exergy efficiency comparison of horizontal and vertical axis wind turbines, Renewable energy. 35(9) (2010) 2102-2113.

[9] K. Irabu, J. N. Roy, Characteristics of wind power on Savonius rotor using a guide-box tunnel, Experimental thermal and fluid science. 32(2) (2007) 580-586.

[10] B.D.Altan, M. Atılgan, A. Özdamar, An experimental study on improvement of a Savonius rotor performance with curtaining, Experimental and fluid science. 32(8) (2008) 1673-1678.

[11] F. Alam, S. Golde, An Aerodynamic Study of a Micro Scale Vertical Axis Wind Turbine, Procedia Engineering. 56 (2013) 568-572.

6th BSME International Conference on Thermal Engineering (ICTE 2014)

Adjacent wake effect of a vertical axis wind turbine

Israt Mustary, Harun Chowdhury*, Bavin Loganathan and Firoz Alam

School of Aerospace, Mechanical and Manufacturing Engineering, RMIT University, Melbourne, 3083, Australia

Abstract

The main objective of this study is to understand the effect of turbine placement and surrounding structures. Using Urban Green Energy's UGE-4K vertical axis wind turbine and the ANSYS computational fluid dynamics package (CFX), a dynamic fluid analysis was undertaken looking at the wake of the turbine through a variety of different inlet speeds and rotational frequencies to determine suitable flow recovery for optimal placement of subsequent turbines. The results showed that the wake interference is minimal at around 5 times the diameter of the turbine downstream. Results also show that flow recovery was a lot slower to the right of the turbine especially along a line 15° from the centre of the turbine to the right as this is coincident with the vortices generated from the turbines rotation.

Keywords: wake effect; vertical axis wind turbine; optimal turbine placement; CFD modelling.

1. Introduction

Harnessing the wind for power has been achieved by humans for over 5000 years with the Egyptians using sails to travel the Nile. The first windmills were discovered around the Persian-Afghan borders date back to 200 BC and the Dutch followed with their windmills for irrigation and drainage around 1300-1875 AD [1]. When the electrical generator was invented the application was soon used with the wind turbine and the first large wind turbine to

* Corresponding author. Tel.: +61 3 99256103; fax: +61 3 99256108.
  E-mail address: harun.chowdhury@rmit.edu.au

generate electricity was created in 1888 and was rated at 12 kW [2]. The progression continued with technology levels increasing and more research being undertaken it wasn't long till large scale wind farming was taking place with a notable case of California where over 16,000 machines ranging from 20-350 kW were installed between 1981 and 1990 for a total of 1.7 GW [3]. In recent years the global wind industry has been the fastest growing industry in electrical power generation with over 237,000 MW worth of capacity installed by the end of 2011.

The vertical axis wind turbine (VAWT) has been around for years but is starting to get more and more widely used as the world constantly increases its focus on renewable energy sources. The VAWT has the capability of providing a renewable energy source to the domestic, private and small commercial markets as it can be placed on rooftops and areas of turbulent flows with more success than a horizontal axis wind turbine (HAWT) [4-6]. The wind turbine power generation efficiency in commercial and domestic applications can significantly be affected by the built up geometry and the interference of adjacent turbines [7]. In order to maximize the power output, it is important to understand aerodynamic behavior of different building edges, surrounding structures and nearby installed turbine wakes. The wake of a turbine is an important part of analysis because it gives an assessment of the performance of the wind turbine, the other benefit of wake analysis is that an understanding of the downstream effect of the flow can be garnered and used for the optimizations of the placement of subsequent wind turbines for maximum effectiveness. Despite the importance, little information is available on optimal placement of turbines and their wake effect. Hence, the main objective of this study is to understand the effect of turbine placement and surrounding structures. Numerical and computational fluid dynamics (CFD) models were used to analyze wake and turbulence in the analysis of a commercially manufactured VAWT.

2. Methodology

2.1. Selection of wind turbine

Urban Green Energy (UGE) is a world leader in small wind and renewable energy systems, with installations across the globe. UGE designs, manufactures, and markets cutting-edge vertical axis wind turbines and hybrid renewable solutions with a track record of high performance, safety, and reliability. Fig. 1(a) shows the UGE-4K turbine marketed towards large domestic or moderate commercial scale. The turbine is designed to provide the maximum power possible from the wind over a given area. Detailed specifications of this wind turbine can be found in [8]. A simplified 3D CAD model of the UGE-4K turbine was developed for this study as shown in Fig. 1(b). The simplified CAD model of the turbine was used as the downstream wake profile is dependent on the whole physical geometry and rotational speed of the turbine rather than aerofoil type blade profile.
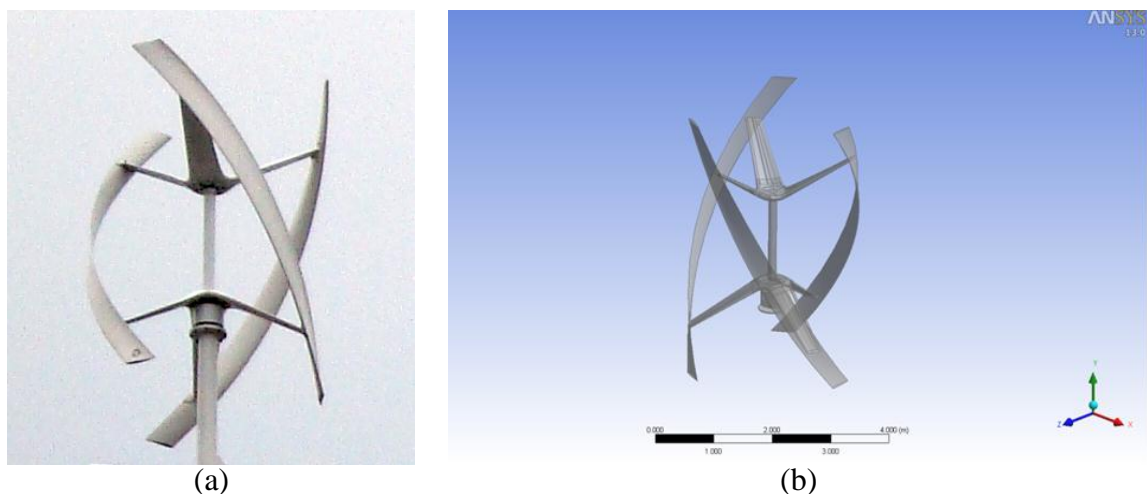

(a)   (b)

Fig. 1. (a) UGE-4K turbine; (b) CAD model in ANSYS.

2.2. Analysis parameters

In order to get a good understanding of the wake effects, the turbine was analysed across a range of expected wind speed and at a range of associated rotor speed. From the UGE-4K data sheet obtained from UGE, the cut-in speed was found 3.5 m/s and its optimal running speed was 125 rpm at 12 m/s wind speed. Therefore, a good range for analysis would be 2−12 m/s to look at the flow around a turbine before cut-in to investigate the flow behavior of subsequent turbine for cut-in, and not above 12 m/s because there is a decrease in efficiency above the optimal speed and the expected local wind speeds in the built-up environment would rarely be above a clean 12 m/s flow.

2.3. CFD setup

The CFD package utilized was ANSYS CFX for its ability to model and analyse rotating turbines with the help of its TURBO model setup. The turbine was boolened out of a cylinder with 0.25 m clearance on all sides of the blades. This cylinder was then fitted inside the fluid domain with all edges matching up with a negative space of the same dimensions so that there would be no issues with surface interfaces. The cylinder acts as the rotating domain immersed in the fluid domain. The model was analyzed in full-scale of the UGE-4K; thus the rotating domain has 3.5 m diameter and 4.9 m height. The fluid domain dimensions are 66 m × 45 m × 30 m. The model was meshed with more importance placed on the fluid domain as it is the point of analysis rather than near boundary layer of the blades of the turbine. Thus the quality of the mesh is aimed at giving reasonable results within the fluid domain. A tetrahedral mesh was used with refinement on curvature and proximity to geometry. Mesh statistics indicated an average skewness of 0.232 which is an acceptable value for the purposes of this analysis as it is expected to yield reasonably accurate results. Fig. 2(a) shows the position of the rotational domain inside of fluid domain whereas mesh of the fluid and rotational domain are shown in Fig. 2(b) and Fig. 2(c) respectively.
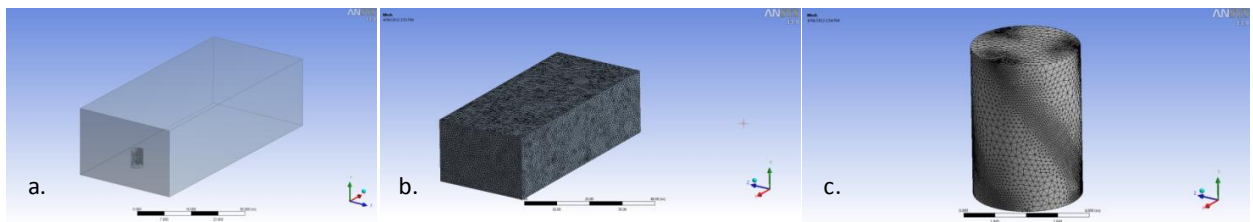

Fig. 2. (a) rotational domain modelled inside of fluid domain; (b) fluid domain mesh; (c) rotational domain mesh.

The fluid used in this analysis is standard air at ground level, i.e. at *25 °C* with a density of $\rho = 1.185 \ kg/m^3$ and a dynamic viscosity of $\mu = 1.831 \times 10^{-5} \ kg/m \ s$. As the turbine was analyzed at a range of speeds the inlet fluid velocity from 2−12 m/s. The ground was treated as a wall with no slip conditions. The sides and sky are defined as openings with a zero relative pressure and zero relative temperature difference to that of the fluid body. The outlet is treated as an outlet with an average static pressure of zero. The rotating domain was set as a rotating body with input revolutions across 24−125 rpm with respect to the inlet speeds and was rotating clockwise as the turbine is designed to do. The blades and body of the turbine are considered as rotating non-slip walls. There are interfaces defined between the matching faces of the rotating domain and the fluid domain. The interfaces are placed as rotor-stator with a pitch change of zero as the whole model is present and rotating 360 degrees. The *k-ε* turbulence model was used for the analysis. The solver control was set so that it runs across the physical timescale under which the turbine completes one full rotation. The residual type was defined as RMS rather than Max Residual which leads to lose convergence, the iterations to convergence was defined as 100 and the convergence criteria was 10^{-4}.

3. Results and discussion

Usually two turbulent models: *k-ε* and *k-ω* are widely used for the analysis of CFD simulation [9]. The most appropriate turbulence model for this analysis was determined through running two simulations using the both turbulent models on a sphere under similar conditions by matching the inlet wind speed with respect to the equivalent Reynolds number of the VAWT simulation. Table 1 shows the results from the simulations. Using the resulting calculated C_D on the sphere for both turbulence models and comparing them with the graph of C_D vs. *Re* on a sphere to determine which was closer to the expected for the relative turbulent region under which the model would be evaluated. With the expected drag on a smooth sphere around the region with a Reynolds number of 1.96×10^6, is around 1.5-2.0 [10]. It can be seen in Table 1 that the *k-ε* model yields a closer C_D value for this turbulence region with 0.14729 and thus this model is more suitable for the wind turbine analysis in this turbulence region.

Table 1. Results of CFD simulations using k-*ε* and k-*ω* models on a sphere.

Parameters	*k-ε*	*k-ω*
Frontal area of sphere (m^2)	0.3927	0.3927
Drag force on sphere (N)	30.843	21.996
Coefficient of drag of sphere (C_D)	0.14729	0.1050

For the wake analysis the results of the range of inlet wind speeds and relative rotor speeds were correlated and compared to each other to determine a value of recovery across the different conditions along different paths within the fluid domain. Velocity and pressure contours, velocity vectors and streams are evaluated for the 2-10 m/s inlet speeds at 24-120 rpm, these contours are based on a plane intersecting the turbine and consequently fluid domain in the centre, thus these results are about the mid-plane. It was observed that there is no real difference between the different inlet speeds and wake patterns bat a scale effect, this is because they are in the same turbulence region as the Reynolds number doesn't vary so much between an inlet speed of 2 m/s to that of 12 m/s.

Fig. 3 shows the velocity contour about the vertical mid-plane and the horizontal mid-plane at 10 m/s inlet wind speed and 120 rpm rotor speed. It can be seen that there is an increased velocity coming off of the top and bottom of the turbine as a result of the flow over the vortexes created by its rotation and low pressure region. There is also an increased total velocity coming off the centre back of the turbine which gradually slows down and returns to around the inlet velocity. The slow regions of velocity are most critical around the front of the turbine and coming off the top and bottom created by the blades creating a low and high pressure region through extracting energy from the wind.
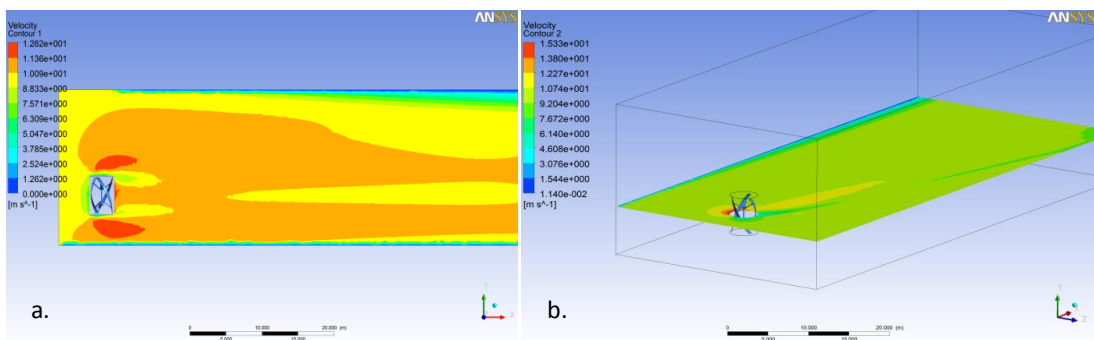

Fig. 3. velocity contours: (a) about the vertical mid-plane; (b) about the horizontal mid-plane.

Fig. 4 shows the pressure contour about the vertical mid-plane and the horizontal mid-plane at 10 m/s inlet wind speed and 120 rpm rotor speed. The figure shows that maximum pressure occurs in the centre immediately in front of the turbine with low pressure regions above and below the blades with a maximum point towards the back of the turbine. The low pressure regions slowly recover pressure back to zero relative pressure to the inlet downstream with

the centre of the turbine having the quickest recovery as it is out of the way of the critical low pressure regions at the top and bottom of the turbine. These low pressure regions would also be a critical component of the increased flow over the top and bottom of the turbine in terms of wind speed.

The velocity vector plot is shown in Fig. 5 where only the free stream velocity vector which is aligned with the inlet flow and it gives a more accurate representation of flow recovery because the flow running parallel to the inlet flow is the most desirable flow for the turbine to extract energy form the wind. The plot shows decreased flow immediately around the turbine which gradually recovers downstream and is around 3.5 m/s, increased flow above and below the slow flow of the turbine, at a maximum of around 12.5 m/s, which fans out and slows down back to inlet speed gradually.
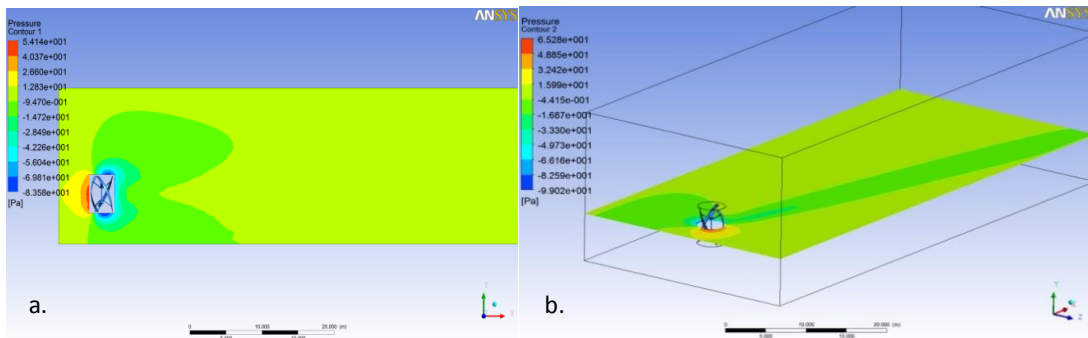

Fig. 4. pressure contours: (a) about the vertical mid-plane; (b) about the horizontal mid-plane.
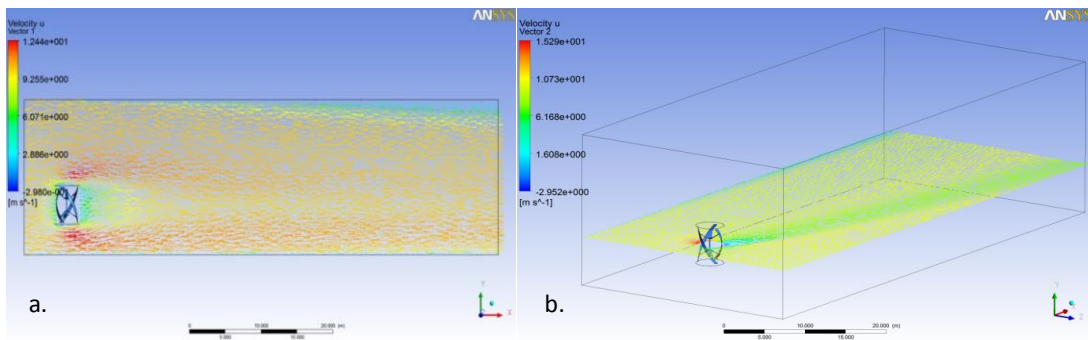

Fig. 5. velocity vector: (a) about the vertical mid-plane; (b) about the horizontal mid-plane.

The streamline plot shows the vortices coming off the right hand side of the turbine at the top and bottom and continuing to swirl all the way downstream at an angle of roughly 15° to the centre of the turbine (see Fig. 6). These vortices would indicate that there would be more turbulent flows on the right of the turbine and thus slower recover on that side. The side on which the vortices are coming off is determined by the direction of rotation of the turbine. If the turbine was rotating counter-clockwise the vortices would be on the left and the reduced flow recovery, in the directional vector, would be slower on the left.

Fig. 7 shows the velocity vector directly downstream from the centre of the turbine for the various inlet speeds and rotor speeds. The results show that better the flow recovery is possible at further downstream. The graph shows that recovery takes a slightly longer distance as the inlet speed increase but for all inlet speeds it can be seen that at around 15 m downstream, and to non-dimensionalise it, divide it by the turbine diameter (3 m) which equates to 5 times the diameter of the turbine downstream, there is almost complete flow recovery. The graph also shows that the flow recovery directly downstream appears to be asymptotic to the relative inlet speed.
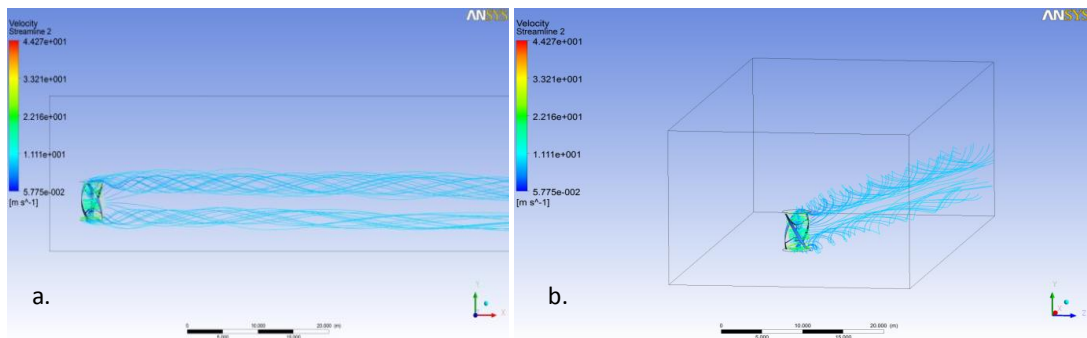
Fig. 6. velocity streamline: (a) about the vertical mid-plane; (b) about the horizontal mid-plane.
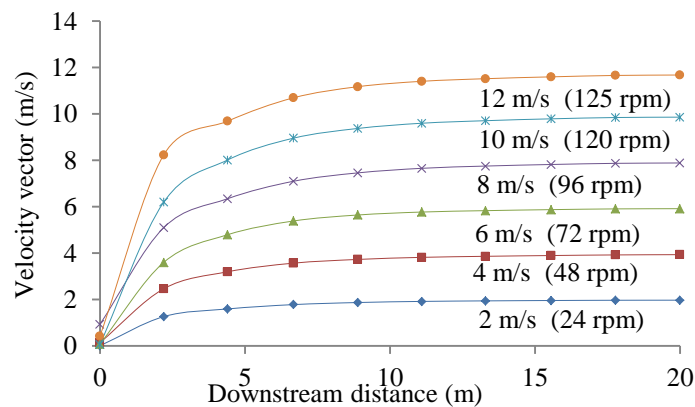

Fig. 7. directly downstream velocity vector as a function of downstream distance for all speeds tested.

4. Conclusions

From the wake analysis over a range of expected wind and rotor speeds it was shown that directly downstream of a turbine adequate flow recovery was seen 5 times the diameter of the turbine downstream. It was also seen that flow recovery was a lot slower to the right of the turbine especially along a line 15° from the centre of the turbine to the right as this is coincident with the vortices generated from the turbines rotation. The converse of this was found in that flow recovery to the left of the turbine was a lot quicker than the right side and central line and that at −15°.

References

[1] J. Kaldellis, D. Zafirakis, The wind energy revolution: A short review of a long history, Renewable Energy. 36 (2011), 1887-1901.
[2] J. Herbert, S. Iniyan, E. Sreevalsn, S. Rajapandian, A review of wind energy technologies, Renewable and Sustainable Energy Reviews. 11 (2007), 1117-1145.
[3] V.Quaschning, Understanding Renewable Energy Systems, Earthscan, United States, 2005.
[4] P. Lynn, Onshore and Offshore Wind Energy: An Introduction, John Wiley & Sons, Queensland, 2012.
[5] J. Roberts, Micro Wind Energy Systems in Harsh Environments, Memorial University, Newfoundland, 2009.
[6] S. Eriksson, H. Bernhoff, M. Leijon, Evaluation of Different Turbine Concepts for Wind Power, Renewable and Sustainable Energy Reviews.12 (2008), 1419-1434.
[7] J. Yao, J. Wang, W. Yuan, H. Wang, L. Cao, Analysis on the influence of Turbulence model changes to aerodynamic performance of vertical axis wind turbine, International Conference on Advances in Computational Modeling and Simulation. 31 (2012), 274-281.
[8] Urban Green Energy, UGE-4K Specification Sheet [accessed on 11 Nov 2012 from http://www.urbangreenenergy.com/products/uge-4k/downloads]
[9] J. Tu, G.H. Yeoh, C. Liu, Computational Fluid Dynamics: A Practical Approach, Elsevier, Oxford, UK, 2008.
[10] NASA, Drag on a sphere. [accessed on 25 May 2013 from https://www.grc.nasa.gov/WWW/k-12/airplane/Images/dragsphere.jpg]

6th BSME International Conference on Thermal Engineering (ICTE 2014)

Energy Yield of Torrefied Rice Husk at Atmospheric Condition

Md. Ahiduzzaman[a*] and A.K.M. Sadrul Islam[b] *

[a]*Bangabandhu Sheikh Mujibur Rahman Agricultural University, Gazipur-1706, Bangladesh*
[b]*Islamic University of Technology, Board Bazar, Gazipur-1704, Bangladesh*

Abstract

Torrefaction is a thermal treatment for lignocellulosic waste biomass at low temperature, which has been found to be effective not only for improving the quality of biomass solid fuels, in terms of higher energy density, longer shelf life and hydrophobic in nature, but also to make them useful as a feedstock for further decomposition such as gasification and liquefaction. In this study, torrefaction of rice husk is carried out in a fixed bed reactor under atmospheric condition at a temperature range of 200 to 300°C, in order to clarify the effect of air on torrefaction of rice husk. © 2015 The Authors. Published by Elsevier Ltd.
Peer-review under responsibility of organizing committee of the 6th BSMEInternational Conference on Thermal Engineering (ICTE 2014).

Keywords: Torrefaction, Rice husk, Mass yield, Calorific value ratio, Energy yield.

1. Introduction

Biomass is considered one of the most abundant resources on earth and can be used as feed stock of fuel in its' solid, liquid or gaseous form and chemicals. Lignocellulosic waste biomass is drawing attention worldwide because of its non-edible characteristics. Rice husk is considered to be the best source of biomass energy obtained as milling waste of rice processing centers [1]. In 2009, Bangladesh produced about 9.0 million tonnes of rice husk and it is the fourth largest producer of the total world supply of rice husk [2, 3]. Torrefaction is thermal treatment of biomass at 200 to 300° C temperatures under an inert atmosphere is found to be effective for enhancing the energy density and shelf life of the biomass and has been reported for wood and grass biomass over the past few years [4-10]. Torrefaction can be used to increase the energy content of wood or to facilitate grinding. Couhert et al. confirmed that torrefaction decreased the oxygen carbon ratio [4]. Arias et al. studied torrefied woody biomass (eucalyptus) in

---

order to improve its properties for pulverized systems consisting in a heating treatment at moderate temperature (240, 260, 280 °C) under an inert atmosphere [5]. Torrefaction improves the properties of biomass in relation to energy conversion techniques; e.g., combustion, co-combustion with coal or gasification**.** Bridgeman et al. showed that both volatile and char combustion of the torrefed biomass become more exothermic compared to the raw fuels, and that depending on the degree of the torrefaction. They also reported that torrefed fuel can contain up to 96% of the original energy content on a mass basis and ignites more quickly [6]. After torrefaction the wood briquettes showed an increase of approximately 15 % in heating value, and a decrease of approximately 73 % in equilibrium moisture. Torrefed briquettes show hydrophobic nature during storage [7]. The increase of the heating value of the torrefed rice straw and rape stalk compared with the raw material are 17% and 15%, respectively [8]. Study results from torrefaction processes of four kinds of biomass materials, including bamboo, willow, coconut shell and wood (Ficus Benjamina L.) show that the biomass torrefed in less than 1 h with light torrefaction (240°C) is an appropriate operation for producing fuels with higher energy density [9]. Torrefaction or thermal pretreatment of biomass can produce an energy dense and consistent quality solid biomass fuel for combustion and co-firing applications. The results of torrefed pine chips and logging residues showed the improved fuel characteristics and grinding properties closer to coal [10]. There are several research reports on torrefaction of biomass from forest product and some residues however; little information is found on torrefaction of rice husk [28]. Torrefaction process requires heat energy. Then the process could not be energy efficient. Rice husk is produced in rice milling centers of Bangladesh. Rice milling center has a rice husk fired boiler unit [11]. A huge waste heat is liberated from the boiler with temperature ranges of 600 to 700°C. This waste heat can be used to meet up the requirement of heat energy for torrefaction. Most of the torrefaction process is reported under inert (nitrogen) atmosphere. When the waste thermal energy is used for torrefaction, the gas contains some components other than nitrogen such as oxygen, carbon dioxide and water vapor. The oxygen content is thought the worst problem for torrefaction, because there is a possibility of higher oxidation during the process. However, Uemura et al reproted that torrefaction can be done without any significant problem in environment with oxygen content in the range of 3 to 15% [24, 25]. The oxygen content in flue gas from boilers used in rice mill is reported in the range of 7-8% [27]. Hence torrefaction under static air would be cost effective and affordable for local condition of rice millers in Bangladesh. A comparison study of torrefaction of different varieties of rice husk is reported in Ahiduzzaman [26]. In this paper, torrefaction of rice husk is carried out in a fixed bed reactor in the presence of static air to answer the question above.

2. Methodology

2.1 Torrefaction

Torrefaction of the rice husk samples is carried out using a crucible as reactor made of ceramic. Four gram of each sample was weighed, and put in a ceramic crucible. The crucible is placed in a muffle furnace with digital PID controller (jSR Model: JSMF-45T). Time and temperature for torrefaction of each sample is maintained with setting program with PID control of muffle furnace. The temperature of the reactor was raised to desired levels, *i.e.* 200, 250 or 300°C by switching on the furnace. Samples are heated at three different duration of heating for torrefaction, i.e. 10, 20 and 30 min. After finishing the torrefaction, the sample is then removed from furnace and left to cool down at an ambient temperature. The torrefed sample of husk is then weighed and kept in desicator till the characterization. Three replication of each sample were analyzed and an average value was taken.

2.2 Measurements

The moisture content, proximate contents (volatile matter, fixed carbon and ash), mass and the calorific value were measured before and after torrefaction. Volatile matter is determined as per British Standard BS EN 1860 [12]. Fixed carbon and ash content of the samples are determined the methods described in Tariq et al. and Rees et al. [13, 17]. The calorific value of rice husk samples are measured using a bomb calorimeter, model CH80b MAHLER CALORIMETER manufactured by ISI IMPIANTO, ITALIA. Detail description of the method is reported in Ahiduzzaman [26]. From the experimental results, mass yield, calorific value ratio and energy yield are calculated by the following equations:

$$Mass\ yield = \frac{Mass\ of\ solid\ sample\ after\ torrefaction}{Initial\ mass\ of\ sample} \times 100\% \ ---[1]$$

$$Calorific\ value\ ratio = \frac{Calorific\ value\ of\ solid\ sample\ after\ torrefaction}{Calorific\ value\ of\ rice\ husk\ sample\ used} \ ----[2]$$

$$Energy\ yield = Mass\ yield \times Calorific\ value\ ratio \ ------[3]$$

3. Results and Discussions

3.1 Proximate analysis of raw husk

The results show that volatile matter, fixed carbon and ash content of husk are 62.84%, 15.09% and 22.07%, respectively. Iyer et al. also reported that the volatile matter of rice husk from different location varied from 65% to 67% while the fixed carbon and ash content varied from 11.2% to 18% and from 13.1% to 22.4% respectively [14]. Kargbo et al. reported that the volatile matter of rice husk is 63.52% [15]. These results are very close to the results of this study although the physical properties of biomass frequently depend on the soil and geographical location of biomass produced. In this study BRRIdhan50 variety of husk is taken for detail analysis of torrefied husk to identify the optimum combination of torrefaction factor in the next section.

3.2 Effect of torrefaction on proximate contents of rice husk

Proximate analysis results of torrefied husk samples at 200, 250 and 300°C for 10, 20 and 30 minutes of heating are shown in Fig. 1, Fig. 2 and Fig. 3. Volatile matter content decreases in torrefied samples with increase of both temperature and residence time. Whereas, fixed carbon and ash content increase due to the increasing temperature and duration of heating. Highest volatile matter was found to be 61% at 200°C for 10 min of heating and lowest volatiles matter was found to be 24.68% at 300°C for 30 min heating. Fixed carbon and ash content increased to 32.58% and 42.74% at 300°C for 30 min from their original value of 15.09% and 22.07%, respectively. Sridhar et al. reported that volatile matter decreased and fixed carbon increased with increase in temperature of torrefaction for bamboo [16]. Almeida et al. also reported that an increase in fixed carbon and a decrease in volatile matter with increased temperature and duration of torrefaction reaction occurred for different wood and bark biomass [19].
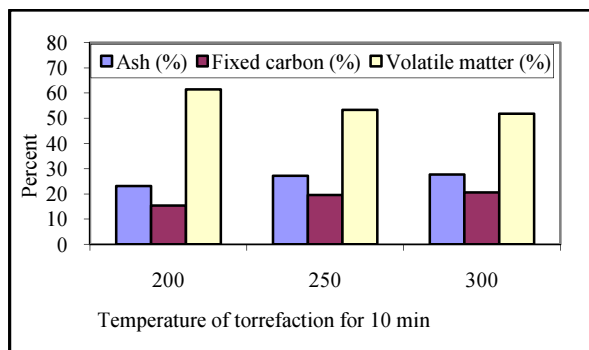

Fig.1. Proximate analysis of torrefied rice husk after 10 minute of residence time
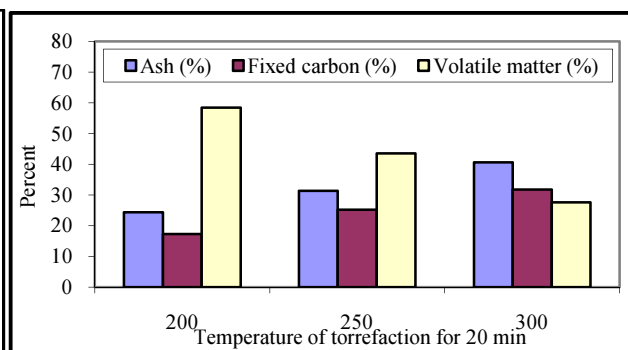
Fig.2. Proximate analysis of torrefied rice husk after 20 minute of residence time

3.3 Effect of torrefaction on mass yield of rice husk

Mass yield of torrefied samples were measured in percent of original mass of sample and presented in Fig. 4. Highest mass yield was 90% at 200°C and 10 min of torrefaction and lowest mass yield was 50% at 300°C and 30

min of torrefaction. This is a genral norm that the rate of mass loss depends on the parameters of torrefaction. In this study it is found that mass loss increases with increase in temperature and reaction time. Similar results for mass loss of torrefied biomass also is reported in previous studies [18, 19].
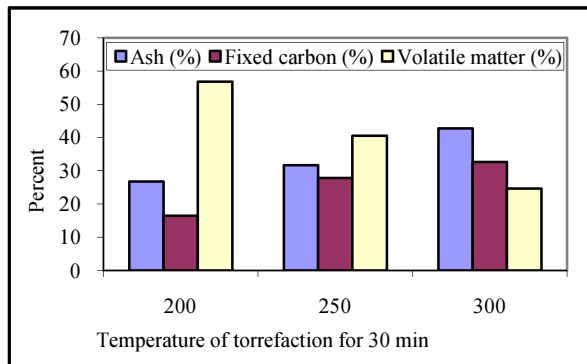

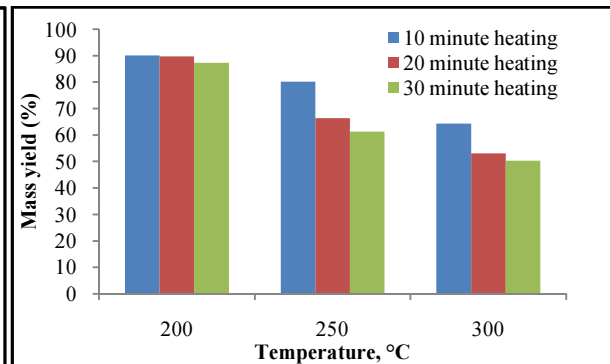Fig.3. Proximate analysis of torrefied rice husk after 30 minute of residence time

Fig.4. Mass yield of torrefied rice husk at dirrerent temperature and residence time

3.4 Effect of torrefaction on calorific value

   Calorific value of each sample of torrefied rice husk was measured and presented in Fig. 5. There is an interaction effect of temperature and residence time on calorific value of torrefied husk. Calorific value increases remarkly with increasing of heating temperature for a reaction time of 10 min and decreases for a reaction duration of 30 min. Calorific value increases minorly with increasing of temperature of heating under the condition of 20 min of reaction duration. It is reported that calorific value of torrefied wood increases with increase in temperature and duration of reaction [19, 20, 21]. However, for rice husk the calorific value decreased at higher heating time. This phenomenon ouccred might be due to the increase of mass fraction of ash in torrefied husk. McKendry also reported that the energy of the fuel is reduced in proportion to the magnitude of the ash content [22]. Calorific value ratio of raw husk and torrefied husk are presented in Fig. 6. The highest carific value ratio was found to be 1.33 under the condition of 300°C and 10 min duration of heating. The lowest calorific value ratio was found to be 1.08 under the condition of 300°C and 30 min duration of heating. The results confirmed that for obtaining higher energy density, higher heating temperature and lower heating duration is the optimum condition.
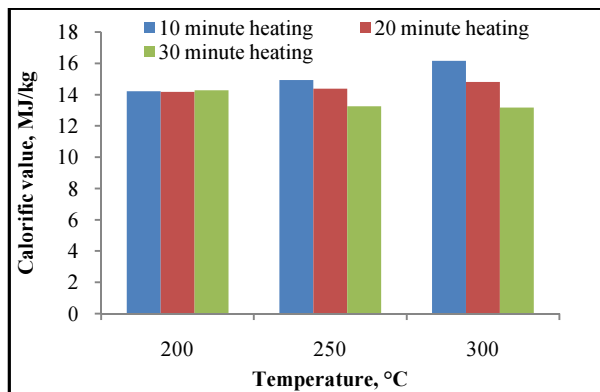

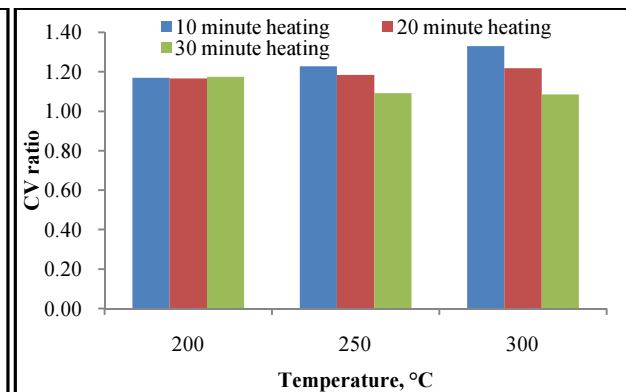Fig.5. Calorific value of torrefied rice husk at dirrerent temperature and residence time

Fig.6. Calorific value ratio of torrefied husk and raw husk at dirrerent temperature and residence time

3.5   Effect of torrefaction on moisture content of rice husk

During the torrefaction process signifcant amount of moisture is removed. The lowest moisture content was found at 300°C for 30 minutes of heating duration [Table 1]. The results show that the rice husk achieves hydrophobic nature after torrefaction. Thus enhances the maximum energy recovery during the combustion of torrefied biomass.

Table 1. Changes in moisture cotnent of torrefied husk at diifferent time and temperature conditions

Temperature	Moisture content (%) of torrefied product at different condition		
	10 min	20 min	30 min
200°C	2.81	2.31	2.04
250°C	2.28	1.75	1.47
300°C	2.08	1.74	1.46
Control (raw husk)	9.07		

3.6 Effect of torrefaction on energy yield of rice husk

   Energy yield indicates the improvement of calorific value of rice husk by torrefaction and it is the key parameter for defining the fuel quality. Fig. 7 shows the relationship between energy yield and temperature at different residence time for 10, 20 and 30 minutres. The energy yield was found in the range of 55% to 105% for torrefied husk. The results shows that energy yield decreases with increase in temperature and residence time. The highest energy yield was found at 200°C of heating temperature. Energy yield was found to be 105.3%, 104.5% and 102.5% for 10, 20 and 30 min of residence time, respectively at 200°C. The energy yield at 250°C for reaction period of 10 min was found to be 98%. The energy yeild value over 100% means the moisture and some non-energy volatile are significantly removed during torrefaction process. From the results it is recommended that the optimum torrefaction of rice husk should be at a temperature range of 200-300°C for a reaction period of 10-30 minutes. Similar results are reported for other types of biomass such as torrefied wood briquette shows 97% of energy yield for 30 minute of heating duration at 220°C (18) and energy yield of willow is 94.9% at 280°C for 17.5 min reaction time [23]. Uemura et al reproted that torrefaction can be done without any significant problem in environment with oxygen content in the range of 3 to 15% [24, 25].
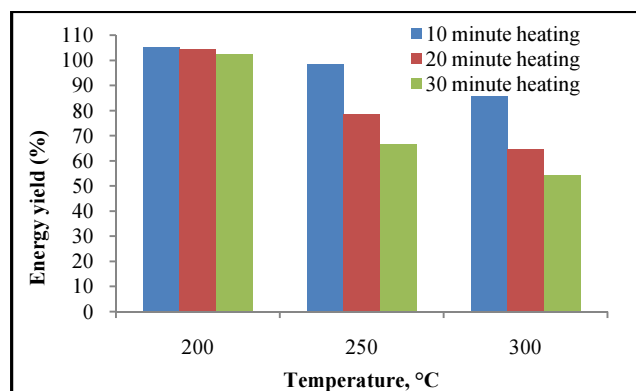
Fig. 7: Energy yield of torrefed rice husk at dirrerent temperature and residence time.

4. Conclusion

   Torrefaction of rice husk was carried out in the presence of air in order to investigate the effects of various torrefaction conditions, viz., different temperature level (200 250 and 300°C), different duration of heating (10, 20 and 30 min), on the change in moisture content, mass recovery, calorific value and energy yields. The mass yield decreased noticeably with an increase in temperature and residence time. The results confirm that torrefaction

reaction rate is affected by both the temperature and residence time. The calorific value and calorific value ratio show a complex behavior. Caloric value increases considerably with increase in temperature for 10 min of residence time. On the other hand these values decrease with increase in temperature for 30 min of residence time. The energy yield decreases with an increase in temperature and residence time, but all the values fell between 105 and 103% at 200°C for 10 min residence time. It is worthwhile pointing out that torrefaction in the presence of static air can be carried out without any significant problem. Since the temperature of flue gas from rice parboiling boiler contains lower oxygen (7-8% oxygen) compared to air, then the flue gas is more suitable for torrefaction media when it is directly in the reactor.

References

[1] Ahiduzzaman, M., Sadrul Islam, A. K.M. , "Energy Utilization and Environmental Aspects of Rice Processing Industries in Bangladesh." Energies, 2, no. 1: 134-149, 2009.

[2] http://www.irri.org/science/ricestat/pdfs/WRS2005-Table01.pdf, (accessed on 03.02.2006)

[3] http://faostat.fao.org/site/339/default.aspx (accessed on 17.02.11).

[4] C. Couhert, S. Salvador, J-M. Commandré, Impact of torrefaction on syngas production from wood, Fuel, 88, pp. 2286-2290, 2009.

[5] B. Arias, C. Pevida, J. Fermoso, M.G. Plaza, F. Rubiera, J.J. Pis, Influence of torrefaction on the grindability and reactivity of woody biomass, Fuel Processing Technology, 89, pp. 169-175, 2008.

[6] T.G. Bridgeman, J. M. Jones, I. Shield, P.T. Williams, Torrefaction of reed canary grass, wheat straw and willow to enhance solid fuel qualities and combustion properties, Fuel, 87, pp. 844-856, 2008.

[7] Felix Fonseca Felfli, Carlos Alberto Luengo, Jose Antonio Suárez, Pedro Anibal Beatón, Wood briquette torrefaction, Energy for Sustainable Development, 9, pp. 19-22, 2005.

[8] Jian Deng, Gui-jun Wang, Jiang-hong Kuang, Yun-liang Zhang, Yong-hao Luo, Pretreatment of agricultural residues for co-gasification via torrefaction, Journal of Analytical and Applied Pyrolysis, 86, pp. 331-337, 2009.

[9] Wei-Hsin Chen, Po-Chih Kuo, A study on torrefaction of various biomass materials and its impact on lignocellulosic structure simulated by a thermogravimetry, Energy, 35, pp. 2580-2586, 2010.

[10] M. Phanphanich, S. Mani, Impact of torrefaction on the grindability and fuel characteristics of forest biomass, Bioresour Technol, 102(2):1246-53, 2011.

[11] M A Baqui, M. Ahiduzzaman, M Khalequzzaman, M M Rahman, J Ghani and S M F Islam, Development and Extension of Energy Efficient Rice parboiling Systems in Bangladesh, A Comprehensive Research Report Funded by German Technical Cooperation (GTZ), 2008.

[12] BRITISH STANDARD. Appliances, solid fuels and firelighters for barbecueing —. Part 2: Barbecue charcoal and barbecue charcoal briquettes — Requirements and test methods. BS EN 1860-2:2005

[13] Tariq, A.S., Reupke, P and Sarwar G., Biomass Combustion Systems. A Guide for Monitoring and Efficeint Operation. NRI. UK, 1994.

[14] Iyer, P.V.R., Rao, T.T, Grover, P.D. and Singh N.P. , Biomass Thermo-Chemical Characterization. Second Edition. Chemcial Engineering Department, Indian Institute of Technology, Delhi, 1997.

[15] Kargbo, F. R., Xing, J. and Zhang, Y.(2009). Pretreatment for energy use of rice straw: A review. African Journal of Agricultural Research Vol. 4, pp. 1560-1565, 2009.

[16] Sridhar, G., Subbukrishna, Sridhar, H. V., Dasappa, S., Paul, P.J. and Mukunda, H.S. Torrefaction of Bamboo, 15th European Conference and Exhibition, 7-11 May, Berlin, Germany, 2007.

[17] Rees, O.W., Coolican, F. A. and Pierron, E.D., Comparison of Methods for Determination of Volatile Matter and Ash in Coal. Division of the Illinois State Geological Survey. Circular 240, 1957.

[18] Felix Fonseca Felfli, Carlos Alberto Luengo, Jose Antonio Suárez, Pedro Anibal Beatón, Wood briquette torrefaction, Energy for Sustainable Development, 9, 2005, pp. 19-22, 2005.

[19] Almeida, G., J.O. Brito, P. Perré, Alterations in energy properties of eucalyptus wood and bark subjected to torrefaction: The potential of mass loss as a synthetic indicator, Bioresource Technology, 101, 2010, pp. 9778-9784, 2010.

[20] Mark J. Prins, Krzysztof J. Ptasinski, Frans J.J.G. Janssen, Torrefaction of wood Part 1. Weight loss kinetics, J. Anal. Appl. Pyrolysis, 77, pp. 28-34, 2006.

[21] Mark J. Prins, Krzysztof J. Ptasinski, Frans J.J.G. Janssen, Torrefaction of wood Part 2. Analysis of products, J. Anal. Appl. Pyrolysis, 77, 2006, pp. 34-40, 2006.

[22] McKendry, P., Energy production from biomass (part 1): overview of biomass. Bioresour. Technol. 83, 37–46, 2002.

[23] Bergman, P.C.A. and Kiel, J.H.A. Torrefaction for biomass upgrading. Published at 14th European Biomass Conference & Exhibition, Paris, France, 17-21 October 2005.

[24] Uemera Y., Omar, W. N., Othman, N. A., Yusup, S. and Tsutsui, T. Effect of atmosphere on torrefaction of oil palm waste. World Renewable Eenrgy Congress 2011- Sweden, 8-13 May 2011, Linkoping Sweden.

[25] Uemera Y., Omar, W., Othman, N. A., Yusup, S. and Tsutsui, T. Torrefaction of oil palm EFB in the presence of oxygen. Fuel (2011), doi:10.1016/j.fuel.2011.11.018

[26] Ahiduzzaman, M. Studies and Investigation on Extraction of Energy and Value Added Product from Rice Husk. A PhD Thesis Submitted to the Department of Mechanical and Chemical Engineering, Islamic University of Technology, September 2011, Gazipur-1701, Bangladesh.

[27] Baqui, M. A., Ahiduzzaman, M., Khalequzzaman, M., Rahman, M. M., Ghani, J. and Islam, S.M.F. Development and Extension of Energy Efficient Rice parboiling Systems in Bangladesh. A Research Report Funded by German Technical Cooperation (GTZ), 2008.

[28] Pimchuai, A.; Dutta, A. and Basu, P. (2010). Torrefaction of Agriculture Residue To Enhance Combustible Properties. Energy & Fuels. 24, 4638–4645.

6th BSME International Conference on Thermal Engineering (ICTE 2014)

On the implementation of two-diode model for photovoltaic-thermal systems

Mohammad Waliullah[a],*, M. Zakir Hossain[b], Sumon Saha[a]

[a]*Department of Mechanical Engineering, Bangladesh University of Engineering and Technology, Dhaka-1000, Bangladesh*
[b]*Department of Mechanical and Materials Engineering, University of Western Ontario, Ontario, Canada*

Abstract

Photovoltaic (PV) cells are known for poor efficiency within the range of only 6-15%, depending on the type of cells. As a result, those can convert only a small part of the absorbed solar energy into electricity, the rest is wasted as heat, which also contributes to rise in cell temperature. This heating up is undesirable for PV cells because it further decreases the electrical conversion efficiency. One viable solution to this problem is the combination of PV cells with integrated thermal collectors, known as photovoltaic-thermal (PVT) collectors. This combination usually improves the PV module efficiency compared to stand-alone PV modules, because the fluid circulating underneath the PV cells removes the heat from the cells and cools them. Among the studies concerning PVT, Delisle [1] provided a good mathematical model, where the electrical output was calculated simply by considering a linear dependence of PV efficiency with cell temperature. In the current study, following the Delisle's approach [1], a simple model configuration consisting of transpired collector absorber plate of corrugated type mounted underneath the PV cells is analyzed. The resulting mathematical system is solved numerically using multivariate Newton's method. To calculate the model output more accurately, a sophisticated model known as two-diode model is incorporated. This model provides current-voltage characteristics with maximum power point (MPP) tracker, and considers nonlinear temperature effect. The comparison of the model outputs with experimental data reveals that two-diode model behaves differently for different sets of data at different conditions.

*Keywords:*Photovoltaics; solar thermal; photovoltaic/thermal; two-diode model

---

* Corresponding author. Tel.: +880-191-182-3177;
 E-mail address: waliullahshakil@ymail.com

Nomenclature

A	area
c_p	specific heat at constant
C_0, C_1, C_{01}, C_{02}	module specific constants
e	charge of an electron
G	irradiation
h	heat transfer coefficient
I, I_{01}, I_{02}	current, diode saturation currents
k	Boltzmann constant
$\dot{m}$	mass flow rate
n_1, n_2	diode ideality factors
n_s, n_p	number of cells in the module in series, in parallel
P	power
P_{PV}	proportion of PV cells
$\dot{Q}$	heat transfer rate
R	resistance
T	temperature
U	overall heat transfer coefficient
V, V_{gap}	voltage, band gap voltage equivalent

Greek Symbols

α	absorptance
σ	porosity of collector absorber plate
σ_{sb}	Stefan-Boltzmann constant
ε	effectiveness
	emissivity
η	efficiency
μ	PV cell temperature coefficient at maximum power point

Subscripts

abs	absorbed
amb	ambient
blg	building
col	collector
cond	conductive
conv	convective
el	electrical
HX	heat exchanger
j	junction
out	outlet
p	parallel
ph	photoelectric
plen	plenum
proj	projected
rad	radiative
ref	reference
s	series
surr	surroundings
T	total
u	useful

1. Introduction

In the last few years, unglazed transpired solar collectors (UTCs) have been proven to be an effective and viable method of reducing HVAC (heating, ventilation, and air conditioning) loads and building energy consumption. With the concern of growing over energy sources and their usage, the combination of PV cells with UTCs (PV/thermal UTCs) have become a focal point of interest in the field of solar energy research. Although PV/thermal UTCs are not as prevalent as PV modules, their integration into the walls or roofing structure of a building could provide greater opportunity for the use of renewable solar energy technologies in domestic, commercial and industrial applications.

In 2008, Delisle [1] developed a mathematical model for PV/thermal UTCs and simulated it in a commercial software called 'TRNSYS'. She adapted Summer's [2] and Maurer's [3] codes to take the wind effect and considered a corrugated trapezoidal surface. The simulated configurations had PV cells directly on (a) the upper trapeziums or (b) the entire surface. The simulation results showed that when the air suction was started, the decrease in temperature caused an increase in electricity production. The configuration with PV cells only on the top was more interesting in terms of cost because it avoided placing the PV cells in the shade of the corrugation. After conducting an experiment, she compared the experimental results with her model. The model tended to overestimate the assembly temperature. This was explained by the fact that the coefficient associated with convective term did not account for wind direction or the trapezoidal shape. Besides, two modeling assumptions such as the uniformity of the suction and thermal uniformity of the panel were not met. However, when there was no suction, predicted power generation agreed with the measurement.

In the present work, Delisle's configuration (a), i.e., PV cells mounted only on the top of the corrugations is studied since it was suggested as cost effective. She developed a general mathematical model for the two configurations. Here, a simplified model (see Fig. 1), only for configuration (a), is simulated using a mathematical software called 'MATLAB'.
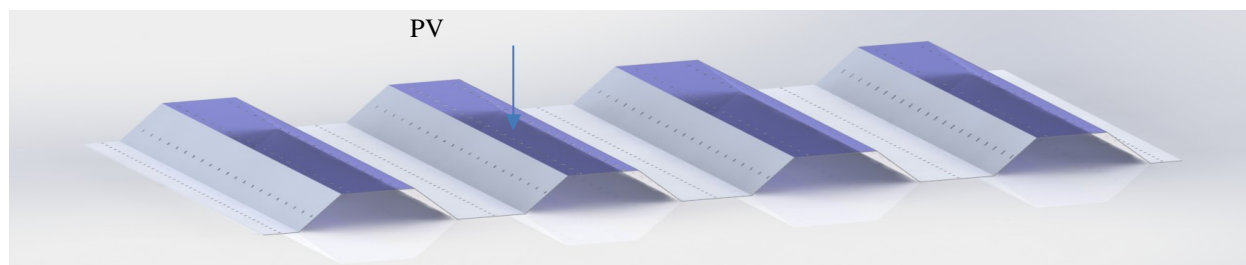

PV

Fig. 1.PVT configuration used in this study where PV cells are mounted directly on the top of trapezoidal corrugations.

2. Mathematical modelling

In order to determine the performance of the PV/thermal collector, a set of ten nonlinear equations are solved numerically using multivariate Newton-Raphson method [4] (see the flow chart for numerical simulation in Fig. 2). The first nine equations are those developed by Delisle [1]. The tenth equation for total absorbed solar radiation is formed neglecting shading and reflection since there is no such effects on the top surfaces.

The first equation is the one developed by Kutscher *et al.*[5] for an isothermal UTC that expresses the collector as a heat exchanger of effectiveness ε_{HX},

$$\varepsilon_{HX} = \frac{T_{plen} - T_{amb}}{T_{col} - T_{amb}}. \tag{1}$$

Radiation heat transfer between the wall and the back of the absorber plate $\left(\dot{Q}_{rad,wall-col}\right)$ can be expressed as,

$$\dot{Q}_{rad,wall-col} = h_{rad,wall-col} A_{col,proj} \left(T_{wall} - T_{col}\right). \tag{2}$$

Convection heat transfer from the back of the absorber plate to the plenum $\left(\dot{Q}_{conv,col-plen}\right)$ can be expressed as,

$$\dot{Q}_{conv,col-plen} = \dot{m}c_p\left(T_{plen} - T_{amb}\right). \tag{3}$$

The plate surface is considered to be at a uniform temperature. Therefore, the radiation losses from the collector to the surroundings $\left(\dot{Q}_{rad,col-surr}\right)$ is given as,

$$\dot{Q}_{rad,col-surr} = \sigma_{sb}\varepsilon_{col}\left(T_{col}^{\,4} - T_{surr}^{\,4}\right)A_{col,proj}\left(1-\sigma\right). \tag{4}$$

The convective heat losses from the absorber plate to the wind $\left(\dot{Q}_{wind}\right)$ can be expressed as,

$$\dot{Q}_{wind} = h_{wind}A_{col,proj}\left(T_{col} - T_{amb}\right). \tag{5}$$

The convective heat losses from the wall to the plenum $\left(\dot{Q}_{conv,wall-plen}\right)$ is expressed as,

$$\dot{Q}_{conv,wall-plen} = h_{conv,wall-plen}A_{col,proj}\left(T_{wall} - T_{plen}\right). \tag{6}$$

The conduction through the wall on which the collector is mounted $\left(\dot{Q}_{cond,wall}\right)$ is given as,

$$\dot{Q}_{cond,wall} = \left(\frac{1}{U_{wall}} - \frac{1}{h_{wall}}\right)^{-1} A_{col,proj}\left(T_{blg} - T_{wall}\right). \tag{7}$$
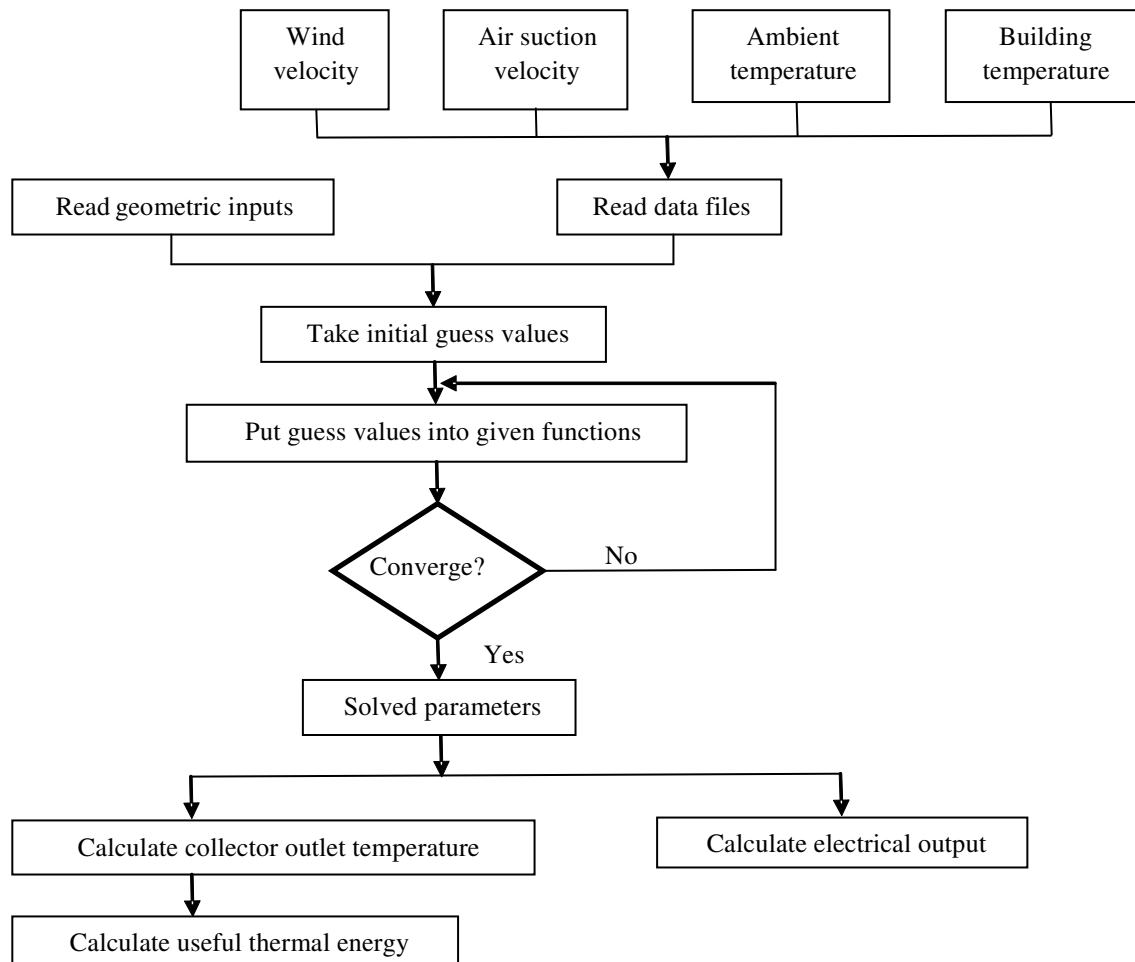
Fig. 2.Flow chart for numerical simulation of the PVT model.

The next two equations are obtained by performing energy balances on the absorber plate, on the wall located at the back of the plate, and in the holes, respectively. Those are as follows:

$$\dot{Q}_{abs} + \dot{Q}_{rad,wall-col} = \dot{Q}_{conv,col-plen} + \dot{Q}_{rad,col-surr} + \dot{Q}_{wind}, \tag{8}$$

$$\dot{Q}_{cond,wall} = \dot{Q}_{conv,wall-plen} + \dot{Q}_{rad,wall-col}. \tag{9}$$

Total absorbed solar radiation ($\dot{Q}_{abs}$) for the top surfaces of the collector except perforated portions is calculated using the absorptivity (α_{panel}) of the collector and then the electrical power output (P_{el}) produced by the PV cells mounted on the surface is deducted from this total. Thus, $\dot{Q}_{abs}$ is given by,

$$\dot{Q}_{abs} = \alpha_{panel} A_{top} (1-\sigma) G_{T,col} - P_{el}. \tag{10}$$

Now, the useful thermal energy can be calculated by,

$$\dot{Q}_u = \dot{m} c_p (T_{out} - T_{amb}). \tag{11}$$

In equation (11), the collector outlet temperature, T_{out} depends on the parameters obtained solving the above equations.

3. Determination of electric power output

In equation (10), the electrical output (P_{el}) is calculated using two different models. The first model uses a linear dependence of the efficiency of the PV module with the PV cell temperature, hence named as 'linear model' here, and the other model uses a sophisticated 'two-diode model' for PV cells.

3.1. Linear model

For simplicity, efficiency of PV module (η_{PV}) is assumed to depend linearly on the PV cell temperature as,

$$\eta_{PV} = \eta_{ref} + \mu(T_{col} - T_{ref}). \tag{12}$$

The electric power output is calculated as,

$$P_{el} = \eta_{PV} P_{PV} \dot{Q}_{abs,top}. \tag{13}$$

3.2. Two-diode model

In two-diode model, non-linearity of electrical output is taken into consideration. To implement this model, at first the PV cell temperature is calculated, then using this cell temperature, the *I-V* characteristics of the PV module is calculated with maximum power point tracking mechanism.

3.2.1 Determination of cell temperature

The cell temperature is calculated using the nominal operating cell temperature (NOCT) conditions as shown in Fig. 3.

3.2.2 Determination of I-V characteristics

According to two-diode model, *I-V* characteristics of a PV cell is governed by the equation,

$$I = I_{ph} - I_{01} \left[\exp\left(\frac{eV_j}{n_1 kT} \right) - 1 \right] - I_{02} \left[\exp\left(\frac{eV_j}{n_2 kT} \right) - 1 \right] - \frac{V_j}{R_p}, \tag{14}$$

where,

$$V_j = V + IR_s. \tag{15}$$

Unfortunately, equation (14) cannot be solved analytically [6]. It can be solved if either voltage or current is known by means of numerical iterations. Therefore, one of them is assumed and the other is iterated. Moreover, the dependence on the environmental conditions is not included in this equation, e.g., there is no crossover for an

increase in temperature. This is included by modifying the photocurrent and the diodes' saturation currents as follows:

$$I_{ph} = (C_0 + C_1 T) AG, \tag{16}$$

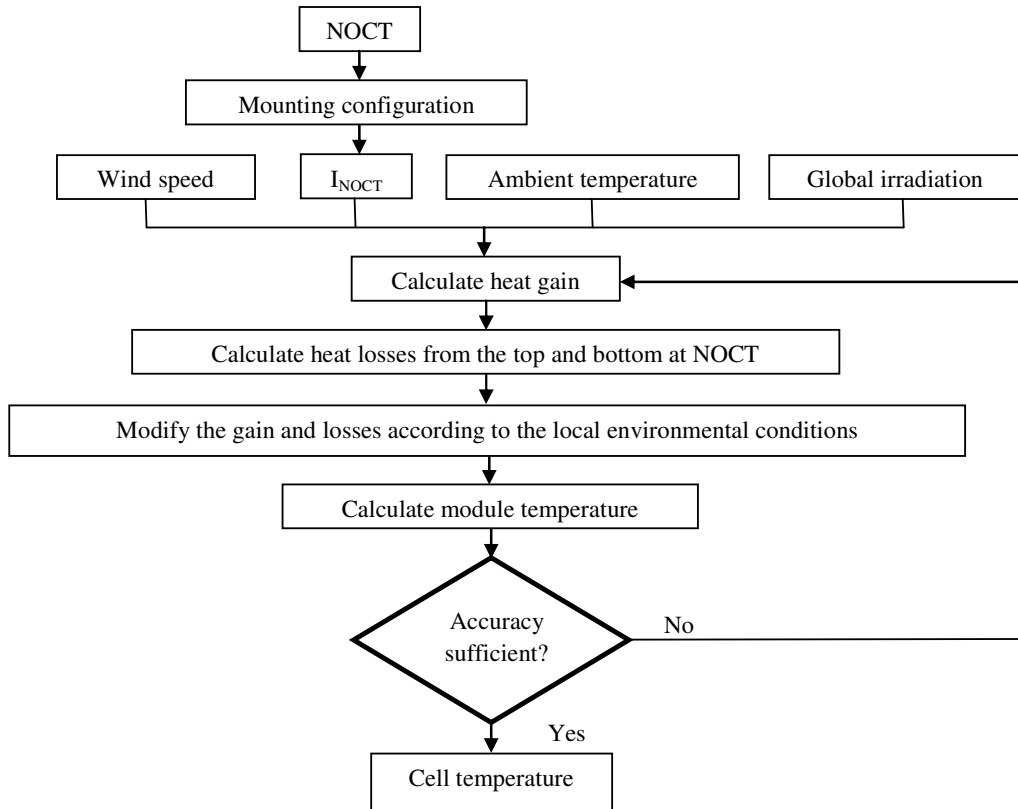$$I_{01} = C_{01} T^3 \exp\left(-\frac{eV_{gap}}{kT}\right), \tag{17}$$

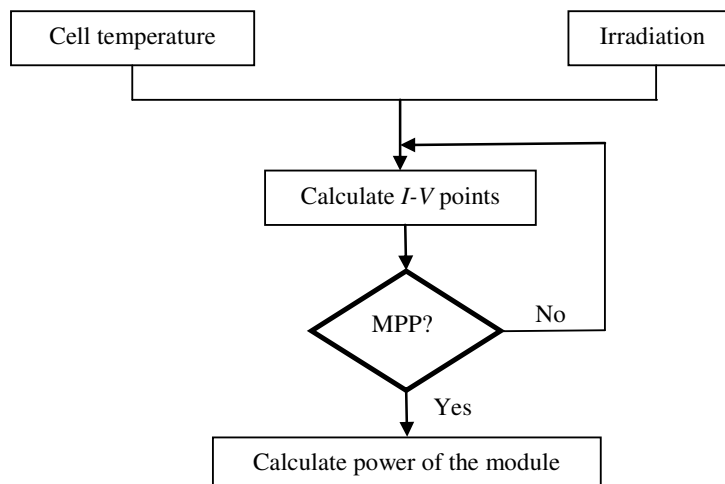Fig. 3: Flow chart to calculate cell temperature.

Fig. 4. Flow chart for determination of *I-V* characteristics.

$$I_{02} = C_{02} T^{\frac{5}{2}} \exp\left(-\frac{eV_{gap}}{2kT}\right). \tag{18}$$

These set of equations is the most accurate way to calculate the performance of a solar cell at any given environmental condition. Once the values of I_{ph}, I_{01} and I_{02} are known from equations (15) – (17), I and V are determined by numerical iterative procedure. Then, electrical power of the module can be calculated by,

$$P_{el} = n_s n_p IV. \tag{19}$$

The flow chart for determination of I-V characteristics as described above is presented in Fig. 4.

4. Results and discussions

In this work, we have taken Delisle's experimental data [1] for three days and compared them with our output. For the data of 29th August 2007, the simplified model seems to overestimate the thermal output (see Fig. 5(a)). For the other two days, the simplified model underestimates for a certain range (Figs. 5 (b) and (c)). This day-to-day variation may be caused by variation in weather, since the output depends greatly on the exposure of sun. In the present calculation, sky temperature is assumed to be a function of ambient temperature and cloud cover factor is ignored. The consideration of cloud cover factor might improve the result. However, the trend of the graph for theoretical thermal output seems to agree with that of experimental output. This indicates that the simplified model is valid.
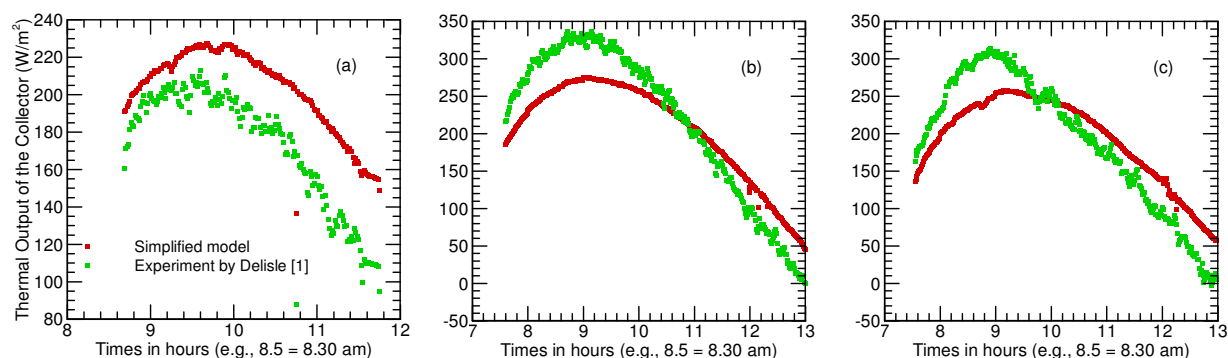
Fig. 5. Comparison of thermal outputs for (a) 29th August, (b) 31st August and (c) 2nd September.

After incorporating two-diode model, we have compared the electrical outputs with experimental data (see Fig. 6). Again, the results seem to be different for 29th August and the other two days. It seems that for 29th August, for a certain region, the two-diode model conforms better to the experimental data than Delisle's model. For the other two days, both overestimate in a certain region and the two-diode model overestimates more by around 6%. The reason for this variation is already discussed.
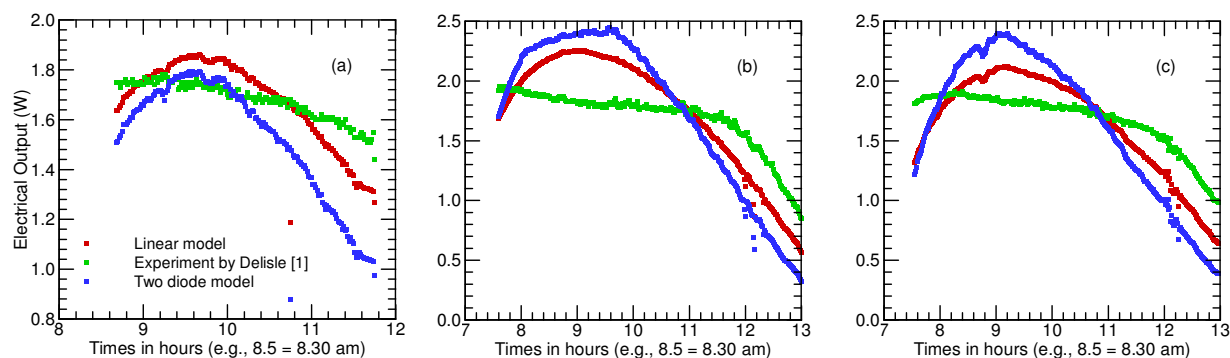

Fig. 6. Comparison of electrical outputs for (a) 29th August, (b) 31st August and (c) 2nd September.

5. Conclusion

In this study, a mathematical model is developed for PV cells combined with UTCs following the approach of Delisle [1]. The study reveals the possibility that two-diode model may analyze the electrical behavior of PVTs better depending on the weather conditions and other physical variables. The outputs are compared with the experimental data and some discrepancies are discovered. For removing these discrepancies, and improving the model and suiting it with respect to Bangladesh, the followings are recommended:

- In this work, sky temperature is assumed to be a function of ambient temperature. More sophisticated approach including cloud cover factor [7] should be taken to improve the calculation.
- Since, shading and reflection effects can be ignored for configuration (a), absorbed solar radiation is calculated much simplistically. More sophisticated approach should be taken for the calculation of absorbed solar radiation even though shading and reflecting effects are ignored.
- In the radiation converter, collector azimuth angle is assumed to be zero. Further investigations regarding different values of angles should be carried out.
- In this work, only trapezoidal corrugation is examined for the collector. In Bangladesh, tins of sinusoidal corrugation are easily available. Therefore, further investigations should be carried out regarding sinusoidal corrugations and tin as an absorber material.

Acknowledgements

References

[1] V. Delisle, Analytical and Experimental Study of a PV/Thermal Transpired Solar Collector, University of Waterloo, Waterloo, Ontario, Canada, 2008.
[2] D. Summers, Thermal Simulation and Economic Assessment of Unglazed Transpired Collector Systems, University of Wisconsin, Madison, 1995.
[3] C. Maurer, Field Study and Modeling of an Unglazed Transpired Solar Collector System, North Carolina State University, Raleigh, 2004.
[4] T. Sauer, Numerical Analysis, Second Edition, Pearson, 2011.
[5] C.F. Kutscher, C. Christensen, G. Barker, Unglazed transpired solar collectors: heat loss theory, Journal of Solar Energy Engineering, Transactions of the ASME, 115(3) (1993) 182-188.
[6] R. Gottschalg , Introduction to PV Cell Technology, Photovoltaic Cell for Bangladesh, Editors: A.K.M.S. Islam, D.G. Infield, 2001, pp. 49-84.
[7] L.T. Wong, W.K. Chow, Solar radiation model, Applied Energy, 69 (2001) 191-224.

6th BSME International Conference on Thermal Engineering (ICTE 2014)

The Production of Ethanol from Micro-Algae Spirulina

Md. Nahian Bin Hossain, Joyanta Kumar Basu, Dr. Mohammad Mamun

Department of Mechanical Engineering, Bangladesh University of Engineering and Technology (BUET)

Abstract

This study ascertained the technical potential of producing bio fuel from naturally occurring micro algae spirulina. The algae are grown by BCSIR and the collected algae are examined. The growing environment contains nitrates, phosphates and carbon dioxide that come from atmosphere. The overall research work consisted of manual and mechanical drying of algae, grinding and subjecting the algal matter to acid hydrolysis to extract carbohydrates to form an algal sugar solution. Fermentation of that solution was performed with *Saccharomyces cerevisiae* to produce ethanol. The presents of ethanol in the solution assures the ultimate desired destination of the work. An average of 15.2 g/L of reducing sugar was extracted in the hydrolysate showing that microalgae have significant usable carbohydrates after hydrolysis to conduct this research work. Ethanol percentage varies with the variation of hydrolysis time, concentration of sulfuric acid and fermentation time. The average value of ethanol percentage varies between 0.85-1.0 percent among the samples. Although the ethanol percentage is not economical for this algae but the main task of establishing the process of bio fuel production from micro algae comes to a successful end. This process gives the assurance and defined way of bio fuel production from other carbohydrate enriched micro algae.

1. Introduction

1.1 General Overview

A biofuel is a fuel that contains energy from geologically recent carbon fixation and produced from living organisms. These fuels are made by a biomass conversion. This biomass can be converted to convenient energy containing substances in three different ways: thermal conversion, chemical conversion, and biochemical conversion. This biomass conversion can result in fuel in solid, liquid, or gas form. This new biomass can be used for biofuels. Bioethanol is an alcohol made by fermentation, mostly from carbohydrates produced in sugar or starch crops such as corn, sugarcane, or sweet sorghum. Ethanol can be used as a fuel for vehicles in its pure form, but it is usually used as a gasoline additive to increase octane and improve vehicle emissions. As the biofuel production from typical crop sources creates a challenge to human food supply market so the world is now moving towards the production of biofuel from algae. Enormous source of sea micro and macro algae illustrates a new era of alternative fuel research opportunities. Among algal fuels' attractive characteristics are that they can be grown with minimal impact on fresh water resources, can be produced using saline and wastewater, have a high flash point, biodegradable and relatively harmless to the environment if spilled.

1.2 Motivation and Background

Fossil fuel sources almost come to an end. Nuclear energy source endangered the human civilization from the view point of political restless situation and aggression. Solar and wind energy still can't capable to cop up for meeting the requirement of alternative energy. The lack of sustainable technological development in different sectors also makes it difficult to use the wind, solar or other sources of energy as the replacement of present fossil fuels. So biofuel gives a comfortable opportunity of replacement of fossil fuels with present technological capabilities. Through the world biofuel is considered as a clean and environment friendly fuel source. There are various social, economic, environmental and technical issues these include the effect of moderating oil (petroleum) prices, the food vs. fuel debate, poverty potential, carbon (C) & other carbon base emissions levels, sustainable biofuel production, deforestation and soil erosion, loss of biodiversity and impact on water resources. The most important ethical controversy that arises for the production of bio fuel is "food vs. fuel". It can be easily said that biofuel production from human food sources makes a huge danger to food security through the world. The poor regions from the world have to deal with more complex situation of food prices for this reason. On the other hand it is not possible to give up the prospects of biofuel production for better future. So the optimum and acceptable solution comes with the use of micro algae for biofuel (ethanol) production. Microalgae especially marine microalgae are highly enriched with carbohydrate content which can be used for ethanol production instead of sugarcane or other human food crops.

1.3 Objectives

a) The main objective was to establish a complete process for ethanol production from micro algae spirulina. the production of ethanol from spirulina was still being a completely unknown chapter. The low carbohydrate content of spirulina makes it difficult and challengeable to go for ethanol from spirulina. Although some government research is planning to go through for this work at near future but we have wanted to establish the definite process that can be useable in future.

b) Process standardization was the secondary object of ours. Though after finding out the production process of ethanol from micro algae it is difficult to standardize the process due to time and lab facility limitation we have accepted the challenge. For the process standardization dry time variation of algae, acid hydrolysis variation, acid concentration variation, fermentation time variation with samples is planned. To find out an optimum position of ethanol production from our established process is the summarized secondary objective of this thesis work.

2. Literature Review

2.1 Ethanol

Biologically produced alcohols, most commonly ethanol, and less commonly propanol and butanol, are produced by the action of microorganisms and enzymes through the fermentation of sugars or starches (easiest), or cellulose (which is more difficult). Alcohol fuels are produced by fermentation of sugars derived from wheat, corn, sugar beets, sugar cane, molasses and any sugar or starch. The ethanol production methods used are enzyme digestion (to release sugars from stored starches), fermentation of the sugars, distillation and drying. Ethanol can be used in petrol engines as a replacement for gasoline by mixing with gasoline to any percentage. Most existing car petrol engines can run on blends of up to 15% bioethanol with petroleum/gasoline. Ethanol has a smaller energy density than that of gasoline; this means it takes more fuel (volume and mass) to produce the same amount of work. An advantage of ethanol (CH_3-CH_2-OH) is that it has a higher octane rating than ethanol-free gasoline available at roadside gas stations, which allows an increase of an engine's compression ratio for increased thermal efficiency. In high-altitude (thin air) locations, some states mandate a mix of gasoline and ethanol as a winter oxidizer to reduce atmospheric pollution emissions. Ethanol has roughly one-third lower energy content per unit of volume compared to gasoline. This is partly counteracted by the better efficiency when using ethanol (in a long-term test of more than 2,1 million km, the BEST project found FFV vehicles to be 1-26 % more energy efficient than petrol cars The BEST project), but the volumetric consumption increases by approximately 30 %, so more fuel stops are required.
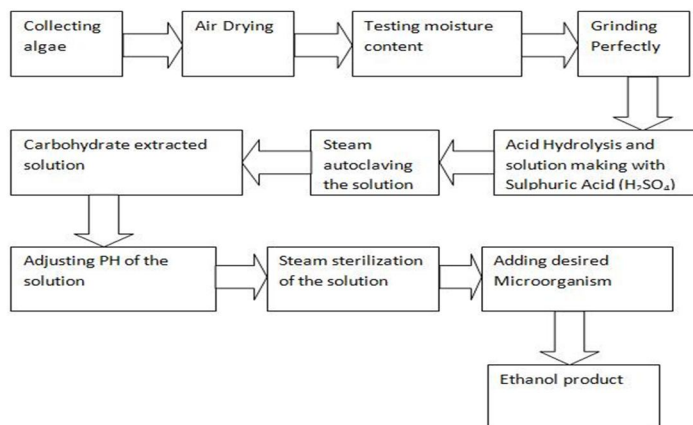
2.2 Why Spirulina

Spirulina is a cyan bacterium that can be consumed by humans and other animals and is made primarily from two species of cyan bacteria: *Arthrospira platensis* and *Arthrospira maxima*. Spirulina is simple one-celled microscopic blue - green algae with the scientific name Arthrospira platensis. Under a microscope, spirulina appears as long, thin, blue-green spiral threads. The odor and taste of spirulina is similar to seaweed. Spirulina can be found in many freshwater environments, including ponds, lakes, and rivers. It thrives best under pesticide-free conditions with plenty of sunlight and moderate temperature levels, but it is also highly adaptable, surviving even in extreme conditions. There remain some basic reasons behind the choice of spirulina as the production substance

 a) Spirulina is the most easily collectable algae than others in Bangladesh.
 b) According to the availability and easily collectability spirulina is the lowest cost algae than others.
 c) With the present work for algal fuel in Bangladesh, spirulina is the most common one for the technology is available here. BCSIR and CARS and some laboratories in BUET have the known facility to work with spirulina and widespread expertise knowledge is available for this.

3. Experiment Procedure

3.1 Process outline

Process flow chart

3.2 Process Detailing

- Collecting Algae

    We have got almost 1000 gm. dry spirulina from BCSIR for research purpose. This algae was collected from the plant of spirulina which is run under a senior scientific researcher of BCSIR.

- Air Drying & Testing Moisture Content

    For testing the variation of ethanol percentage in the final solution according to the variation of air drying time, three different air drying times was used. These are 1 day air drying, 2 days air drying, and 3 days air drying

- Grinding Perfectly

    For the preparation of algal solution perfect grinding of coarse algal powder was very important. Because of the adjustment of pH of the solution depends upon the finer powder of algae. the suspension of algal powder will hinder the cell degradation process of algae. That may result low carbohydrate extracted solution and thus fermentation with microorganism may not be performed. The grinding of coarse algal powder was done by mortar and pestle at lab.

- Acid Hydrolysis and Solution Making with H_2SO_4

  Hydrolysis is necessary to convert starches to fermentable sugars. The cell degradation of carbohydrates to fermentable sugar is basically done with the hydrolysis process by making solution with Sulphuric Acid. The term "Acid Hydrolysis" is also applied to certain nucleophilic addition reactions, such as in the acid catalyzed hydrolysis of nitriles to amides. Acid hydrolysis does not usually refer to the acid catalyzed addition of the elements of water to double or triple bonds by electrophilic addition as may originate from a hydration reaction. For our work purpose we have made three sample solutions with the variation of Sulphuric acid percentage. Every sample solution is 500 ml solution. This solution was made with algal powder and distilled water. Three samples were made with 1%, 1.5% & 2% sulphuric acid by weight percentage.

- Steam Autoclaving the Solution

  An autoclave is a device used to sterilize equipment and supplies by subjecting them to high pressure saturated steam at 120-130°C for around 15–30 minutes depending on the size of the load and the contents. In our process at this step autoclaving is required for both the perfect cell degradation that means carbohydrate cell coming out form the spirulina cell and for assisting the acid hydrolysis process. We complete the process in the laboratory of Department of Microbiology, University of Dhaka. Three samples are made according to the autoclaving time 15 min, 20 min, and 25 min at $125^0 C$. The pressure of the autoclave was 15 psi.

- Carbohydrate Extracted Solution

  After the autoclaving process is finished the solution we get that is called the carbohydrate extracted solution. At this stage the solution is with divided carbohydrate cells. A manual filtering process is done here to find out any coarse particles of algal powder. This is important for the next step of PH adjustment.

- Adjusting PH of the Solution

  A suitable pH value (4.5-5) must have to be adjusted for the fermentation. In our process pH is adjusted by using manual pH meter. For this process concentrated Sulfuric acid's diluted solution and NaOH solution were used. Although it was tried to make the sample solution as much as better from suspension type but the pH adjustment took a long time. This may cause from the little bit precipitation formation tendency of the solution. The pH adjustment of solution is done at the lab with the help of experienced lab attendant. Almost for all the samples the pH was tried to keep at the range of 4.5-5.0.

- Steam Sterilization of the solution

  Sterilization (or sterilisation) is a term referring to any process that eliminates (removes) or kills all forms of life, including transmissible agents (such as fungi, bacteria, viruses, spore forms, etc.) present on a surface, contained in a fluid, in medication, or in a compound such as biological culture media. For our process sterilization ensures the absence of any other microorganisms in the solution that can hamper the fermentation process. In our process we have used steam sterilization. This is almost the same process as the autoclaving. The same autoclave is used here for the sterilization. The sample solution is kept in the autoclave for 15 minutes at $121^0 C$ and thus the solution is sterilized.

- Adding Desired Microorganism

  In this step we have added the desired microorganism into our sterilized solution. In our process the microorganism is *Saccharomyces cerevisiae,* commonly known as yeast. The medium of this microorganism is made at the lab of Centre for Advances Researches in Science (CARS), University of Dhaka. Yeast can be grown in either liquid medium or on the surface of a solid agar plate. Yeast cells will grow on a minimal medium containing dextrose (glucose) as a carbon source and salts that supply nitrogen, phosphorus, and trace metals. Yeast cells grow much more rapidly in the presence of rich medium that contains reagents such as yeast extract and bactopeptone.
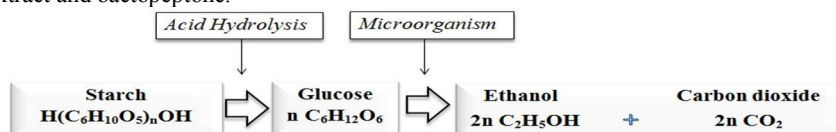
  Yeast strains can be stored at −70°C in 15% glycerol and are viable for more than 3 yr. alternatively, they can be stored at 4°C on slants of rich medium for 6 month to 1 yr. According to the information of CARS for our process the yeast medium is developed with the simple general condition. After adding with the solution a fermentation time is required for the ethanol production. In our study we have made three samples by varying the fermentation time as 3 days, 5 days and 7 days.

- Ethanol Product

  Our final solution is containing ethanol or not. A simple chemical experiment is used here for this purpose. Here we have used two types of solution. They are (i) 1M NaOH (Sodium Hydroxide) solution & (ii) 0.5 M Iodine Solution. 20 drops of solution was taken in a test tube using pipette. Then 50 drops of iodine solution was added in that solution. After those 20 drops of Sodium Hydroxide solution is added. After 2 minutes the solution is observed carefully. The solution in the test-tube was being cloudy and then a yellow precipitate of triiodomethane (iodoform) had seen.

- Alcohol Meter

  The simplest method for getting the ethanol percentage is the use of alcohol meter. For this process a suitable amount of solution is taken in a volumetric flask. The weight of the solution is measured carefully.

- Spectra photometrical experiment

  We have used this method only for one sample as Chromium is a highly carcinogenic material and the experiment with this chemical reagent is very hazardous and In this method we have to use a chemical reagent named pyridinium chlorochromate ($C_5H_5N. ClCrO_3H$). In this process some diluted standard solution like 0.1 %, 0.2 %, .7 %, 0.8 %.....1% is made with standard ethanol and distilled water. After that 5 ml of our very prepared standard solution is mixed with 2 ml of pyridinium chlorochromate solution. It is then kept in complete darkness for 1hr. Then using the spectra photometer absorbance at 588 nm concentration of different solution is achieved. Then our ethanol solution and pyridinium chlorochromate solution is used to get the absorbance. Then comparing with the standard data we got the % ethanol present in the solution.

4. Results and Discussions

The main target of this research was to find out the ethanol presence in the solution that means the establishment of ethanol production procedure from spirulina. According to this it can be easily said that our result is positive. And this research is successful. Although our main objective was to set up a definite process for ethanol production from micro algae spirulina by using its carbohydrate content but we had a secondary objective of process standardization. We have made various samples to fulfill our secondary objective. Four types or sample variation were done by us.

4.1 Air drying time variation

It is seen that we have got the highest percentage ethanol with the sample solution of 3 days air drying. Three sample data are given in Table 01. The reason may behind this the moisture content. As the moisture content was reduced in the algal powder so the finer algal powder was made. As a result the solution became more fermentable and ethanol percentage was increased. Graphical presentation of those data is given in Figure 01.

4.2 Sulphuric acid concentration variation

Three samples were made with the variation of Sulphuric acid concentration. Those were with 1 %, 1.5 % and 2 % Sulphuric acid. Three sample data are given in Table 02. The results show that the highest ethanol percentage is obtained with the sample of 2 % Sulphuric acid. The basic reason behind this is the higher concentration of Sulphuric acid the reducing sugar concentration in the solution also goes high. Graphical presentation of those data is given in Figure 02.

4.3 Hydrolysis time variation

Three samples were made by varying the autoclaving (hydrolysis) time of the solution. Three sample data are given in Table 03. Here we have got the highest percentage ethanol solution with the highest hydrolysis time. The same reason as like the Sulphuric acid concentration variation responsible here for the result. For a longer autoclaving time the hydrolysis process get more duration to occur. As a result the fermentable sugar concentration is increased in the solution which gives the higher percentage ethanol. Graphical presentation of those data is given in Figure 03.

4.4 Fermentation time variation

This is done by varying the time of fermentation after the desired microorganism was added to the solution. The first sample was kept for three days fermentation, which is the standard fermentation time. Another two samples was kept for five and seven days. Three sample data are given in Table 04. We got the highest ethanol percentage at the solution of seven days fermentation. This caused because of more fermentation time the microorganism gets more time to increase its concentration through the solution. As the concentration of microorganism is increased, so all of the fermentable sugar can convert to ethanol. As a whole ethanol percentage is increase. Graphical presentation of those data is given in Figure 04.

Sample No.	Air drying time (days)	Ethanol percentage
1	1	0.85
2	2	0.89
3	3	0.965

Table 01: Air drying time and ethanol percentage
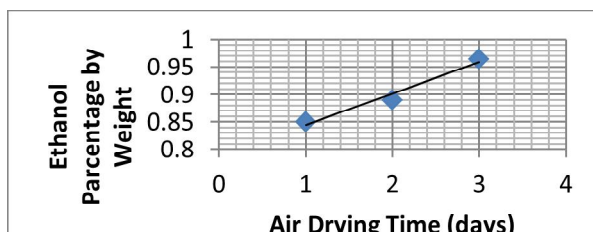
Fig 01: Air drying time vs. ethanol percentage graph

Sample No.	Concentration of H_2SO_4 (% weight)	Ethanol Percentage (%)
1	1.0	0.865
2	1.5	0.954
3	2.0	0.989

Table 02: Acid concentration an ethanol percentage
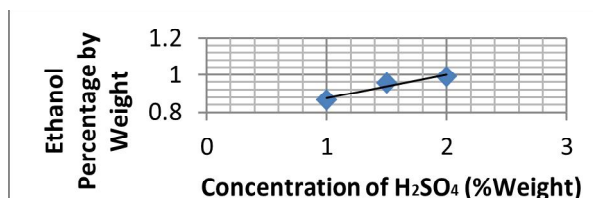
Fig 02: Acid concentration vs. ethanol percentage graph.

Sample No.	Hydrolysis time (min)	Ethanol percentage
1	15	0.88
2	20	0.96
3	25	0.998

Table 03: Hydrolysis time and ethanol percentage
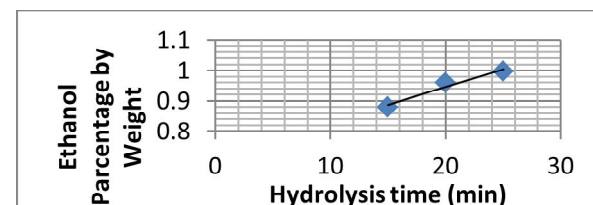
Fig 03: Hydrolysis time vs. ethanol percentage graph.

Sample No.	Fermentation time (days)	Ethanol percentage
1	3	0.89
2	5	0.958
3	7	0.99

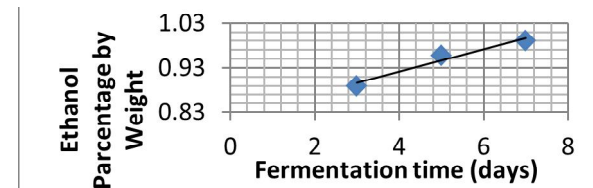Table 04: Fermentation time and ethanol percentage

Fig 04: Fermentation time vs. ethanol percentage graph.

References

[1] Adey, W.H. (1990). Water purification system and apparatus, U.S. Patent 88-228114.
[2] Bruhn, A., Dahl, J., Nielsen, H.B., Nikolaisen, L., Rasmus- sen, M.B., Markager, S., Olesen, B., Arias, C., & Jensen, P.D. (2011). Bioenergy potential of Ulva lactuca: Bio- mass yield, methane production and combustion, Biore- source Technology, 102, 2595-2604.
[3] Burgess, R.M., Pelletier, M.C., Ho, K.T., Serbst, J.R., Ryba, S.A., Kuhn, A., Perron, M.M., Raczelowski, P., & Can- twell, M.G. (2003). Removal of ammonia toxicity in marine sediment TIEs: A comparison of Ulva lactuca, zeolite and aeration methods, Marine Pollution Bulletin, 46, 607-618.
[4] Greer, D.E., & Ziebell, C.D. (1972). Biological removal of phosphates from water, Journal of the Water Pollution Control Federation, 44, 2342-2348.
[5] Hirayama, S., Miyasaka, M., Amano, H., Kumagai, Y., Shimojo, N., Yanagita, T., & Okami, Y. (2004). Functional sulfur amino acid production and seawater remediation system by sterile Ulva sp. (Chlorophyta), Applied Biochemistry and Biotechnology, 112, 101-110.
[6] Liang, S., Shi, X., Han, X., & Zhang, G. (2010). Comprehensive bioremediation method for eutrophic seawater net cage culture zone, Faming Zhuanli Shenqing, 201010168350, 6

6th BSME International Conference on Thermal Engineering (ICTE 2014)

Simulation and Optimization of Solar Desalination Plant Using Aspen Plus Simulation Software

Mojibul Sajjad [a], Mohammad G. Rasul [b]

a Researcher, School of Science & Engineering, Central Queensland University, Rockhampton,Queensland,Australia
b Associate Professor,, School of Science & Engineering, Central Queensland University, Rockhampton,Queensland,Australia

Abstract

Of the total global water, 94% is salt water from the oceans and the remaining 6% is fresh. The shortage of fresh water is a problem that has continued to challenge third world countries, and over time has become increasingly evident in developed nations around the globe. With a combination of contributing issues such as overpopulation and changes in weather and climatic conditions, the demand for alternate approaches to fresh potable water supply has increased dramatically. The paper develops a computational model to simulate the performance of a small scale solar desalination plant. The model is validated with experimental results found in the literature. The validated model is used to optimize the functional parameters of a desalination plant and in turn, enhance the recovery rate and product quality of the system. The model is suitable for brackish and seawater desalting applications specific to the climatic conditions of coastal Queensland, Australia. Aspen Plus is the process simulation software that was used for the modelling. The outcomes of the study is a validated process simulation model of a small scale solar desalination plant, optimization of this model for better utilization of current technologies and methods of improving performance, efficiency and recovery and reducing operational limitations.

Keywords: Solar desalination plant, Aspen Plus software, Simulation, Optimisation.

1. Introduction

Among the water reserves in this world, nearly 6% is fresh water and remaining is saline water. Approximately 27% of all fresh water reserves are in glaciers with 72% located underground with the remaining 1% accounted for in the limited fresh water dams, streams, lakes and river systems throughout the world. Desalting technologies have evolved over the last 50, impacting lives with considerable effect especially in remote regions of the Middle East and

North Africa where the lack of fresh water was previously impeding development. A major development and realization of the potential of desalination was first discovered in the mid 1940's during WWII when various military camps in arid areas required potable water for the troops. Following the war, further industrial advances continued into the 1960's [1]. Over time, the maturity of both desalination processes and renewable energy sources have been proven by social acceptance from implementations causing growth and development of both technologies [2, 3].

Australia is both the driest inhabited continent on earth and the highest consumer of water per capita by international standards [4]. Of all continents it has the smallest area of permanent wetlands, the least river water and the lowest run off along with the most variable rainfall records in the world [4]. In recent times, a combination of technology advancements and actions taken by leading authorities and governments has seen an increased awareness in the possibilities of alternative fresh water sources. After studies undertaken as a part of the National Water and Resources Audit found there would be a likely decline in the quality of water supplies over the next 50 years [5], measures including the introduction of zoned water restriction regulations in Australia have helped to stem the usage of the diminishing fresh water reserves. Additionally, extensive investigations and research have provided promising alternative methods of obtaining potable water.

Of all the investigated technologies, desalination has emerged as being one of the most promising solutions to providing an alternative means of fresh water supply. Considering its climatic conditions and suitability, until recent times, Australia has comparatively limited operational expertise and experience in desalination technologies and falls behind world leaders in the Middle East and North Africa where almost half of the world's desalting capacity lies. Isolated mining towns and small communities as well as industrial processes such as power stations that require exceedingly high qualities of water are the main users of desalination technologies in Australia [5]. Over the past decade, several plants in Australia have been constructed or have been proposed for public potable water supply such as the Perth based 130ML/day RO plant which has the potential to expand with additional extensions. Desalination technology has also been introduced to offset the amount of potable water used for purposes other than drinking. In an Australian first, a water mining treatment process operating at Rocks Riverside Park in Queensland utilizes a low cost, sustainable natural treatment and filtration process to convert wastewater to quality non potable drinking water for parkland irrigation saving up to 360kL of potable water daily [6].

In 2009, the Commonwealth Scientific and Industrial Research Organization (CSIRO) conducted a report to investigate the status of desalination on a national scale. Of the 46 desalination plants investigated, 45 operated as reverse osmosis (RO) plants. It was found by comparison with Australia's total potable, industrial and agricultural water consumption in 2004-05 (51.5 GL/day), the amount of desalted water used in 2008 is 0.57% of that total (0.294 GL/day) [5]. These figures represent the potential Australia has to develop and implement desalination technology and with further reports showing that the cost of seawater RO plants have fallen by 300% in the past 15 years [7], it is now more economically and financially feasible than ever.

The main aim of this study was to develop a process simulation model of a small scale solar desalination plant using programs and software that decompose the process into its constituent elements for the purpose of predicting performance using analysis techniques. These process characteristics included feed flow rates, temperatures, pressures, compositions, and specific properties of equipment. Through the input parameters and design equations, the model considered and simulated the three stages of the process including feed pre-treatments, structure and desalination technique and the final permeate and retentate outputs. These outputs were then validated against data from recognized past studies which had been completed using geographically appropriate data that coincided with the Central Queensland area, Australia.

Once the outputs were verified, the model was then adjusted and optimized by altering a number of variables including adjustments to the configuration of the desalination process, quality of feed water, level of pre-treatment and extent of filtration in an effort to increase the performance, recovery rate and efficiency, thus impacting on the required input power, magnitude of brine waste, maintenance requirements and running costs. The purpose of the optimization was to determine the most realistically achievable, sustainable and environmentally responsible small

scale arrangement to produce potable water for a community subject to a typical Queensland climate with access to abundant supply of brackish or seawater.

2. Methodology and Experimental Measurement

2.1. Component of the System

The system to be replicated and used for validation purposes consists of three main sections throughout the entire desalination process, pre-treatment and pressurization, power supply and the RO membrane arrangement. The system under investigation has no grid connection and is powered completely from solar energy obtained through a photovoltaic arrangement. Figure 1 outlines the system schematic with arrows outlining direction of flow. The system makes use of a salt water feed intake from a beach well before introducing a simple coarse filter pre-treatment ensuring suspended solids are removed before the feed stream is pressurized through the positive displacement pump which is powered by the solar PV array. A flow meter and pressure relief valve monitor the flow rate and pressure of the system downstream of the pump before the membrane arrangement desalts the feed into the two final output streams of brine reject and the product permeate.
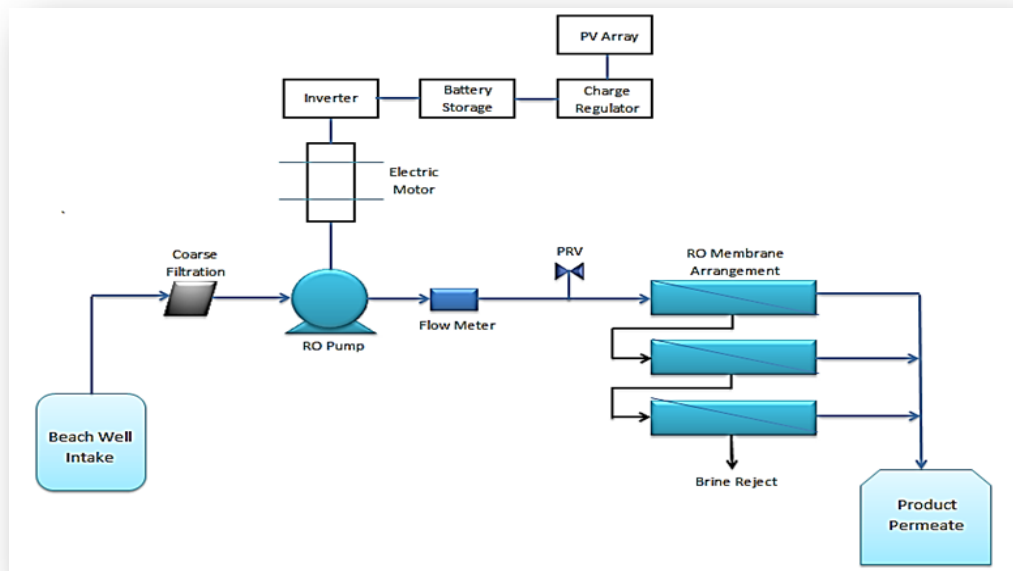

Figure 1: Reference Data System Schematic.

Power Source: Harnessing solar energy are 10 off 80W Sharp NE-80EJEA poly-crystalline panels connected in parallel. This PV array gives a DC output which is delivered to a Xantrex DR1512E 1500W inverter with integrated battery storage and charging element. The inverter transforms the DC supply into an AC voltage before it reaches the AC induction motor. Table 1 summarizes characteristics of the PV modules and the main PV system elements.

Pressure Source: The pump powered by the electric motor is a Hydra-cell D/G-03X positive displacement pump. With the pressure and flow rate of the feed stream being two influential characteristics on the output of the system, these are monitored and mediated by both a flow meter and pressure reducing valve. These elements are critical in the consideration of both the simulation and experimental operation as they ensure large fluctuations are eliminated

allowing single values to be inputted into a model while maximum design specifications for both the pump and RO membranes is not exceeded. These elements are also versatile instruments in practical applications to mimic simulation results once optimization has been carried out.

Desalination Source: The membrane configuration used in the referenced data set is a 3 membrane arrangement in series. Each product stream feeds back into one permeate line while the brine stream feed the preceding membrane before discharging from the final membrane. Although additional membranes results in a greater pressure loss over the series configuration, investigations from the reference data suggest a smaller applied pressure is required for an increased recovery rate. The retentate discharge is also at a pressure that an energy recovery device can be implemented into the system to enhance the prospect of turning the configuration into an energy generating operation. In simulating the above system, the AspenPlus software [8] allows the user to define the feed water characteristics. The temperature, pressure, volumetric flow rate and concentration are among the original input variables used to define the feed water.

Table 1: PV Module and System Characteristics

Module Characteristics System Elements		System Elements	
Cell Type	Poly-Crystalline Silicon	PV Array	10 off Sharp NE-80EJEA poly-crystalline panels
Number of Cells	36 (series)	Charge	Plasmatronics PL60 60A Solar Regulator
Open Circuit Voltage	21.6V	Regulator	
Maximum Power Voltage	17.3	Battery	4 off US185, 12V, 195A.hr flooded cell
Short Circuit Current	5.16		lead acid battery in parallel
Maximum Power Current	4.63	Inverter	Xantrex DR1512E 1500W
Maximum Power	80W	Electric	Baldor EL3507 115/230V, 559W, 0.75hp
		Motor	AC induction motor

2.2 Input Data

Feed Water Characteristics: With the model being proposed to simulate operation in the climatic conditions of Yeppoon in Central Queensland, feed water characteristics were chosen to replicate those in the case study location. These properties of temperature, pressure (based on osmotic pressure of the feed water concentration) and salinity concentration are outlined in Table 2 as used in the simulation model. The system was designed to produce 0.5m3/day product water under a 6 hour operational cycle coinciding with the time of day that yields the highest solar potential. The feed water flow rates used were defined in three arrangements as the model was developed. The single, double and triple membrane arrangements in series adopted varying flow rates. Because of this, the development of the Aspen Plus model adopted the same progression to ensure validation was accurate. The variable feed flow rates used for validation are shown in Table 3

Table 2: Feed water characteristics used for validation and simulations

Description	Value
Temperature (oC)	25
Pressure (bar)	34.5
Feed concentration (ppm)	35

Table 3: Feed water flow rates used for validation and simulations

System arrangement	Feed flow rate (m3/hr)
Single	0.830
Double	0.506
Triple	0.414

Membrane Characteristics: The modelled and simulated membrane was a spiral wound SWC-2540 manufactured by Hydranautics and used in the simulation. This particular membrane was of a thin film composite polyamide construction and had an active area of 2.37m2. The membrane performance and efficiency is based on the primary characteristics of percentage salt rejection and maximum permeate flow relative to geometry under ideal conditions. As outlined on the manufacturer's website, these properties are 99.4% and 2.0m3/day respectively. Table 4 outlines the maximum application conditions at which the membrane is designed for general use. For specific or prolonged use, operation at more conservative levels would ensure the longevity and performance of the device. Dimensions A, B and C mentioned in the table are described in Figure 2.

Table 4: Maximum application conditions [9]

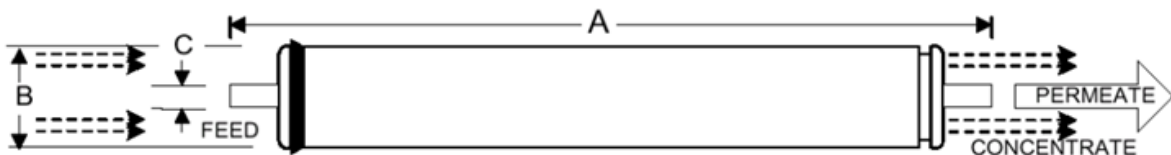| In put parameter	Values
Maximum Applied Pressure	6.9 MPa
Maximum Chlorine Concentration (not applicable for current model)	< 0.1 ppm
Maximum Operating Temperature	45°C
pH Range (for continuous use)	3.0 – 10.0
Maximum Feed Water Turbidity	1.0 NTU
Maximum Feed Flow	23 L/m
Maximum Pressure Drop for each Element	70 KPa
Dimension A	1016 mm
Dimension B	61 mm
Dimension C	19.1 mm

Figure 2: Membrane dimension

Product Characteristics: The primary aspect of the permeate that was required to be accurately simulated to achieve validation was flow rate. As a result of known feed flow, the recovery rate was also an indication of validity of the model. Table 4 shows the properties of the permeate for the corresponding system arrangements.

Table 5: Product Permeate Properties (Schrader, Rasul 2008)

System Property	Single Arrangement	Double Arrangement	Triple Arrangement
Feed Flow (m3/hr)	0.83	0.506	0.414
Permeate Flow (m3/hr)	0.083	0.136	0.166
Recovery (%)	10	16.4	20.05

The data proposed that the product output from the system should be free of any traces of sodium chloride or other minor saline elements. With the ideal salt rejection factor of the membrane being 99.4%, this is not a realistic target nor is it possible with this model of membrane. According to the Western Australian Department of Health, potable water can contain traces of NaCl of up to 180mg/L (180ppm) for taste based on an aesthetic guideline level from the ADWG. It was expected for this simulation, the product water would be suitable for uses equivalent to recycled water and not for consumption. The expected return of permeate concentration for salt water RO processes with a feed water concentration in excess of 32,000mg/L is no greater than 500mg/L. With this the accepted industry norm outlined by Hoang et. al. [5], results of less than 500ppm will be acceptable and deemed accurate.

2.3 Simulation Techniques and Assumptions

Aspen Plus software offers the user a number of existing libraries containing product blocks with defined settings ranging from pumps and centrifuges to filters, splitters and evaporators. The program also allows the options to customize a user defined unit operation block which specifies a process that isn't captured or can be modelled using the items within the existing libraries. To simulate the RO membrane, a process that selectively separates the feed stream into two streams based on the membrane characteristics needed to be selected. With the RO membrane acting as a combination of blocks such as filters and splitters, the option of using defined blocks was deemed inaccurate and unsuitable, meaning a customized unit operation block was needed to model the membrane. Using the user block option in the Aspen Plus library, the Hydranautics SWC-2540 membrane was created and simulated in single, double and triple series arrangements before being validated and sequentially optimized. Throughout the development, simulation and validation of the Aspen Plus model, there were a number of assumptions that were made which are listed below.

- The effect of scale build up, system purity and prime running conditions have negligible effects on the design and effectiveness of the membrane.

- The properties of the feed water remain constant during the treatment meaning, the TDS level does not alter along with temperature, level of suspended solids and additional pre-treatment requirements due to unforeseen contaminants or a change in outside conditions.

- Due to the model being validated against the existing theoretical result, an assumption was made that appropriate measures were taken during the study to ensure that the results collected are accurate and correct. In the event that the results were considered unrealistic such as the saline concentration in the product streams, realistic limits and boundaries were set to ensure accurate validation.

- Material degradation during the life of the simulated system was negligible and did not affect the outcome of the simulations.

- Membrane elements and specifications were all taken at a maximum during input calculations and when determining performance characteristics of the model.

3. Modelling and Simulation Results and Discussion

In order to develop a validated model against the design data, the Aspen Plus model adopted the single to triple membrane series arrangement progression. The model was tested as each membrane was added to the system to ensure validation of the simulation was achieved. Figure 3 outline the model as it is developed from a single membrane to the triple membrane series arrangement validated and used in the optimizations process. For means of validation, the primary results returned from the simulations were those comparable to the validation data including permeate flow rate and system recovery percentage. Although the product concentration of the validation data was neglected, this aspect of the permeate was monitored throughout the simulations to ensure it remained below 500ppm as expected according to Hoang et. al. [5]. Other properties of the system were also checked throughout modelling for any adverse or unexpected results that could have inhibited validation of the simulation. The final simulations for each arrangement were all completed 'normally' and without errors.

3.1 Model Validation

The validation process was carried out progressively as the model was developed from a single membrane system to the three membrane series arrangement to ensure the model obtained and maintained accuracy until the final model was established. The flow rate which corresponds directly to the system recovery along with the boundary limits of permeate concentration were the properties used to determine and establish a validated model. In order to determine the validity of each model progression, the percentage difference was found for these characteristics with the maximum allowable variation set to 2%. Table 6 shows a summary of the simulated result, the validation data and the variation between the two sets of data.
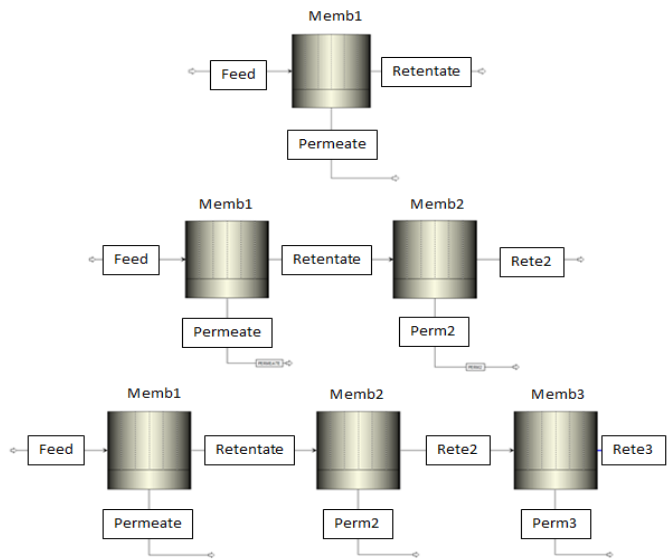

Figure 3: Membrane series model development schematic

The small inaccuracies that were recorded can be assumed to have originated from the differences in the allowable concentrate levels in the simulated and validation permeates. With a maximum of 466ppm difference in this level, the membrane flow characteristics that were calculated in the validation data would have been modelled to an unrealistic level, generating performance characteristics such as salt rejection coefficients beyond the capacity of the SWC-2540 membrane. Although errors were apparent in the simulations, the developed model coincides with the validation data within the accepted error limits of 2% and less than 500ppm TDS concentration. With this the case, the model is deemed as valid and optimization investigations can be carried out.

Table 6: Validation Data and Variation Percentages

Arrangement	Simulation Permeate Flow Rate (L/hr)	Validation Permeate Flow Rate (L/hr)	Difference (%)	Maximum Permeate Concentration (ppm)
Single	83.16	83	0.19	292
Double	136.09	136	0.07	399
Triple	166.01	166	0.01	466

2.2 Model Optimization

The optimization process adopted a structured form which altered each feed characteristic of the triple membrane arrangement one at a time within suitable limits. Results were recorded after each simulation which focused predominantly on the flow rate and concentration of the permeate stream and the concentration and pressure of the brine waste. The optimum settings for each parameter are recognized and discussed with regard to possible implementation and the effectiveness of altering the system. For comparison and discussion purposes, the recorded data was graphed and is shown in the preceding discussion.

Temperature: The feed input values used for the temperature optimization simulations were as per the triple arrangement validation simulation with the exception of the variable temperature property. The temperature ranged between 10 oC and 40 oC at increments of 1 oC and small linear improvements were seen as temperature dropped

Author name / Procedia Engineering 00 (2015) 000–000

below the initial simulation temperature of 25 °C. No changes were seen in product concentration or pressure drop across the membrane modules. Figure 4 gives an indication of the total product flow from the system as a variable feed temperature is introduced. As can be seen from the plot, the system returns small increases as the temperature decreases. Figure 5 gives a graphical display of the percentage improvements due to the alteration of the feed water temperature. As shown, the maximum increase in total permeate flow is approximately 0.4%. When comparing these results to those found in literature it is difficult to determine whether they are accurate as most major established plants and other experimental test rigs operate with feed water temperatures of approximately 25 oC, [10] resulting in no wasted energy through preheating or cooling the feed stream. An example of this is the SWRO plant in Qatar which operates at 25 oC producing 223.2 cubic meters of permeates daily between 500 and 1000ppm from a feed of 58,000ppm concentration [11]. Although a number of larger plants operate at the standard temperature of 25 oC, a year round study conducted in Tunisia [12] using a small scale domestic RO system found that higher feed water temperatures in the summer months resulted in up to 8% higher recovery rates for the small system. In saying this, it should be noted that the feed water in this study was supplied from natural sources and subject to limited pre-treatment (chemical free filtering for suspended solids) in which the salinity of the feed varied depending on the climatic conditions. pH levels also varied due to these conditions while Figures 4 and 5 assume constant feed properties.
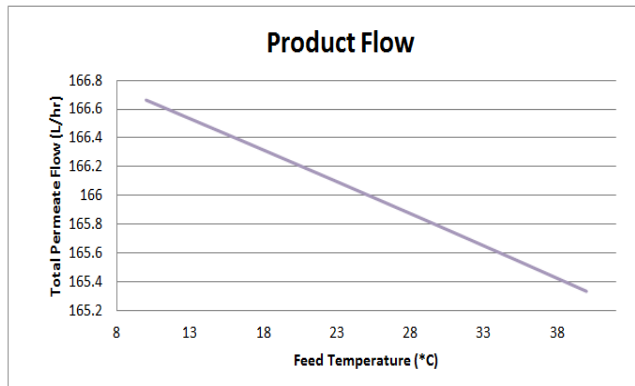

Figure 4: Total product flow against variable feed water temperature.
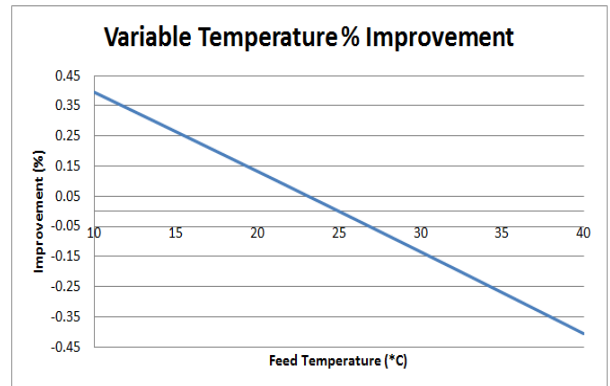

Figure 5: Percentage improvement for variable feed water temperature.

Pressure: Temperature of the feed water was returned to 25 °C for the pressure optimisation investigation with the flow rate remaining at the original 0.414 m³/hr. The feed pressure was varied from 30 bar to 80 bar which in fact exceeds manufacturer's recommended maximum operating pressure by 14%. From the simulations it was found that the total product flow remained constant, along with the individual product stream concentrations which were seen to stay within the set boundary of 500ppm. This can be seen in Figure 6. Although the constant product stream concentrations were simulated beyond the maximum operating pressures outlined by the manufacturer, the output data shown in Figure 6 correspond to those shown in RO plants such as the Sharjah BWRO plant in United Arab Emirates where the concentration of each RO module remains constant in each arrangement pass as they are subjected to variable pressures [11]. The increase in feed pressure saw a directly proportional rise in the pressure of each brine steam, although the pressure drop in the membrane modules remained unchanged. This again resembles current plants in operation regardless of size or output capacity including Sharjah and Qatar [11] as there is a limited maximum pressure drop across each membrane during operation. With the increase in the brine pressure, an opportunity for the addition of multiple ERD's to the system is presented. Although the initial system requirements have been met, the initial power generated from the ERD devices can contribute to the funding of additional membranes to further increase the system efficiency and output. The brine stream pressures plotted in Figure 7 show

the relationship between the increased feed pressure and the corresponding retentate pressure output. The feed pressure would only be able to increase to 6.9MPa due to maximum pressure limits specified by the manufacturer.
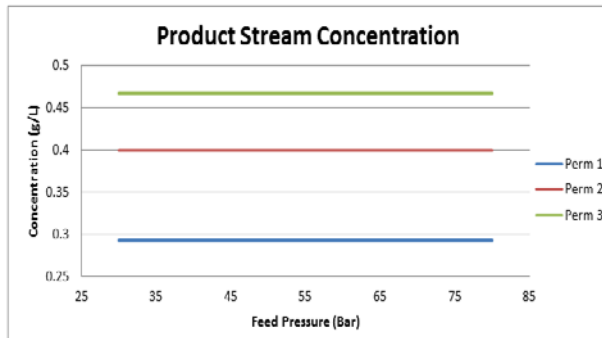

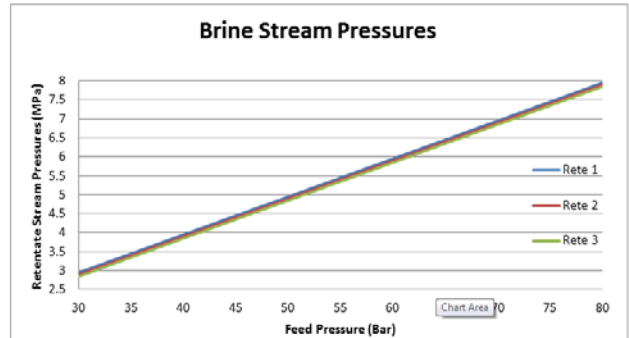**Figure 6:** Product stream concentration with variable feed pressure

Figure 7: Brine stream pressure increase with variable feed pressure

*Feed Concentration :*As expected, the alteration of feed concentration had immediate and substantial impacts to the product flow and concentration of the retentate streams as shown in Figure 8. With temperature, pressure and feed flow established at 25 oC, 34.474 bar and 0.414 m3/hr, the product flow increased almost linearly as the feed concentration was decreased. As feed flow remains constant, a diluted feed diffuses more readily through the membrane as it has a constant salt rejection factor. Studies by both Majali et al. [11] and Elfil et al. [12] report that both large scale and small scale plants exhibit behaviors like those shown in Figure 8 where increased feed concentrations inhibit product flow levels. These reports and the relationship plotted in Figure 8 reflect the maximum membrane salt rejection properties which are outlined by the Hydranautics as being 99.4% for the SWC-2540 membrane used in the simulations. As the concentration of the feed water increases, the permeate flow reduces as the diffusion process through the first membrane under constant pressure is lengthened. Figure 9 shows this relationship graphically as the three permeate streams are plotted against the changing feed concentration.

As seen in Figure 9, the flow through the first and second membranes is up to 71.7% and 25.4% greater respectively, than those seen in the triple arrangement validation simulation. Once the stream passes through the third membrane, the flow rate returns almost to the initial flow rates as the salt concentration has again increased after the first two passes. Although increased flow rates are seen as a result of this investigation, it must be noted that the initial feed concentration of 35g/L was used to replicate the coastal water conditions of Central Queensland and specifically Yeppoon. Unless brackish water supplies of lower concentrations are to be used in the system, further pre-treatment is needed in order to alter the feed concentration conditions to replicate those in the above simulation.

*Feed Flow :*The variable feed flow optimizations simulation resulted in product flow data returns almost linearly proportional to the increase in the feed flow. With feed temperature and pressure at 25 oC and 34.474 bar respectively, the feed flow was altered from 0.05 m3/hr to 1.5 m3/hr in increments of 0.05 m3/hr. Permeate concentrates remained below the 500ppm limit for all flow rates which was expected as the feed concentration was again set to 35,000mg/L. Figure 10 shows the total product flow as the feed flow increments rose. As anticipated, the product flow increased as the system was subjected to a rising feed rate and exhibits behavior that reflects data found in a study by Majali et al [11] on both the Sharjah and Qatar RO plants. Figure 11 outlines the relationship found in this study between the feed and product flows at the Qatar SWRO plant which operates at a daily capacity of 223.5 m^3.
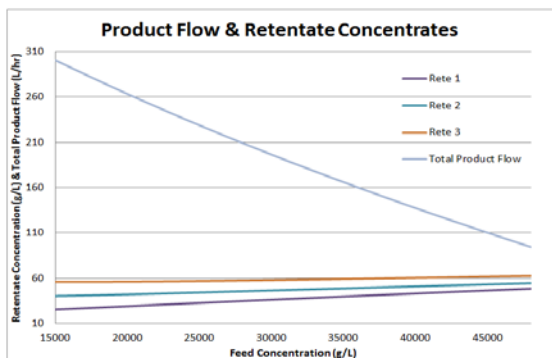
Figure 8: Product flow and retentate concentrates subject to variable feed concentration.
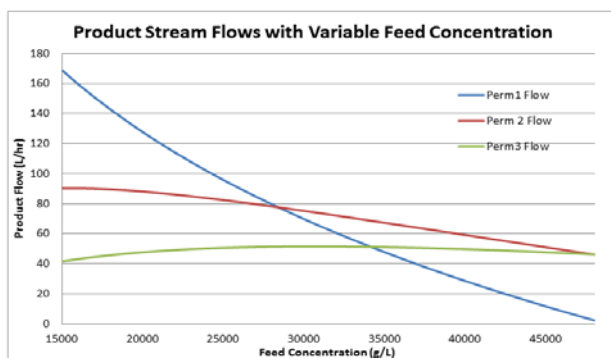

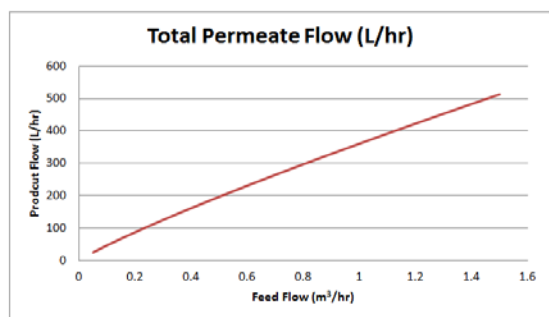**Figure 9:** Product stream flows with variable feed concentration.

Figure 10: Total product flow with increasing feed flow.
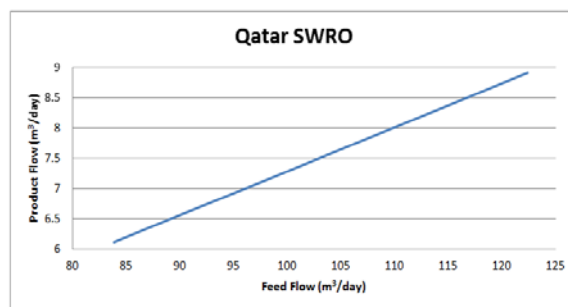

Figure 11: Feed & Product Flow relationship of the Qatar SWRO Plant (Majali et al. 2008).

Although Figure 12 suggests a relatively simple relationship between the two sets of data, an investigation into the water conversion factor (WCF) of the simulations, which relates to the system recovery, shows that at smaller flow rates, the system operates at greater efficiencies. Over the range of feed flows simulated, an increase in system efficiency of almost 15% can be seen. This efficiency relationship is plotted below in Figure 12. Comparison between Figures 10 and 12 present opportunities for a user to select the most efficient feed flow depending on the desired output of the system. Using the case of the validation data where 0.5 m3/day was required from a 6 hour operational day, the most efficient system feed can be found to be 0.109 m3/hr using the optimization data and a linear approximation through interpolation. The calculation of the most efficient and appreciate system arrangement also applies the assumption that the feed temperature and pressure remain constant at the values the optimization data was evaluated. In comparison to the other feed water characteristics of temperature, pressure and concentration, the feed flow is a variable that can be altered at no additional costs or variation to the system. This ensures the small scale solar desalination arrangement operates at the most efficient level whilst still providing the minimum desired output promoting longevity of the system components and most importantly the membranes.

4. Conclusions

The primary purpose of this study saw the development of a computational model to simulate and sequentially optimize the performance of a small scale solar desalination plant as a function of operating variables using Aspen

Plus software. As a part of the project, an investigation into desalination indicated that solar RO desalination systems provide a sustainable solution to the increasing scarcity of fresh water sources especially in Australia where saltwater is an abundant resource. In comparison with a set of validation data, the simulated model was validated before optimizations simulation took place in order to improve current outputs.

Once the system was verified, optimization of the functional parameters was investigated providing results that both aligned with literature studies and current practice in operating RO plants around the world giving further evidence of system verification. Based on the results of the optimization phase, the impact of variable feed water characteristics were discussed, analyzed and compared, with feed flow concluded as the most cost effective and easily altered property for the small scale simulated system. By using the optimization results and the water conversion factor plot, the most efficient system can be obtained while desired outputs are still met.
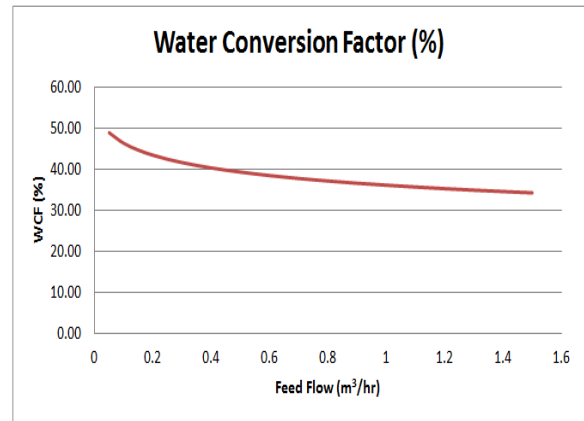

Figure 12: Water Conversion Factor for Variable Feed Flow Simulations.

Although it was found that additional changes to temperature, pressure or concentration of the feed-water can results in system improvements, feed flow was seen to be only variable that provides a seemingly cost free and instant improvement in system efficiency of up to 15%. Along with this enhancement it was also noted that the concentration of the permeate remained below the 500ppm limit meaning the product permeate remained within the potable range. Additionally, the variation of the feed flow provides the option to alter the desired output based on the level of potential solar energy each day.

5. References

[1] Buros, OK 1990, The ABC's of Desalting, International Desalination Association, Massachusetts 'Case History: Tapping the Oceans' 2008, The Economist – Technology Quarterly, viewed 23 October 2013, http://www.economist.com/node/11484059.

[2] Schrader, JR and Rasul, MG 2008, Design and Simulation of a Small Scale Solar Powered Desalination System, CD-ROM, Proceedings of the 3rd IASME and WSEAS International Conference on Energy & Environment, Paper Number: 575-295, Page 457-462, 23-25 February 2008, Cambridge, UK.

[3] Rasul, MG, Covey, DW & Khan MMK 2006, 'Solar Assisted Desalination Technology', paper presented to the International Conference & Exhibition on Sustainable Energy Development, New Delhi, February

[4] Planning Institute of Australia (PIA) 2003, Water and Planning, viewed 30 November 2013, http://www.planning.org.au/policy/water-and-planning.

[5] Hoang, M, Bolto, B, Haskard, C, Barron, O, Gray, S, Leslie, G 2009, Desalination in Australia, and Water for a Healthy Country Flagship Report series ISSN: 1835-095X, CSIRO, Clayton

[6] Horticulture Australia Limited 2005, Rewater – Farming with Recycled Water, brochure, Horticulture Australia Limited, Australia

[7] Leslie, G 2004 Desalination: Its place in meeting our fresh water needs, Presentation to Institute of Energy Australia, 15 November 2004.

[8] Aspentech 2013, Optimize Chemical Processes with Aspen Plus, viewed 4 November 2013, http://www.aspentech.com/products/aspen-plus.aspx

[9] Hydranautics 2013, Membrane Element, Nitto Group, Oceanside.

[10] Laborde, H.M, Franca, K.B, Neff, H, Lima, A.M.N 2001, 'Optimization Strategy for a small-scale reverse osmosis water desalination system based on solar energy', Desalination, vol. 133, no. 1, pp. 1-12

[11] Majali, F, Ettouney, H, Abdel-Jabbar, N & Qiblawey, H 2008, 'Design and operating characteristics of pilot scale reverse osmosis plants', Desalination, vol. 222, no. 1, pp.441-450.

[12] Elfil, H, Hamed, A, Hannachi, A 2007, 'Technical evaluation of a small-scale reverse osmosis desalination unit for domestic water', Desalination, vol. 203, no. 1, pp. 319-326.

6th BSME International Conference on Thermal Engineering (ICTE 2014)

Interactions between liquid-water and gas-diffusion layers in polymer-electrolyte fuel cells

Prodip K. Das[a,*], Anthony D. Santamaria[b], Adam Z. Weber[c]

[a]*School of Mechanical and Systems Engineering, Newcastle University, Newcastle upon Tyne, NE1 7RU, United Kingdom*
[b]*Department of Mechanical Engineering, Western New England University, Springfield, MA 01119, USA*
[c]*Environmental Energy Technologies Division, Lawrence Berkeley National Laboratory, Berkeley, CA 94720, USA*

Abstract

Over the past few decades, a significant amount of research on polymer-electrolyte fuel cells (PEFCs) has been conducted to improve performance and durability while reducing the cost of fuel cell systems. However, the cost associated with the platinum (Pt) catalyst remains a barrier to their commercialization and PEFC durability standards have yet to be established. An effective path toward reducing PEFC cost is making the catalyst layers (CLs) thinner thus reducing expensive Pt content. The limit of thin CLs is high gas-transport resistance and the performance of these CLs is sensitive to the operating temperature due to their inherent low water uptake capacity, which results in higher sensitivity to liquid-water flooding and reduced durability. Therefore, reducing PEFC's cost by decreasing Pt content and improving PEFC's performance and durability by managing liquid-water are still challenging and open topics of research. An overlooked aspect nowadays of PEFC water management is the gas-diffusion layer (GDL). While it is known that GDL's properties can impact performance, typically it is not seen as a critical component. In this work, we present data showing the importance of GDLs in terms of water removal and management while also exploring the interactions between liquid-water and GDL surfaces. The critical interface of GDL and gas-flow-channel in the presence of liquid-water was examined through systematic studies of adhesion forces as a function of water-injection rate for various GDLs of varying thickness. GDL properties (breakthrough pressure and adhesion force) were measured experimentally under a host of test conditions. Specifically, the effects of GDL hydrophobic (PTFE) content, thickness, and water-injection rate were examined to identify trends that may be beneficial to the design of liquid-water management strategies and next-generation GDL materials for PEFCs.

© 2015 The Authors. Published by Elsevier Ltd.
Peer-review under responsibility of organizing committee of the 6th BSME International Conference on Thermal Engineering (ICTE 2014).

Keywords: Polymer-electrolyte fuel cells; Liquid-water; Water-management; Gas-diffusion layers

* Corresponding author. Tel.: +44-191-208-6170 ; fax: +44-191-208-8600
 E-mail address: prodip.das@ncl.ac.uk

1. Introduction

Polymer-electrolyte fuel cell (PEFC) systems are extremely efficient over a wide scale ranging from 1 kW to hundreds of megawatts and some systems can achieve overall efficiencies of 80% or more when heat production is combined with power generation. They are becoming the center of attention as an alternative power source for vehicle and stationary applications due to their ability to produce high power densities under rapid load changes. Although a substantial amount of resources has been devoted over the past several decades to the development of PEFC systems, they are not yet commercially viable due to several technical barriers. Of the many barriers, cost and durability present two of the most significant challenges to achieving reliable, cost-effective PEFC systems. In addition, PEFC performance must meet or exceed that of competing technologies. Therefore, sought after methods to reduce PEFC's cost include: i) reducing expensive Pt loading while maintaining performance ii) improving performance and durability by advanced liquid-water management schemes [1-3].

The United States Department of Energy (DOE) has a target to develop a direct-hydrogen fuel-cell power system for transportation at a cost of \$30/kW by 2017. Paralleling this goal, the DOE's current targeted platinum usage in PEFCs is 0.125 mg/cm^2 (in combined anode and cathode electrodes) or less, while producing rated stack power densities of 8.0 kW/g$_{Pt}$. To achieve the DOE's target, a key solution is the design and use of thin catalyst layers (CLs). The limiting factor in thin CL design is believed to be high gas-transport resistance due to the ionomer film covering the catalyst particles as well as issues of tolerance to poisoning [4]. In addition, the performance of thin CLs is sensitive to operating temperatures due to their inherent low water capacity, as the thickness of a CL is often in the range of few microns [3]. At low temperatures, they are prone to severe water flooding, which is problematic since the low-temperature operation is vital for rapid startup and attaining relatively high current densities. Therefore, water management is an especially critical component for PEFC operation with thin CLs, especially at low operating temperatures and during startup/shutdown, where liquid water is present. A balanced liquid-water scheme is therefore essential to achieve the full potential of a thin CL PEFC and to avoid membrane dehydration and porous-media flooding.

A critical issue for optimal water management in PEFCs at lower temperatures is the removal of liquid water from the membrane electrode assembly (MEA). This pathway is intimately linked with the phenomena of water transport (in either gas or liquid phase) and liquid-water droplet removal from surface of the gas-diffusion layer and into the flow channel. Therefore, understanding multiphase, dynamic GDL water uptake and removal is essential to developing effective liquid-water management strategies as well as next-generation GDL materials. To understand the dynamics of GDL and liquid-water interactions, we employed a novel rotating-stage goniometer to quantify and directly measure the sliding angles, adhesion force, and breakthrough pressure for various GDLs. Results of these measurements are presented and analyzed with the aim of finding an optimum pathway for liquid-water removal and designing next-generation GDL materials for PEFCs.

2. Experimental

2.1. Adhesion force

The adhesion force represents the resistance force that a droplet needs to overcome to initiate motion along a surface, which can be correlated with the sliding and contact angles of a droplet by a gravity field [5]. The contact and sliding angle measurements were done with a custom-made automated rotating-stage goniometer (ramé-hart Model 590) as shown in Fig. 1a. The system utilized a CCD camera (70 fps) of 640 × 480 pixels to capture images every quarter second, with two 150 W halogen lamps used as a backlight. The GDL sample was first placed on the sample-stage and then liquid-water was injected from either above the sample by a needle or the bottom of the sample using an automated dispensing system. The camera was mounted to a stage that was inclined by a rotary motor at a constant angular speed. The rotary motor can operate as low as 0.1°/s. Movement of the stage was vibration-free with no backlash and vibrations from surroundings were isolated from the stage using an anti-

vibration stage to ensure that the liquid-water droplet releases only due to gravity. Several measurements of contact and sliding angles were taken for each sample, while three contact-angle measurements were taken for each droplet within 1 second using DROPimage® software.
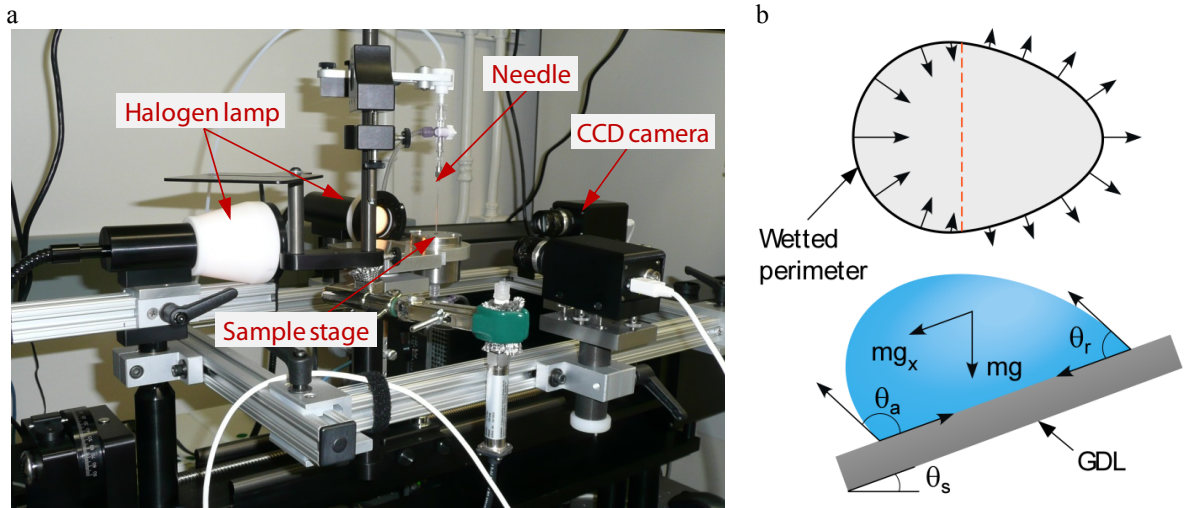

Fig. 1. (a) Rotating-stage goniometer setup used for breakthrough-pressure and adhesion-force measurements. (b) Illustration of contact and sliding angles and forces acting on a liquid-water droplet on a gas-diffusion layer (GDL) surface. Top view of part (b) shows the adhesion force distribution that is preventing the droplet from roll-off (parallel to the GDL surface); dashed line shows contact angle transition through 90°.

As shown in Fig. 1b, at the incipient sliding angle, the adhesion force and the gravity force acting on the liquid-water droplet equal each other. Thus, we can calculate the adhesion force between the liquid-water droplet and GDL surface from the body force acting along the direction of the slide and the wetted diameter,

$$F_{\text{adhesion}} = \frac{\rho V g \sin \theta_s}{\pi d_w} \tag{1}$$

where ρ is the water density, V is the droplet volume, g is the gravitational acceleration constant, θ_s is the sliding angle, and d_w is the wetted diameter. The wetted diameter represents the equivalent diameter of the wetted area between the droplet and GDL surface as shown in Fig. 1b.

2.2. Breakthrough pressure

Breakthrough pressure is a characteristic parameter for porous material, such as fuel cell GDLs. It is related to the capillary pressure inside the pore and is determined predominately by the pore structure and the contact angle between a liquid droplet and the GDL. The Young-Laplace equation defines capillary pressure, P_c, as

$$P_c = P_L - P_G = \frac{2\gamma \cos \theta}{r} \tag{2}$$

where θ is the contact angle between water/air and GDL pore, r is the radius of a pore, P_L is the liquid-phase pressure, and P_G is the gas-phase pressure [6]. Water invasion into a hydrophobic GDL usually follows a path whereby pores with larger connecting throat radii are filled first. Breakthrough pressure, P_{BT}, refers to the maximum capillary pressure (usually a result of the minimum throat radii) that must be overcome by the reservoir pressure before flow out of a GDL can occur.

Gas-diffusion layers (GDLs) are typically treated with PTFE to increase hydrophobicity and enhance water-removal capability (see scanning-electron-microscope images in Fig. 2). These coatings can affect the GDL pore volumes and throat radii influencing the breakthrough pressure, especially as the coatings are known to be non-uniform. To measure breakthrough pressure, GDL samples were held in place on the injection port plate using 3M double-sided tape. An Omega PX603 series pressure transducer was used to measure pressure at a sampling rate of 10 Hz. Injection rates were controlled digitally using an automated dispensing system, which was routinely monitored for and purged of air bubbles to ensure consistent results. Breakthrough pressure was determined by examining the maximum pressure achieved during an injection period. An example of typical capillary pressure data recorded over a period of time is shown in Fig. 2c. Analyzing Fig. 2c, the initial pressure signal is due to the head from water traveling through system lines (defined as system pressure or P_{sys}) and filling void space between the GDL and injection port and then a steep climb begins due to water being forced into GDL pores. The slope of the curve is attributable to expansion of the injection system before reaching a maximum, which is accompanied by droplet formation on the GDL surface. This maximum pressure is breakthrough pressure (P_{BT}) followed by a dramatic fall in signal as the pressure decays to a minimum due to reduced resistance.
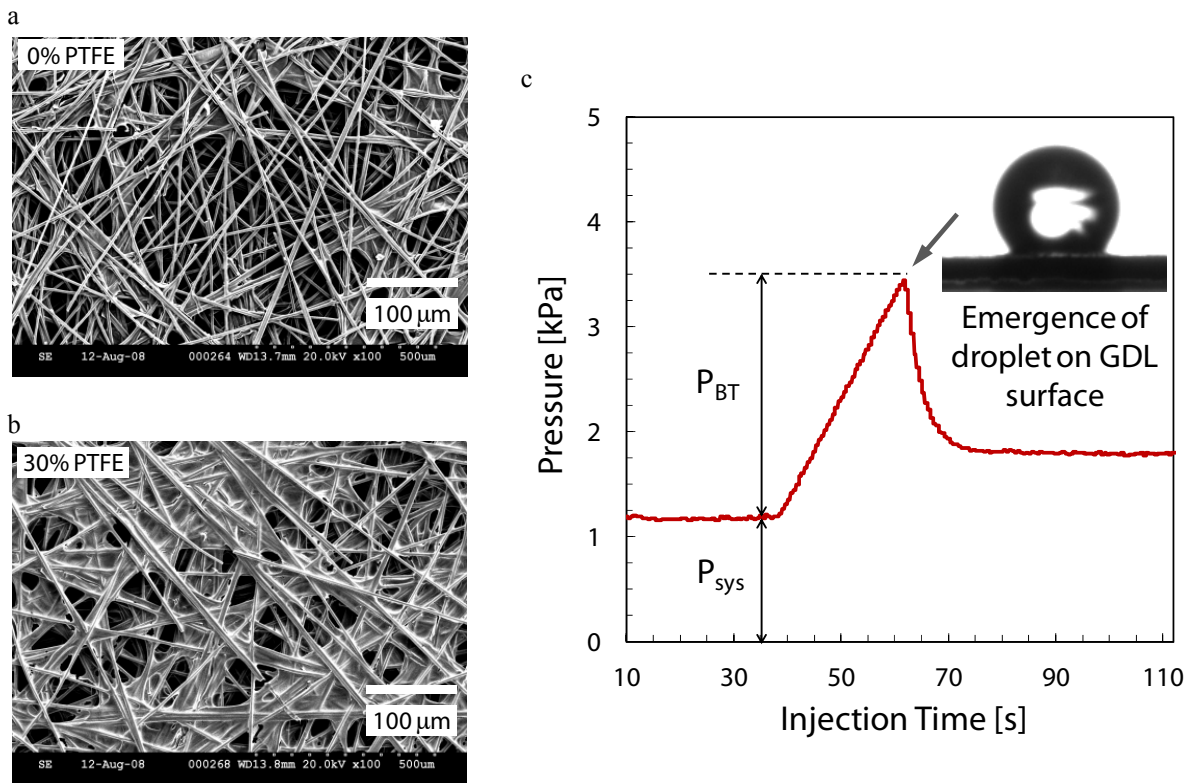

Fig. 2. Scanning-electron-microscope (SEM) images of PEFC gas-diffusion layers showing surface inhomogeneity both without (a) and with (b) PTFE treatment. (c) Time-series data acquired for capillary breakthrough pressure (P_{BT}) measurements, where the maximum capillary pressure represents the breakthrough pressure as droplet forms.

3. Results and Discussions

The interactions between the liquid-water and GDL surface are analyzed through the evaporation of a droplet on GDL surface. The adhesion force between the liquid-water droplet and GDL surface is determined from sliding angle data using Eq. (1). Fig. 3a shows the evaporation of a water droplet on untreated and PTFE treated (20-wt% PTFE loading) GDLs and Fig. 3b shows the effect of water injection rate on adhesion force. The 'pinning' effect is

found to be significant for the bottom injection, which assists the droplet adhesion with the GDL surface, whereas both the 'pinning' and 'dewetting' phenomena are present for a droplet placed on top of a GDL surface using the top injection. Here the pinning represents the scenario when the solid-liquid contact line remains pinned to the GDL surface while the liquid-gas interface shrinks, and the dewetting represents the scenario when the solid-liquid contact line shrinks with the liquid-gas interface.

As observed in Fig. 3a, the change of static contact angle is non-uniform. It initially decreases due to evaporation, and it increases and then again decreases as the droplet size decreases due to evaporation. Here, the adhesion between the droplet and GDL surface changes with the droplet size, which influences the static contact angle. Clearly, the adhesion force dominates over the tension force that prevents the liquid-water droplet from contracting along the wetting line (for times less than 160 s). In other words, the pinning effect is dominant over the dewetting effect. With the decrease of droplet size, the cohesion force eventually helps the droplet to contract, and the droplet exhibits the initial surface wettability again that is indicated between 150 s and 400 s. As droplet size further decreases, the adhesion force eventually regains its dominance, and the pinning effect is again observed after 400 s.

The injection rate is analogous to the operating current density in an operating PEFC. In fact, an injection rate of 1 µL/s corresponds to a water flux derived from a current density of 2.5 A/cm^2 assuming a net water transport coefficient of 0.5 in the membrane of PEFC. The effect of injection rate on the adhesion force is shown for a PTFE treated GDL. As observed in Fig. 3b, the adhesion between the water droplet and GDL surface decreases with injection rate. In other words, faster injection enhances droplet detachment from the GDL surface. Although not shown, the static contact angle decreases with the injection rate, which results in the opposite trend in terms of adhesion force and demonstrates the efficacy of contact angles [5].
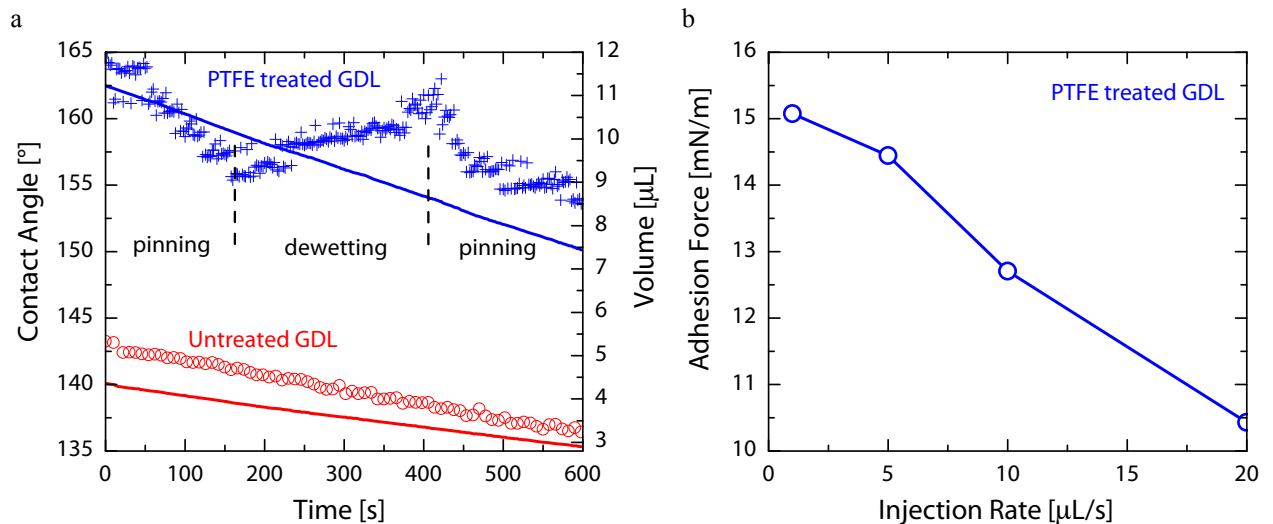

Fig. 3. (a) Interactions between water-droplet and GDL surface are shown through the contraction of the droplet due to the evaporation after 10 min and the pinning-dewetting phenomena. This figure shows the measured droplet volume (solid line) and static contact angle (symbols) as functions of time for PTFE treated and untreated GDLs. (b) Effect of injection rate on adhesion force for PTFE treated GDL [5].

Fig. 4 shows the results of breakthrough pressure as a function of GDL thickness. A higher breakthrough pressure is observed as increased GDL thickness, which implies longer flow pathways and an increased number of pores liquid water must fill before reaching the surface. This result demonstrates reduced breakthrough pressure at lower PTFE weights and an increasing rather than logarithmically plateauing trend at higher loadings. The higher breakthrough pressure at elevated PTFE loadings is due to the heterogeneous distribution of PTFE, as shown in SEM images in Fig. 2, that reduces the number of pores available to water invasion. This result matches with the

idealized view of PTFE loading effectively reducing throat sizes of the porous GDL and increasing contact angle especially at high PTFE content [7].
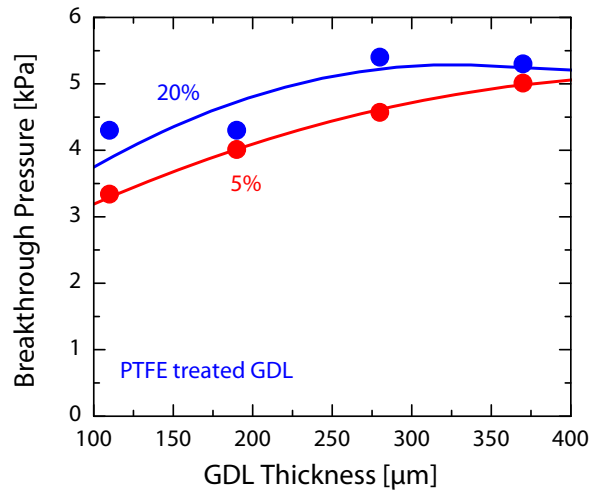

Fig. 4. Breakthrough pressure as a function of GDL thickness for 5% and 20% PTFE loadings [7].

4. Conclusions

The interactions between liquid-water and GDL surface were studied using adhesion force and breakthrough pressure measurements. It has been shown that the direct measurement of sliding angles and adhesion forces is an effective method to accurately predict droplet instability and detachment on and from the GDL surface. It has been observed that both the droplet creation method is important for droplet growth and detachment on a GDL surface. The impact of injection rate showed that higher flow rates results in lower adhesion forces, perhaps due to the kinetic effects and different water-transport pathways. Breakthrough pressure measurements showed that increasing PTFE content and GDL thickness both resulted in higher breakthrough pressure, which highlights the strong dependence of breakthrough pressure on a GDL's porosity and contact angle.

Acknowledgements

References

[1] P.K. Das, X. Li, Z.S. Liu, Analytical approach to polymer electrolyte membrane fuel cell performance and optimization" J. Electroanal. Chem., 604 (2007) 72–90.
[2] P.K. Das, X. Li, Z.S. Liu, Analysis of liquid water transport in cathode catalyst layer of PEM fuel cells, Int. J. Hydrogen. Energ., 35 (2010) 2403–2416.
[3] P.K. Das, A.Z. Weber, Water management in PEMFC with ultra-thin catalyst-layers, Proc. of ASME 11th Fuel Cell Science, Engineering and Technology Conference, Minneapolis, 2013, pp. 1–10.
[4] W. Yoon, A.Z. Weber, Modeling low-platinum-loading effects in fuel-cell catalyst layers, J. Electrochem. Soc., 158 (2011) B1007–B1018.
[5] P.K. Das, A. Grippin, A. Kwong, A.Z. Weber, Liquid water-droplet adhesion-force measurements on fresh and aged fuel-cell gas-diffusion layers, J. Electrochem. Soc. 159 (2012) B489–B496.
[6] H.J. Butt, K. Graf, M. Kapp, Physics and Chemistry of Interfaces, Wiley-VCH, Weinheim, 2006.
[7] A. Santamaria, P.K. Das, J. MacDonald, A.Z. Weber, Liquid-water interactions with gas-diffusion layers surfaces, J. Electrochem. Soc. 161 (2014) F1184–F1193.

6th BSME International Conference on Thermal Engineering (ICTE 2014)

An aerodynamic study of a domestic scale horizontal axis wind turbine with varied tip configurations

Abdulkadir Ali, Harun Chowdhury*, Bavin Loganathan and Firoz Alam

School of Aerospace, Mechanical and Manufacturing Engineering, RMIT University, Melbourne, 3083, Australia

Abstract

This paper primarily aims to investigate the aerodynamic characteristics of a small Horizontal Axis Wind Turbines (HAWT) with different blade tip configurations to enhance power generation efficiency. To understand the flow behavior at the tip and to reduce the induced drag due to tip vortex, three different blade configurations (upwind winglet, downwind winglet and blade without a winglet) were designed, manufactured and tested under a range of wind speeds and yaw angles. The results show that the winglet has significant effect on the aerodynamic performance of the wind turbine blade used for domestic scale wind generator. The results indicated an increase of lift-to-drag ratio with the upwind winglet by around 26% compared to a straight blade with no winglet whereas the downwind winglet results in a decrease of lift-to-drag ratio about 27%.

Keywords: horizontal axis wind turbine; winglets; wind tunnel; aerodynamic loads.

1. Introduction

   Wind energy is considered to be among the most viable and an alternative source of energy to current fossil fuel based energy due to the abundant available resource of wind and has little contribution in the pollution of carbon

   * Corresponding author. Tel.: +61 3 99256103; fax: +61 3 99256108.
     E-mail address: harun.chowdhury@rmit.edu.au

dioxide into the atmosphere. Continued increase in fossil fuel prices coupled with global warming has led to many of the developed nations to act swiftly in order to minimize the pollution of greenhouse gases in to the atmosphere by agreeing to a renewable energy target of 20 percent in the year of 2020 [1]. Over the past two decades, the rapid advancements in technology in particular the aerodynamics design of commercial horizontal axis wind turbine (HAWT) blades, significant improvements have been achieved in the wind turbines ability to extract far greater kinetic energy from the wind. Currently, commercial wind turbines are capable of producing power outputs of up to 6 MW [2]. In contrast to commercial wind turbines, domestic scale horizontal axis wind turbines have not advanced at the same rate as commercial wind turbines due to many factors such as low efficiency, space constraint as well as high capital cost.

Domestic scale horizontal axis wind turbines have the potential to be utilized and integrated into residential urban environments. Due to the presence of buildings and surrounding trees, the wind flow is obstructed and as a result turbulence is generated in the flow which significantly reduces the mean wind speed. In order to maximize the power generation capabilities of small wind turbines, it is essential to consider the environment under which the wind turbines are expected to operate. One of the most important aspects of wind turbines that heavily influence the efficiency of the turbines is the aerodynamic shape of the blades. The geometrical shape of the turbine blades are defined by airfoils that are based on their lift coefficient characteristic and are stationed at different sectional radius of the blade. An ideal wind turbine that is aerodynamically efficient cannot extract more than 59.3 percent of the winds kinetic energy as found by Albert Betz using a simple one dimensional model [3]. Although recent advancements in aerodynamic blade design has significantly enhanced the efficiency of wind turbine blades, there are still aerodynamic losses that a blade experiences which continue to dampen the efficiency of wind turbines. One of these losses is associated with the blade tip vortices. Blade tip vortices are generated as a result of the pressure difference between the suction side (low pressure and high velocity) and pressure side (high pressure and low velocity). This pressure difference causes the high pressure flow of air to intermix with the low pressure flow of air at the blade tip and produces vortices at the tip region of blade. The vortices which are produced induce drag on the blade that reduces the efficiency of the wind turbine blades as well causing undesirable noise.

In order to understand the effects of various tip configurations, it is essential to determine the aerodynamic forces such as drag and lift that are subjected on the blades. Several studies have been conducted to investigate the effects of alternative blade tip designs for minimizing the vortices and ultimately reducing the induce drag. The majority of these studies have being investigated using numerical modeling techniques such as Computational Fluid Dynamics (CFD) and other numerical codes that are based on Blade Element Momentum (BEM) theory [4-5]. Very limited research is available in the public domain which experimentally investigates, through wind tunnel testing, the aerodynamic characteristics of wind turbine blades. Therefore the primary objective of this research is to experimentally investigate the aerodynamics effects of alternative blade tip configurations (winglets) that could potentially enhance the performance of wind turbines.

Nomenclature

ψ	yaw angle
L	lift force (N)
D	drag force (N)
C_D	drag coefficient
C_L	lift coefficient
ρ	density of air (kg/m^3)
V	wind speed (m/s)
A	projected frontal area of the turbine blade (m^2)

2. Experimental method

2.1. Wind turbine blade design

The geometrical shapes of wind turbine blades are generally defined by airfoils which are carefully stationed and arranged through the entire radius of the blade. The blades are designed using the SG6051 airfoil, which is specifically designed for small wind turbines and is selected in the design process due to their high lift to drag ratio [6]. The blade has a length of 0.5 meters and is manufactured from a polycarbonate material which is very low in cost and has very good strength properties.

Winglets are devices which are integrated at the tip of wings to reduce the downwash and in the process reduce induced drag. The design of winglets is a complex process that involves many variable parameters that can significantly influence the performance of the device. Winglets are primarily optimised for one particular operating condition such as cruise condition for aircrafts as the majority of time in flight is spent in that condition [7]. However, as wind turbines operate at a wide range of speeds this adds to the complexity of trying to optimise a winglet to operate at one particular operating condition. To simplify the design process not all of the variable parameters were considered. As the aim of this research is to investigate aerodynamic effects of different blade tip configurations, two winglets were designed with the same design parameters and integrated at the turbines blade tip. The upwind winglet is strategically placed at the tip of the blade so that the tip end is facing suction side of the blade where there is relatively low pressure and high velocity. In contrast, the downwind winglet is placed at the region of the blade associated with high pressure and low velocity. Fig. 1 shows the design specification of the winglets. Some parameters such as sweep, toe and twist were neglected to simplify the design process.
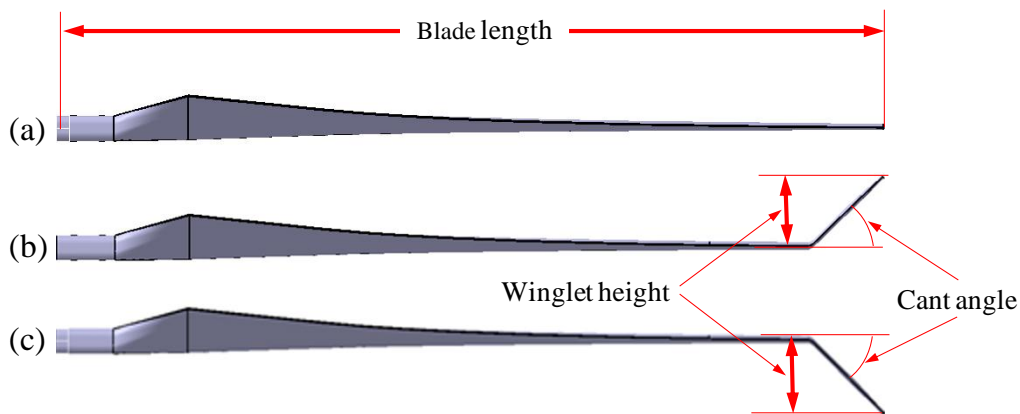

Fig.1. (a) straight blade without winglet; (b) blade with upwind winglet; (c) blade with downwind winglet.

2.2. Wind tunnel test

In this study, RMIT Industrial wind tunnel is employed to measure the aerodynamic drag and lift forces exerted on the blades by the wind. The wind tunnel can be operated at a maximum speed of 145 km/h. Further of the wind tunnel can be found in Alam et al. [8]. The wind turbine blade was mounted vertically on a strut that is connected to a load sensor (manufactured by JR3 Inc., USA) which is a 6-degree of freedom force and moment transducer for real time measurement of aerodynamic forces (drag, lift and side forces) and their corresponding moments (yaw, pitch and roll) simultaneously. The vertical strut that supports the blade is covered by an airfoil shaped device (as shown in Fig. 2) to minimize influence of the strut on the overall aerodynamic forces obtained from the data. All data obtained from the wind tunnel were recorded for 10 seconds time average with a frequency of 20 Hz. To minimize the errors associated with the force sensor, each set of data was computed three times.

In order to compare the aerodynamic performance of different winglet configurations (upwind winglet and downwind winglet) a straight blade (without any winglet) of same length was initially tested in the wind tunnel. As the blades are asymmetric, all the blades were tested over a range of yaw angles (from -90° to +90° with an increment of 15°). At each yaw angle, the blades were tested under a wide range of speeds from 30 to 90 km/h with an increment of 10 km/h. Fig. 3 shows the yaw configuration for the wind tunnel testing.

The aerodynamic drag and lift forces were converted to their non-dimensional parameters drag and lift coefficients (C_D and C_L) using the following formula:

$$C_D = \frac{D}{\frac{1}{2}\rho V^2 A} \tag{1}$$

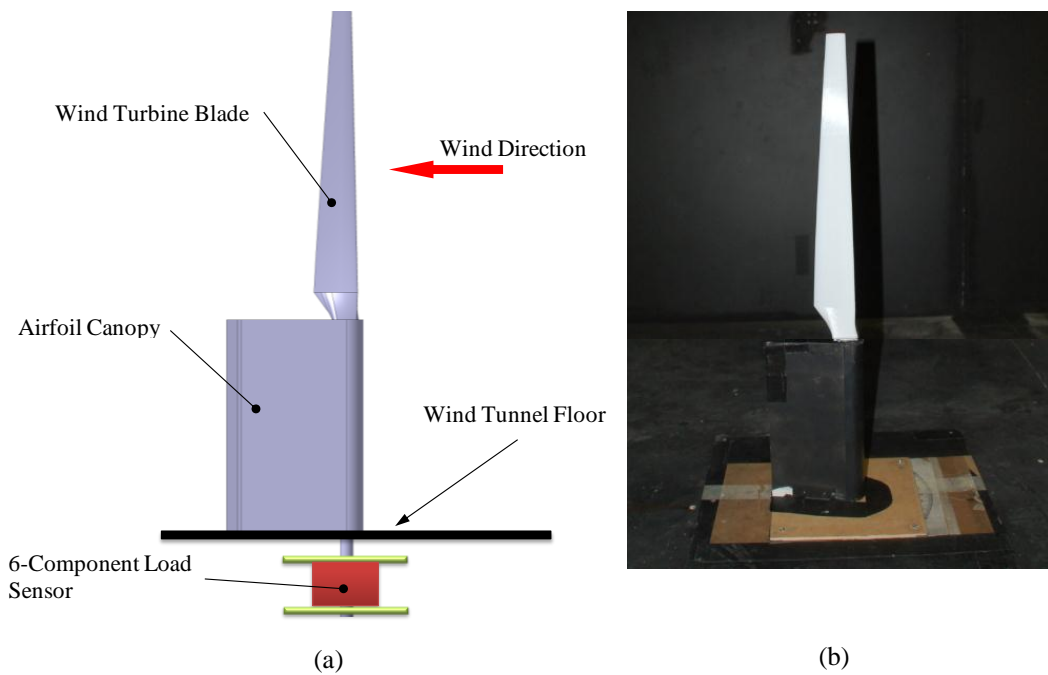$$C_L = \frac{L}{\frac{1}{2}\rho V^2 A} \tag{2}$$

Fig. 2. experimental setup: (a) schematic; (b) inside the wind tunnel for testing.
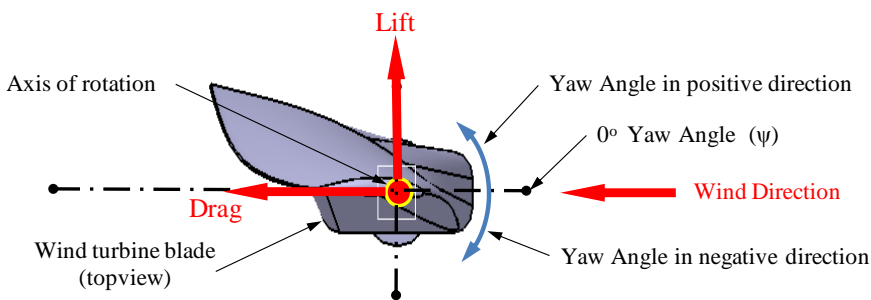

Fig. 3. yaw angle configuration.

3. Results and discussions

In Fig. 4 shows the average C_D and C_L variation with yaw angles for the three blades with different winglet configurations tested. The results indicate that the C_L value varies for both the leeward side (negative yaw angle) and the windward side (positive yaw angle) of the blade with varying yaw angle. At 0° yaw angle, the average C_L value was found to be 0.29. It can be observed from Fig. 4 that the C_L value increases with increasing yaw angle at the windward side of the blade until a yaw of 30° is reached. Above 30°, the C_L value decreases sharply. Similar behavior in C_L value can be observed in the leeward side of the blade. The C_L value reaches its peak at 45° yaw angle before it sharply decreases. The sharp decrease in C_L value is due to the fact that the flow is separating from the blade and the adverse pressure gradients become present. As expected, the drag coefficient continues to rise with increasing yaw angle. At 0° yaw angle the average C_D value is found to be 0.19 as shown in Fig. 4. There is a notable difference in C_D value between the windward and leeward side of the blade at ±90° yaw angle. The average C_D value at ±90° is 1.12 and 0.95 as shown Fig. 4.
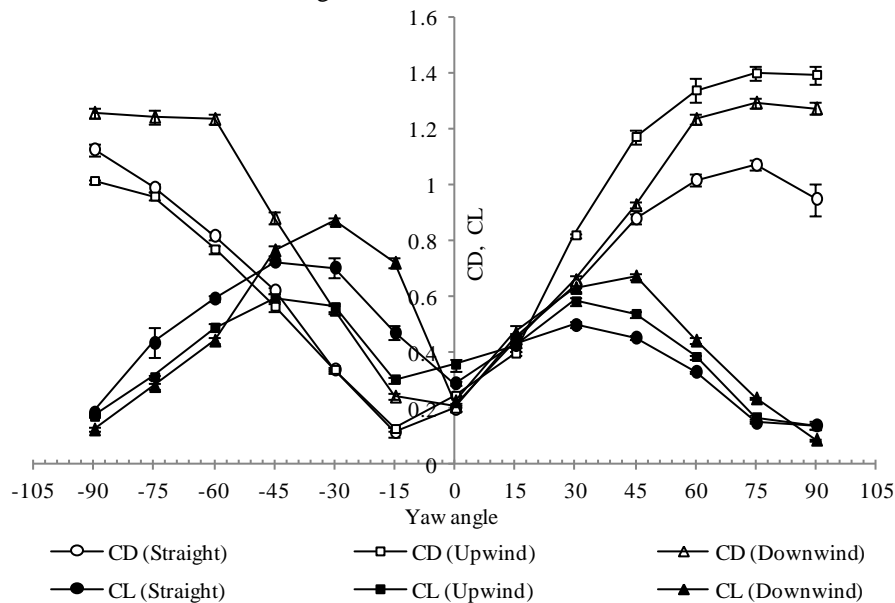

Fig. 4. C_D and C_L as function of yaw angle.

As illustrated in Fig. 4, the forward facing winglet blade produced a higher lift coefficient C_L value at 0° yaw angle when compared to the baseline (straight) blade with a C_L value of 0.35. This corresponds to an increase of 20.7% from the baseline model. Although the C_L value significantly increased the at 0° yaw angle, it was also observed that the C_D value increase for the same yaw angle. The average C_D value at 0 degree yaw angle is found to be 0.24. The flow separates from the blade at the exact the same yaw angle as that of the baseline model but produces much higher C_D and C_L value. Fig. 4 also indicates that the C_D value reaches maximum at 90° yaw angle with an average C_D value of 1.39 at the windward side of the blade, which is significantly greater than at the leeward side of C_D value of 1.01.

The backward facing winglet blade displayed similar results to that of the baseline model. As shown in Fig. 4, the average lift coefficient (C_L) value at 0° yaw angle is found to be 0.22 which is slightly higher than the baseline model of 0.19. The C_L value gradually increases with increasing yaw angle. It can be also observed that the C_L value does not fall sharply until it reaches a yaw angle of 45°. The flow separation from the blade is slightly delayed at the windward side of the blade at 45° yaw angle compared to the both the baseline blade and the forward facing winglet blade. The C_D variation for both the windward and leeward side of the blade is found to be similar. At 0° yaw angle the backward facing winglet produced a C_D value of 0.20 which is practically the same as the baseline blade and significantly lower than the forward facing winglet.

In order to determine the aerodynamic performance of all three blade design configurations, the lift-to-drag ratios (*L/D*) were calculated and the values are plotted as a function of yaw angles as shown in Fig. 5. The figure   shows the *L/D* ratio varies significantly with the yaw angles for all three blades. The forward facing winglet blade produces the highest *L/D* ratio with a value of 5.15 at 0° yaw angle compared to the baseline blade with a value of 4.08 at -15° yaw angle. The lowest lift to drag ratio was produced by the backward facing winglet with a value 2.98 at -15° yaw angle. It was found that the forward facing winglet resulted in an increase in *L/D* ratio of 26% from the baseline blade. In contrast, the backward facing winglet results in a decrease of list 27%.
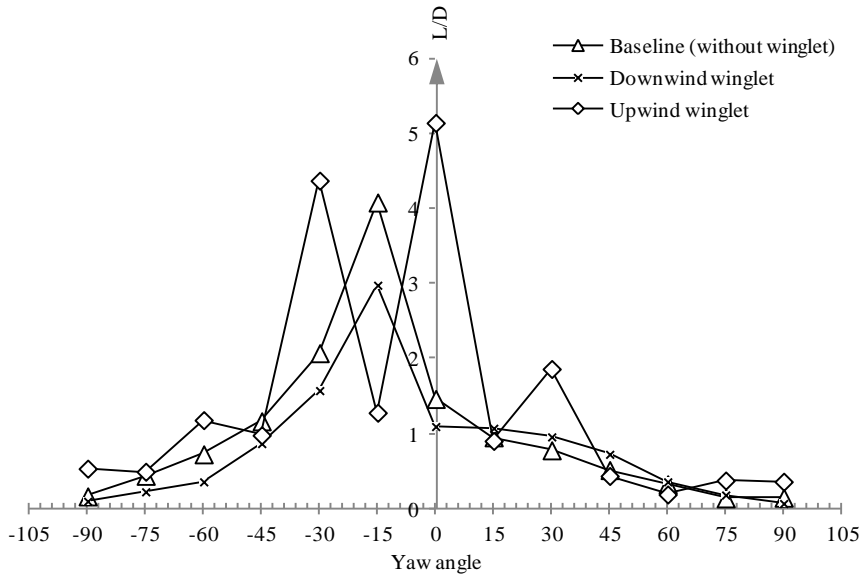

Fig. 5. *L/D* as function of yaw angle.

4. Conclusions

Winglet has significant effect on the aerodynamic performance of the wind turbine blade used for domestic scale wind generator. The results indicated an increase of lift-to-drag ratio with the upwind winglet by around 26% compared to a straight blade with no winglet whereas the downwind winglet results in a decrease of lift-to-drag ratio about 27%. Additionally, yaw angle of the turbine blade plays an important role for the better aerodynamic performance. The results indicate that the maximum aerodynamic performance for can be achieved between 0 and -30 degree yaw angle. Therefore, to get maximum aerodynamic performance, the blade yaw angle should be fixed accordingly. The results show that the maximum lift-to-drag ratio for upwind blade was found at 0 degree yaw angle whereas the straight blade and the downwind winglet blade exhibit the maximum value of lift-to-drag ratio at -15 degree yaw angle.

References

[1] Commonwealth of Australia, securing a clean energy future, The Australian government's climate change plan, 2011.
[2] M.R. Islam, S. Mekhilef, R. Saidur, Progress and recent trends of wind energy technology, J. Renewable and Sustainable Energy, 21 (2013)-456-468.
[3] M. Hansen, Aerodynamics of wind turbines, first ed, James & James, London, 2000.
[4] J. Johansen, N. Sorensen, Aerodynamic investigation of winglets on wind turbines using CFD, Technical Report Riso-R-1543(EN). Riso National Laboratory, 2006.
[5] J. Hyun Lee, S. Park, D. Hwan Kim, S. Hyung Rhee, M. Chan Kim, Computational methods for performance analysis of horizontal axis tidal stream turbines, J. Applied Energy 98 (2012) 512-523.
[6] UIUC Applied Aerodynamics Group. [accessed on 10 December 2011 from http://aerospace.illinois.edu/m-selig/]
[7] M.D. Maughmer, The design of winglets for high performance sailplanes, AIAA 2001-2406.
[8] F. Alam, S. Golde, An Aerodynamic Study of a Micro Scale Vertical Axis Wind Turbine, Procedia Engineering. 56 (2013) 568-572.

6th BSME International Conference on Thermal Engineering (ICTE 2014)

Third generation biofuel from Algae

Firoz Alam, Saleh Mobin and Harun Chowdhury*

School of Aerospace, Mechanical and Manufacturing Engineering, RMIT University, Melbourne, 3083, Australia

Abstract

The use of liquid fossil fuel as an energy source has long been considered unsustainable and most importantly the liquid fossil fuel will be diminished by the middle of this century. In addition, the fossil fuel is directly related to environmental degradation and greenhouse emission. Biofuel produced from plants, animals or algae products can offer an alternative to reduce our dependency on fossil fuel and assist to maintain healthy global environment. Micro-algae is becoming popular candidate for biofuel production due to their high lipid contents, ease of cultivation and rapid growth rate. This paper reviews the current state-of-the-art of biofuel from algae as a renewable energy source.

1. Introduction

The growing concern surrounding the continued use of fossil fuels and rapid depletion of fossil fuel reserves, global climate change, rising crude oil price and environmental degradation have forced governments, policymakers, scientists and researchers to find alternative energy sources. The biofuel production from renewable sources is widely considered to be one of the most sustainable alternatives to fossil fuels and a viable means for environmental and economic sustainability. The biomass of currently produced biofuel is human food stock, which is believed to cause the shortage of food and worldwide dissatisfaction especially in developing nations.

* Corresponding author. Tel.: +61 3 99256103; fax: +61 3 99256108.
   E-mail address: harun.chowdhury@rmit.edu.au

Microalgae are currently being promoted as an ideal third generation biofuel feedstock because of their rapid growth rate, greenhouse gas fixation ability (net zero emission balance) and high production capacity of lipids (fat). They also do not compete with food or feed crops, and can be grown on non-arable land and saline water. Biofuels are generally referred to solid, liquid or gaseous fuels derived from organic matter [1]. The classification of biofuels is shown in Fig. 1 [2].

```
                              ┌──────────────────┐
                              │    Biofuels      │
                              └──────────────────┘
                  ┌────────────────────┴────────────────────┐
        ┌──────────────────┐                    ┌──────────────────┐
        │ Primary Biofuels │                    │ Secondary Biofuels│
        └──────────────────┘                    └──────────────────┘
```

Biofuels

Primary Biofuels

Secondary Biofuels

Natural Biofuel

Produced from
- Firewood, plants
- Wood chips
- Forest
- Animal waste
- Landfill gas
- Crop residues

1st Generation Biofuels

Bioethanol produced from
- Wheat, barley, corn
- Potato, sugarcane, beet
- Oil seeds (soybeans coconut, sunflower rapeseed
- Animal fat, used cooking oil

2nd Generation Biofuels

Bioethanol & Biodiesel produced from
- Cassava, jatropha miscanthus
- Straw, grass, wood

3rd Generation Biofuels

Biodiesel produced from
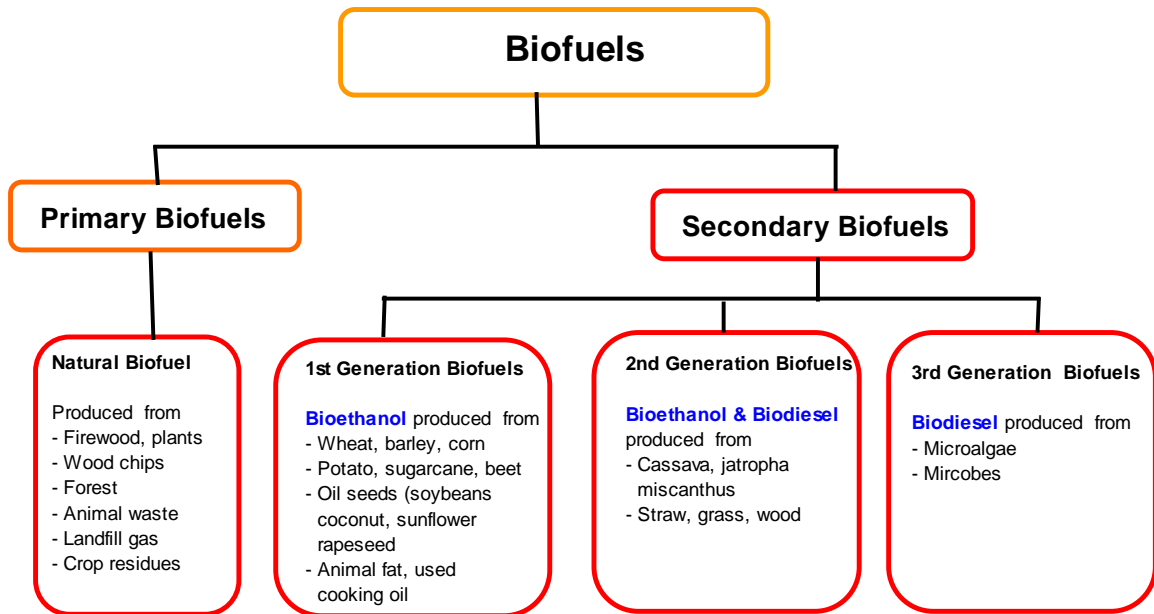- Microalgae
- Mircobes

Fig. 1. Biofuel production sources (biomasses) (adapted from [2, 12]).

The first generation biofuels possess notable economic, environmental and political concern as the mass production of biofuel requires more arable agricultural lands resulting in reduced lands for human and animal food production. Moreover, production process of first generation biofuels is also responsible for environmental degradation. Therefore, enthusiasms about first generation biofuels have been demised. As first generation biofuels are not viable, researchers focused on second generation biofuels. Because of the second generation biofuels production process requires expensive and sophisticated technologies, the biofuel production from the second generation is not profitable for commercial production [2, 4]. Therefore, the researchers focused on third generation biofuels. The main component of third generation biofuels is microalgae as shown in Fig. 1. It is currently considered to be a feasible alternative renewable energy resource for biofuel production overcoming the disadvantages of first and second generation biofuels [1- 2, 5, 16]. Microalgae can provide several different types of renewable biofuels. This includes methane [6], biodiesel [9] and bio-hydrogen [29]. There are many advantages for producing biofuel from algae as microalgae can produce 15 to 300 times more biodiesel than traditional crop on area basis [2]. The harvesting cycle of microalgae is very short and growth rate is very high [2, 15]. Moreover, high quality agricultural land is not required for microalgae biomass production [3].

2. Biofuel Production from Microalgae

Microalgae are single-cell microscopic organisms which are naturally found in fresh water and marine environment. There are more than 300,000 species of micro algae, diversity of which is much greater than plants [3]. Microalgae are generally more efficient converters of solar energy comparing to higher plants. In addition, because the cells grow in aqueous suspension, they have more efficient access to water, CO_2, and other nutrients [2, 5]. The current biofuel yields from various biomasses are shown in Table 1. The table clearly shows huge potential of microalgae compared to other biomasses.

Table 1. E-Portfolio types based on features and purposes (adapted from http://scu.edu.au/teachinglearning/index.php/79).

Oil Yields	Litre/Hectare/Year	Barrels/Hectare/Year
Soybeans	400	2.5
Sunflower	800	5
Canola	1,600	10
Jathropha	2,000	12
Palm Oil	6,000	36
Microalgae	60,000 – 240,000	360 – 1,500

The oil contents of various microalgae in relation to their dry weight are shown in Table 2. It is clear that several species of microalgae can have oil contents up to 80% of their dry body weight. Some microalgae can double their biomasses within 24 hours and the shortest doubling time during their growth is around 3.5 hours which makes microalgae an ideal renewable source for biofuel production [7].

Table 2. Oil contents of microalgae [7].

	Name of microalgae	(% dry wt)
1	Botryococcus braunii	25 - 75
2	Chlorella sp.	28 - 32
3	Crypthecodinium cohnii	20
4	Cylindrotheca sp.	16 - 37
5	Dunaliella primolecta	23
6	Isochrysis sp.	25 - 33
7	Monallanthus salina	20
8	Nannochloris sp.	20 - 35
9	Nannochloropsis sp.	31 - 68
10	Neochloris oleoabundans	35 - 54
11	Nitzschia sp.	45 - 47
12	Phaeodactylum tricornutum	20 - 30
13	Schizochytrium sp.	50 - 77
14	Tetraselmis sueica	15 - 23

3. Microalgal Biomass Production

Producing microalgal biomass is generally more expensive and technologically challenging than growing crops. Photosynthetic growth of microalgae requires light, CO_2, water and inorganic salts. The temperature regime needs to be controlled strictly. For most microalgae growth, the temperature generally remains within 20°C to 30°C. In order to reduce the cost, the biofuel production must rely on freely available sunlight, despite daily and seasonal variations in natural light intensities [7, 17-20]. Growth medium must provide the inorganic elements that constitute the algal cell. Essential elements include nitrogen (N), phosphorus (P), iron (Fe) and in some cases silicon (Si).

Microalgae is grown in various aquatic environments, such as fresh and marine water, municipal waste waters, industrial waste waters and animal waste waters as long as there are adequate amounts of carbon (organic or inorganic), N (urea, ammonium or nitrate), and P as well as other trace elements are present [30]. Sea water supplemented with commercial nitrate and phosphate fertilizers and a few other micronutrients are commonly used for growing marine microalgae [31]. Waste waters are unique in their chemical profile and physical properties as compared with fresh and marine waters. Recent researches indicated the great potential of mass production of algal

biomass for biofuel and other applications using wastewaters. However, wastewater based algae cultivation still faces with many uncertainties and challenges including variation of wastewater composition due to source, infrastructure, weather conditions, and pre-treatment methods, improper nutrient ratios (e.g., C/N and N/P), high turbidity due to the presence of pigments and suspended solid particles which affects light transmission, and the presence of competing microflora and toxic compounds, and accumulation of growth inhibiting compounds which is worsened if water is recycled and reused [30].

There are different ways microalgae can be cultivated. However, two widely used cultivation systems are a) suspended cultures, including open ponds and closed reactors, and b) immobilized cultures, including matrix-immobilized systems and biofilms. The most common large scale production systems in practice are high rate algal ponds or raceway ponds. Raceway ponds are open and shallow with paddle wheel to provide circulation of the algae and nutrients. Raceways are relatively inexpensive to build and operate, but often suffer low productivity for various reasons [5, 32]. Tubular photobioreactors are the only type of closed systems used at large scale production of algae [5].

The photoreactor system can be sub-classified as: a) vertical photoreactor, b) flat or horizontal photoreactor, and c) helical photoreactor. The helical photoreactor is considered the easiest to scale up production. Compared to open ponds, tubular photobioreactors can give better pH and temperature control, better protection against culture contamination, better mixing, less evaporative loss and higher cell densities [32]. However, each system has relative advantages and disadvantages. One of the significant challenges of using raceways and tubular photobioreactors is biomass recovery. This challenge has been mitigated to an extent by immobilized cultures or attached algal processes [33]. Algal biofilms could play a large role in overcoming the major challenges to production and harvesting of microalgae. If enough surface area is provided, algae biofilm growth can be more than suspended growth. More details about these cultivation systems can be found in [2-3, 7].

4. Algae Harvesting Methods

Various methods are currently used for harvesting algae, which includes chemical based, mechanical based, biological based and to a lesser extent, electrical based operations However, various combinations or sequence of these methods are also commonly in use. The cell size of algae is very small. Therefore, chemical flocculation is often performed as a pre-treatment to increase the particle size of algae before using another method such as flotation to harvest the algae. In mechanical based process, centrifugation process, which is the most reliable and rapid method, is used for recovering suspended algae. In electrical based method, negative charge properties of algal cells are used for separating the cells. These cells can be concentrated by the movement in an electric field [34].

5. Biofuels Production Processes from Microalgae

A number of ways the microalgae biomass can be converted into energy sources which includes: a) biochemical conversion, b) chemical reaction, c) direct combustion, and d) thermochemical conversion. Fig. 2 illustrates a schematic of biodiesel and bioethanol production processes using microalgae feedstock [10, 12]. Depending on the microalgae species, in addition to biofuel production, other compounds may also be extracted, with valuable applications in different industrial sectors [2, 8, 10, 21-28]. The production of biofuel is a complex process. A schematic of biofuel production processes from microalgae is shown in Figure 3. However, these processes are complex, technologically challenging and economically expensive.

6. Discussion

The environmentally concerned nations have put emphasis on the use of renewable energy in transport and other sectors. A percentage of renewable energy can be extracted from biofuels. As the second generation biofuels is mainly produced from raw materials (biomasses) that compete with the feedstock of higher vertebrates (human and animal), the 3rd generation biofuels generated from microalgae which do not compete with our feedstock can be well utilised. The biofuels produced from microalgae are generally carbon neutral. The burning process of biofuel

produces CO2 which is in turn consumed by the algae in biomass production. Hence the process is carbon neutral and is a viable alternative to fossil fuels.

Nevertheless, a number of challenges remain in biofuel production. At present research is going on to identify the most promising algae species that can be mass produced in order to make biomass production commercially viable. The biomass production methods (i.e., photobioreactor system and open air (pond) system) also need further research for making algal production economically and environmentally sustainable. Current harvesting process using centrifugation (mechanical), chemical flocculation, biological or electrical methods creates challenges for recovering the suspended algae. All these processes are still relatively costly [13, 16-27].
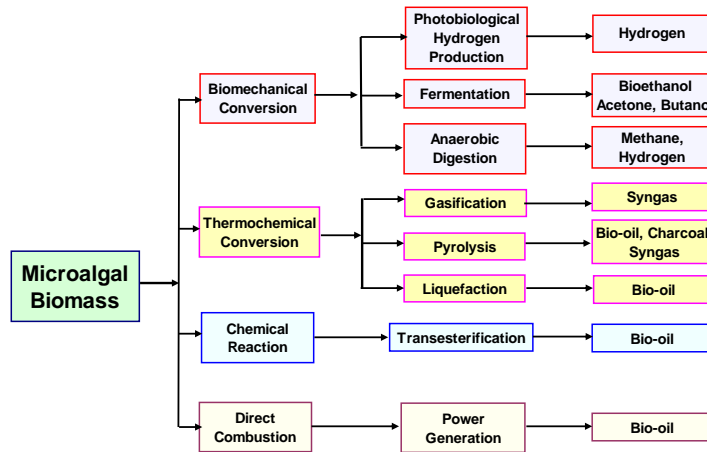

Fig. 2. Biofuel production processes from microalgae biomass, adapted from [2, 11-12]
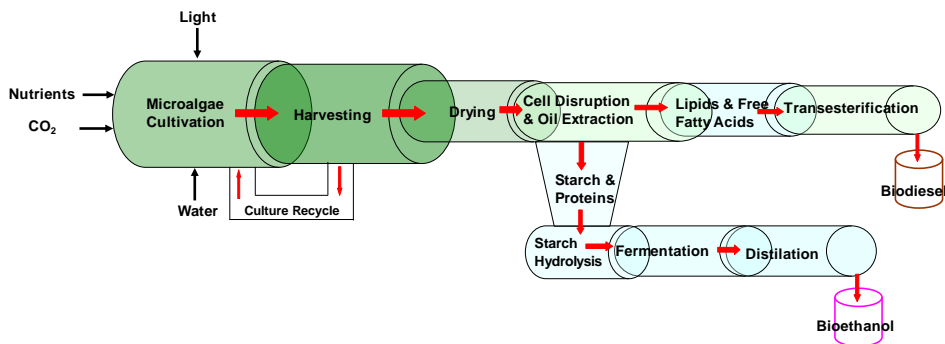

Fig.3. Biodiesel and Bioethanol production processes from microalgae, [2, 12]

Biofuel production from algae biomass can be commercially viable if algal by-products are optimally utilised. The oil part of algae biomass is around 30% and the remaining 70% is algae by-product. This by-product can be utilised as nutrients for feedstock (animal, fish, etc.), pharmaceutical ingredients, cosmetics, toiletries and fragrance products [13, 23-27].

7. Conclusion

Biofuel offers a true supplement to fossil if high yielding algae species can be identified, advanced production and harvesting methods are employed, and innovative drying and oil extraction processes are utilised. Given the current state-of-art, the biofuel cannot be a full replacement of fossil fuel at least in short-term.

References

[1] [1]   Nigam, P.S. and Singh, A. (2011), Production of liquid biofuels from renewable resources, Progress in Energy and Combustion Science, 37(1): 52–68

[2] Dragone, G., Fernandes, B., Vicente, A.A. and Teixeira, J.A. (2010), Third generation biofuels from microalgae in Current Research, Technology and Education Topics in Applied Microbiology and Microbial Biotechnology, Mendez-Vilas A (ed.), Formatex, 1355-1366

[3] Scott, S.A., Davey, M.P., Dennis, J.S., Horst, I., Howe, C.J., Lea-Smith, D.J. and Smith, A.G. (2010), Biodiesel from algae: challenges and prospects, Current Opinion in Biotechnology, 21:277-286.

[4] Brennan L, Owende P. (2010), Biofuels from microalgae--A review of technologies for production, processing, and extractions of biofuels and co-products. Renewable and Sustainable Energy Reviews, 14:557-577.

[5] Chisti Y. (2007), Biodiesel from microalgae. Biotechnology Advances, 25:294-306.

[6] Spolaore P, Joannis-Cassan C, Duran E, Isambert A (2006). Commercial applications of microalgae. J Biosci Bioeng, 101: 87-96.

[7] Chisti, Y (2007), Biodiesel from microalgae, Biotechnology Advances, 25:294-306

[8] Um B-H, Kim Y-S. (2008), Review: A chance for Korea to advance algal-biodiesel technology, Journal of Industrial and Engineering Chemistry, 15: 1-7.

[9] Gavrilescu M, Chisti Y. (2005), Biotechnology- a sustainable alternative for chemical industry. Biotechnol Adv, 23: 471-499.

[10]   Mata TM, Martins AA, Caetano NS. (2010), Microalgae for biodiesel production and other applications: A review, Renewable and Sustainable Energy Reviews, 14:217-232.

[11] Wang, B., Li, Y., Wu, N. and Lan, C. (2008), CO2 bio-mitigation using microalgae. Applied Microbiology and Biotechnology, 79:707-718.

[12] Alam, F., Date, A., Rasjidin, R., Mobin, S., Moria, H. and Baqui, A. (2012), Biofuel from Algae- Is It a Viable Alternative? Procedia Engineering, Vol. 49: 221-227.

[13] Lardon, L., Hélias, A., Sialve, B., Steyer, J. P., & Bernard, O. (2009), Life-Cycle Assessment of Biodiesel Production from Microalgae, Environmental, Science & Technology, 43(17): 6475-6481

[14] Koh, L.P., Ghazoul, J. (2008), Biofuels, biodiversity, and people: understanding the conflicts and finding opportunities, Biological Conservation, 141:2450-2460.

[15] Schenk, P., Thomas-Hall, S., Stephens, E., Marx, U., Mussgnug, J., Posten, C., Kruse, O., and Hankamer, B. (2008), Second generation biofuels: high efficiency microalgae for biodiesel production, BioEnergy Research, 1:20-43

[16] Li, Y., Horsman, M., Wu, N., Lan, C.Q. and Dubois-Calero, N. (2008), Biofuels from microalgae, Biotechnology Progress, 24:815-820.

[17] Chaumont, D. (1993), Biotechnology of algal biomass production: a review of systems for outdoor mass culture, Journal of Applied Phycology, 5:593-604.

[18] Borowitzka, M.A. (1999), Commercial production of microalgae: ponds, tanks, tubes and fermenters, Journal of Biotechnology, 70:313-321.

[19] Borowitzka, M.A. (2005), Culturing microalgae in outdoor ponds In: Andersen RA, eds. Algal Culturing Techniques. Burlington, MA: Elsevier Academic Press, 205-218.

[20] Pulz, O. (2001), Photobioreactors: production systems for phototrophic microorganisms, Applied Microbiology and Biotechnology, 57:287-293.

[21] Spolaore, P., Joannis-Cassan, C., Duran, E., and Isambert, A. (2006), Commercial applications of microalgae, Journal of Bioscience and Bioengineering, 101:87-96.

[22] Carvalho, A.P., Meireles, L.A., Malcata, F.X. (2006), Microalgal reactors: A review of enclosed system designs and performances, Biotechnology Progress, 22:1490-1506.

[23] Benemann, J.R., Tillett, D.M. and Weissman, J.C. (1987), Microalgae biotechnology, Trends in Biotechnology, 5:47-53.

[24] Eriksen, N., Poulsen, B., Lønsmann, I.J. (1998), Dual sparging laboratory-scale photobioreactor for continuous production of microalgae, Journal of Applied Phycology, 10:377-382.

[25] Tredici, M.R. (1999), Bioreactors, photo. In: Flickinger MC, Drew SW, eds. Encyclopedia of Bioprocess Technology: Fermentation, Biocatalysis, and Bioseparation. New York, NY: Wiley, 395-419.

[26] Molina, G.E., Belarbi, E.H., Acién, F.G., Robles, M.A. and Chisti, Y. (2003), Biotechnology Advances, 20:491-515.

[27] Harun, R., Singh, M., Forde, G.M., Danquah, M.K. (2010), Bioprocess engineering of microalgae to produce a variety of consumer products, Renewable and Sustainable Energy Reviews, 14:1037-1047.

[28] Mendes-Pinto, M.M., Raposo, M.F.J., Bowen, J., Young, A.J., Morais, R. (2001), Evaluation of different cell disruption processes on encysted cells of Haematococcus pluvialis: effects on astaxanthin recovery and implications for bio-availability, Journal of Applied Phycology, 13: 19-24.

[29] Kapdan IK, Kargi F. (2006), Bio-hydrogen production from waste materials. Enzyme Microb Technol, 38: 569-582.

[30]   Zhou, W., Chen, P., Min, M., Ma, X., Wang, J., Griffith, R., Hussain, F., Peng, P., Xie, Q., Li, Y., Shi, J., Meng, J., Ruan, R. (2014), Environment-enhancing algal biofuel production using wastewaters, Renewable and Sustainable Energy Reviews, 36: 256-269.

[31] Molina, G E. (1999), Microalgae, mass culture methods. In: Flickinger MC, Drew SW, editors. Encyclopedia of bioprocess technology: fermentation, biocatalysis and bioseparation, vol. 3.Wiley; p. 1753–69.

[32] Mata TM, Martins AA, Caetano NS. (2010), Microalgae for biodiesel production and other applications: a review. Renew Sustain Energy Rev, 14: 217–32.

[33] Hoffmann JP. (1998), Wastewater treatment with suspended and nonsuspended algae. Journal of Phycology, 34: 757–763.

[34] Kumar H, Yadava P, Gaur J.(1981), Electrical flocculation of the unicellular green alga Chlorella vulgaris Beijerinck. Aquat Bot, 11: 187-195.